INVESTIGATION OF GROWTH AND STRUCTURE OF FERROELECTRIC THIN FILMS

Thesis submitted in accordance with the requirements of the University of Liverpool for the degree of Doctor in Philosophy

by

Ahmed Awad

October 2008

ABSTRACT

Non-volatile ferroelectric random access memories (NV-FeRAM) are largely regarded as the ideal non-volatile memory due to their highly desirable performance features. Strontium bismuth tantalate (SBT) is an emerging material for use in NV-FeRAM technology. In this thesis, a "single source" Sr-Ta heterometal precursor and a bismuth organometallic precursor were investigated as potential sources for liquid injection based chemical vapour deposition (CVD) of SBT. Two generic CVD processes have been explored, namely: metal organic chemical vapour deposition (MOCVD) and atomic layer deposition (ALD). MOCVD is a well established thin film deposition process, whereas at the time of writing, liquid injection ALD is a relatively novel process tool. The effects of post-deposition annealing on the SBT thin films deposited by both methods have been characterised using a range of techniques to elucidate the structure and composition of the thin film materials. These have included high resolution transmission electron microscopy; medium energy ion scattering; Auger electron spectroscopy; and X-ray diffraction.

Firstly, the growth of strontium tantalate and bismuth oxide was investigated as a prelude to combining the processes to deposit SBT. A single-source precursor of the type $Sr\{Ta(OEt)_5(dmae)\}_2$ has been investigated as a method of alleviating the mismatch between conventional Sr and Ta sources used for the growth of strontium tantalate. Substrate temperature was found to have a significant effect on the composition of the strontium tantalate films grown. The deposition of bismuth oxide films from $Bi(mmp)_3$ was investigated. The bismuth precursor illustrated similar decomposition behaviour to the $Sr\{Ta(OEt)_5(dmae)\}_2$ and demonstrated its suitability as a complementary source of bismuth for SBT.

The synthesis of SBT thin films was investigated using a superlattice approach. Superlattices of varying components of Bi_2O_3 and $SrTa_2O_5$ were deposited by both MOCVD and ALD. The superlattices were then annealed to inter-diffuse the layers to form SBT. Depending on the annealing conditions, the fluorite phase found after growth was either transformed to: a Bi-layered perovskite; or a Bi deficit – pyrochlore phase. The superlattice approach is shown to be an effective route to the synthesis of SBT thin films on silicon.

PUBLICATIONS

Part of the work of this thesis has been published in the following scientific literature:

Richard J. Potter, Ahmed Awad, Paul R. Chalker, Peng Wang, Anthony C. Jones, Timothy C.Q. Noakes, Paul Bailey "A superlattice approach to the synthesis of ferroelectric Strontium Bismuth Tantalate thin films using liquid-injection-MOCVD", Proceedings of the Materials Research Society, 2005 Fall Meeting, Symposium T (2006) 0902-T02-02.

ACKNOWLEDGEMENTS

I would like to express my sincere appreciation to everyone who helped in the writing of this research. I would like to thank in particular my supervisor Professor Paul R. Chalker for his academic direction; meticulous and critical comments throughout this research. His supervision has been an inspiring source of advice and further learning. I am indebted to Dr. Richard Potter for his enduring support and valuable remarks. I would also like to thank Dr. Robert Murray for his moral support during the course of my research.

I am deeply appreciative of my beloved family who have devoted their time and effort generously to participate in the study. I can never repay their debt in anyway for their incessant love, affection and support.

A word of thanks is due also to other friends and colleagues, especially Dr. H. Al-Badiary, Dr. T. Noakes and Dr. S. Taylor for their invaluable help. Their interest and fruitful discussions regarding the project gave me valuable knowledge and experience.

GLOSSARY

AC	Alternating Current
AES	Auger Electron Spectroscopy
ALD	Atomic Layer Deposition
ALCVD	Atomic Layer Chemical Vapour Deposition
CCLRC	Council for the Central Laboratory of the Research Councils
CVD	Chemical Vapour Deposition
DRAM	Dynamic Random Access Memory
DRO	Destructive ReadOut
E_c	Coercive field
E_d	Depolarising field
EDS	Energy Dispersive X-ray Spectroscopy
EELS	Electron Energy Loss Spectroscopy
EEPROM	Electrical Erasable Programmable Read Only Memory
EM	Electron Microscope
EPROM	Electrically Programmable Read Only Memory
eV	Electron Volt
FEFET	Ferroelectric Field Effect Transistor
FeRAM	Ferroelectric Random Access Memory
HEIS	High-Energy Ion Scattering
HR-TEM	High Resolution Transmission Electron Microscope
HVEE	High Vacuum Engineering Europe
IC	Integrated Circuit
JVD	Jet Vapour Deposition
k / ε_r	Dielectric constant
K	Kelvin
LEIS	Low-Energy Ion Scattering
MBE	Molecular Beam Epitaxy

MEIS	Medium Energy Ion Scattering
MFC	Mass Flow Controller
MOCVD	Metal Organic Chemical Vapour Deposition
MOD	Metal Organic Decomposition
NDRO	Non-Destructive ReadOut
NV-FeRAM	Non-Volatile Ferroelectric Random Access Memory
PECVD	Plasma Enhanced Chemical Vapour Deposition
PLC	Programmable Logic Controller
PLD	Pulsed laser deposition
P_R	Remanent polarisation
P_S	Saturation polarisation
PVD	Physical Vapour Deposition
PZT	Lead Zirconium Titanate
RAM	Random Access Memory
RBS	Rutherford Backscattering Spectrometry
rf	radio frequency
ROM	Read Only Memory
SAD	Select Area Diffraction
SBT	Strontium Bismuth Tantalate
SEM	Scanning Electron Microscope
SL	Superlattice
SRAM	Static Random Access Memory
STEM	Scanning Transmission Electron Microscopy
TEA	Toroidal Electrostatic ion Analyser
TEM	Transmission Electron Microscope
UHV	Ultra High Vacuum
ULSI	Ultra Large Scale Integration
UV	Ultraviolet
V	Voltage
XRD	X-Ray Diffraction

CONTENTS

Chapter 1 Introduction

The physical storage of bits of electronic data within integrated circuits is usually achieved via the storage of electronic charge in separate addressable capacitors. The notion of a single 'supreme' memory technology to meet all applications has been pursued by various companies. In reality, fourteen different types of digital memories are utilised in computers or other devices for information storage. The requirements of memories are generically; non-volatility, fast to read and write, bit erasable, electrically re-programmable, low power, durable, dense and cheap. Such memories range from slow, inexpensive tapes or discs (used for archival storage) to fast but expensive static random access memories (SRAMs) and dynamic random access memories (DRAMs). Although, none of the memories are completely perfect, FeRAM (ferroelectric random access memory) is considered to be the ideal memory.

All kinds of memories can be divided into the general categories; volatile memory, which loses stored data without an external power source and non-volatile memory, which stores recorded data even after the external power source has been switched off. For instance, magnetic disks are

non-volatile; however, they are large and mechanically fragile. They consume a lot of power and have the disadvantage of slow access speeds during writing and reading data. In the case of a DRAM, the data is stored in the form of a charge in a capacitor. In order to safely maintain the stored data, it is necessary to continuously supply a constant voltage to the capacitors, which are recharged a hundred times per second by refresh circuitry. If the power is interrupted, the DRAM loses all data stored, implying that it is volatile. By contrast, data in ferroelectric capacitors are stored via the remanent polarisation states of its ferroelectric material. A ferroelectric capacitor has a non-linear dielectric property with permanent charge retention capabilities following the application of a voltage. The stored data continues to exist whilst the power is turned off, indicating that FeRAM is non-volatile.

Although it has been known that the polarisation states could be used as the binary digits for sorting information, since the discovery of the ferroelectricity in 1921, the effort of the chip manufacturers to develop and exploit ferroelectric materials in semiconductor memories has not occurred until relatively recently. The main driver for this emerging technology has been growth of the DRAM market. The DRAM architecture is simple, as it consists of a one-Transistor/one-Capacitor

(1T/1C) cell. The capacitors in DRAM's usually have nitride and oxide layers as dielectrics. The dielectric constant for this insulator 'stack' is in the order of 6. To enhance the memory cell capacitance for higher memory densities as feature sizes decrease several strategies have been adopted. These include reduction of the dielectric thickness; architectures including fins stack and crowns; and use of deep trenches for area enlargement. However, at the beginning of the 1990's, every major DRAM manufacturer realised that these strategies were approaching the limit of their capabilities in maintaining the cell capacitance. To address this, new upcoming DRAM generations will require materials with higher values of dielectric constant, k or ε_r. Ferroelectrics with the Curie point around the operation temperature (usually room temperature) have large dielectric constants. Recently, several semiconductor industries emerged with products based on new ferroelectric materials and electrodes. Since the basic issues for both high-k DRAM and NV-FeRAM are very similar, most of the major DRAM manufacturers have instigated projects to develop high density FeRAMs. Ramtron International Corporation was the first semiconductor company which succeeded in making low-density solid-state ferroelectric memory devices with lead zirconium titanate (PZT). Besides the well-known PZT, the newer bismuth-layered

perovskite strontium bismuth tantalate (SBT) are promising ferroelectric materials for the use in FeRAMs.

In any DRAM, the dielectric is not ideal, as it contains defects and impurities that make the capacitor leak. The loss of charge signifies that stored information will disappear with time. In order to maintain the information and to separate the binary "1" and "0" digits, the charge of the capacitor has to be permanently read and rewritten. This is called a 'refresh' and has to be performed every 10-30 ms in a DRAM, depending on the quality of the dielectric. To account for the power if turned off or outages, some of the more expensive memories use internal electrical erasable programmable read only memories (EEPROMs), which stores data as electrical charges in floating-gate electrodes, backed-up in SRAMs or via a battery to create a non-volatile RAM for data backup. However, these memory strategies suffer from: high voltage writing (12-16V); slow writing times in the ms range; and from deterioration in memory function after $\sim 10^6$ write cycles. The above mentioned drawbacks can be completely eliminated if SRAMs, EEPROMs, and flash memories are replaced by FeRAMs, which can be tailored to possess longer lifetimes and higher speeds. When comparing these

properties to FeRAM, the latter offers possibilities of a universally ideal RAM (see Table 1).

Properties	**FeRAM**	**DRAM**	**FLASH**	**SRAM**
Read Cycles	$> 10^{15}$	10^{15}	10^{15}	10^{15}
Write Cycles	$> 10^{15}$	10^{15}	10^{6}	10^{15}
Write Voltage	0.8 – 5V	1 – 5V	12 – 16V	1 – 5V
Access Time	20 – < 100ns	40 – 70ns	40 – 70ns	6 – 70ns
Write Time	1 – < 100ns	1ns	µs – ns	1ns
Cell Size	1x	1x	1x	> 4x
Data Retention (power off)	> 10 years	No	> 10 years	No

Table 1: Properties of different memory types [1]

The selection criteria for a non-volatile memory includes, namely: fast read/write; radiation hardness; cost effectiveness and compatibility with currently used integrated circuit (IC) processing technology; high endurance and retention; and non-destructive readout capability. Considering all of these aspects, the ferroelectric memory stands out as the logical choice.

In the current marketplace, the use of FeRAMs is limited to applications, which include low-density memories in video game devices, television

sets, fax machines, printers, mobile phones, and fully embedded ferroelectric memories in silicon microprocessors and microcontrollers. Some of the state-of-art FeRAMs, commercially available, are 4 Mbit RAMs from Samsung, 1 Mbit RAMs from NEC, and 256 kbit RAMs from Matsushita. However, current commercially available FeRAMs are limited to low density structures, in which one-Transistor/one-Capacitor structures (1T/1C) are used with the capacitor being located adjacent to the transistor (see Figure 1). FeRAMs could capture an appreciable market in the field of non-volatile memories, providing that high density FeRAMs are achievable.

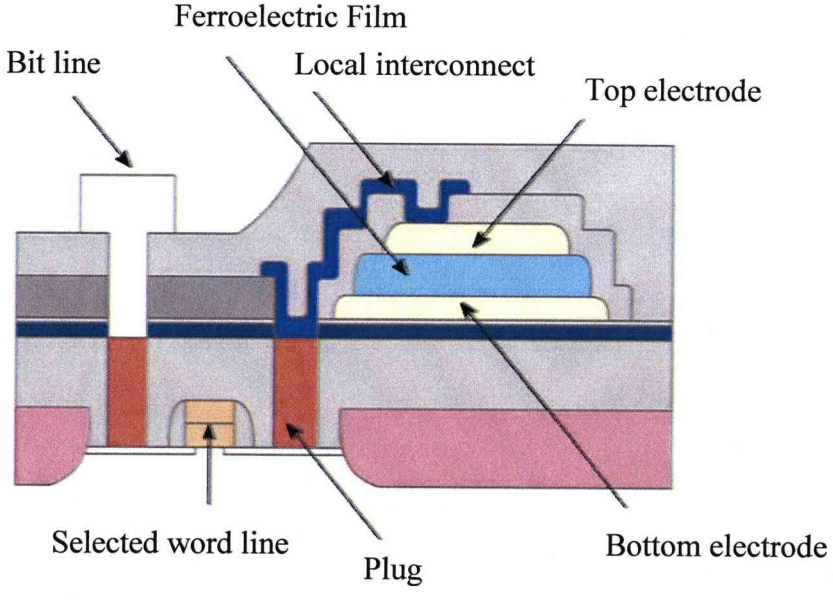

Figure 1: Schematic cross section of a FeRAM unit cell

In order to realise high-density FeRAM structures (in the Gigabit range), a FeRAM cell is required where the capacitor is built on top of the transistor. In principle, FeRAMs could replace EPROMs, EEPROMS, SRAMs, and DRAMs. Furthermore, if high density FeRAMs could be developed and the production cost reduced to the level of magnetic cores, then FeRAMs could also replace the hard disk and become a mass storage device. This is due to their faster access speed and the absence of mechanical wear problems.

1.1 Purpose of Research

This research embodied in this thesis addresses issues, which can be related to the processing of ferroelectric thin films for use as a capacitor in high-density ferroelectric random access memory (FeRAM) cells. In view of the fundamental ferroelectric properties required, namely remanent polarisation (P_R) and coercive field (E_c), there are two leading potential ferroelectric materials for FeRAM applications. These materials are lead zirconate titanate (PZT) and strontium bismuth tantalate (SBT), which are currently receiving much attention in the research literature.

PZT possesses a low processing temperature of 650°C, a low coercive field of 30 kV/cm and a high remanent polarisation of 40 $\mu C/cm^2$. However, PZT capacitors possess a very high fatigue rate (> 60% at the end of 10^8 switching cycles) [2,3,4].

SBT has been shown to have excellent fatigue-resistant properties, maintaining adequate remanent polarisation even after 10^{12} switching cycles [5]. However, the processing temperature of SBT is as high as 800°C, which is unsuitable for integration into high-density memory

circuits. SBT can be processed at temperatures as low as 650°C, however such capacitors do not exhibit detectable remanent polarisation.

1.2 Objectives of Research

As part of this work, new chemical precursors for the deposition of SBT film have been evaluated and the following areas of material science have been investigated:

- Development of a low temperature deposition process for SBT thin films based on the transformation of binary superlattice structures.
- Evaluation of thin film composition and contamination by Auger electron spectroscopy (AES).
- The diffusion of strontium, bismuth, and tantalum measured by medium energy ion scattering (MEIS).
- Characterisation of thin film morphology by transmission electron microscopy (TEM) and X-ray diffraction (XRD), particularly occurring as a function of composition or temperature.
- Comparison of the growth and composition of SBT films prepared by different deposition techniques, namely liquid-injection metal organic chemical vapour deposition (MOCVD) and atomic layer deposition (ALD).

Thin film coating technologies designed to deposit ferroelectric films have been continuously developing to meet technological demands. As part of this research, the new technique of liquid-injection MOCVD and ALD has been exploited using an Aixtron AIX 200FE research reactor. These novel methods have the potential for accurately metering precursor dosing to enable growth of atomically precise thin film structures from new precursors'. This approach makes nano-scale film structures feasible, which until now have been impossible process with previous deposition technologies.

1.3 References

[1] C. Dehm, W. Hartner, G. Schindler, R. Bergmann, B. Hasler, I. Kasko, M. Kastner, M. Schiele, V. Weinrich and C. Mazuré, *Integrated Ferroelectrics*, **26**, 197 (1999).

[2] R. Gross, L. Alff, A. Beck, O.M. Froehlich, D. Koelle and A. Marx, *IEEE Trans. Appl. Supercon.*, **7**, 2929 (1997).

[3] J.F. Scott and C.A. Paz de Arauja, *Science*, **246**, 1400 (1989).

[4] S. Jin, T.H. Tiefel, M. McCormack, R.A. Fastnach, R. Ramesh and L.H. Chien, *Science*, **264**, 413 (1994).

[5] C.A. Paz de Arauja, J.D. Cuchiaro, K.D. McMillan, M.C. Scott and J.F. Scott, *Nature*, **347**, 627 (1995).

Chapter 2 Literature and Background

2.1 Ferroelectricity and FeRAM

The idea of using ferroelectric materials as data storage devices began in the early 1950s and is still ongoing till this day. Researchers at various laboratories (e.g. IBM) have conducted studies on ferroelectric capacitors, in an attempt to replace existing ferromagnetic memories, which were space consuming [1]. By using the two stable remanent polarisation states $+P_R$ and $-P_R$ of a ferroelectric crystal at zero electric field, it is possible to store the information as '0' and '1' states of data required for Boolean algebra. However, these early developments of ferroelectric memories were unsuccessful largely due to: the higher operating voltage of devices; poor control of switching threshold and lack of isolation of memory elements in the matrix. In the 1970s, copious research activity was focused on the development of silicon-based random access memory devices (RAM) and read only memory devices (ROM). These included dynamic RAMs (DRAM), static RAMs (SRAM), electrically programmable ROMs (EPROM), and electrically erasable programmable ROMs (EEPROM). All of the aforementioned offered good performance at low cost and reasonable compactness. However,

EPROMs and EEPROMs suffered from slower read and write speeds and a limited number of allowed write cycles as compared to the volatile counterparts DRAMs and SRAMs.

From the 1980s a renewed interest in ferroelectric memories became apparent, mainly due to improvements in the thin film deposition techniques [2,3,4]. This permitted wafer scale integration of ferroelectric thin films as thin as 25 nm, which led to lowering the operating voltages to 1V. This reduces power consumption and significantly reduces cost. A ferroelectric random access memory (FeRAM) combines advantages of both volatile DRAM and SRAM and non-volatile EPROM and EEPROM. A FeRAM is non-volatile, and can be accessed at higher speeds like a DRAM and SRAM (60ns), and operates at lower voltages (< 5V) [5]. Additionally FeRAMs are radiation hard which makes them useful for military applications and satellite communication systems. Figure 2.1 [5] shows a plot of access time versus cost per bit developed and projected over a period of roughly 10 years. In 1988 (Figure 2.1 (a)), there were approximately 14 different types of digital electronic memories ranging from cheaper but slow and high-density disks to the fast SRAMs. It was anticipated then that by 1998 (Figure 2.1 (b)), FeRAM would eliminate core magnetic and bubble memory and other

devices, thus making the memory market further competitive. In 1999, NEC (Figure 2.1 (c)) projected the future of FeRAMs in smart cards, audio memories, computers etc.

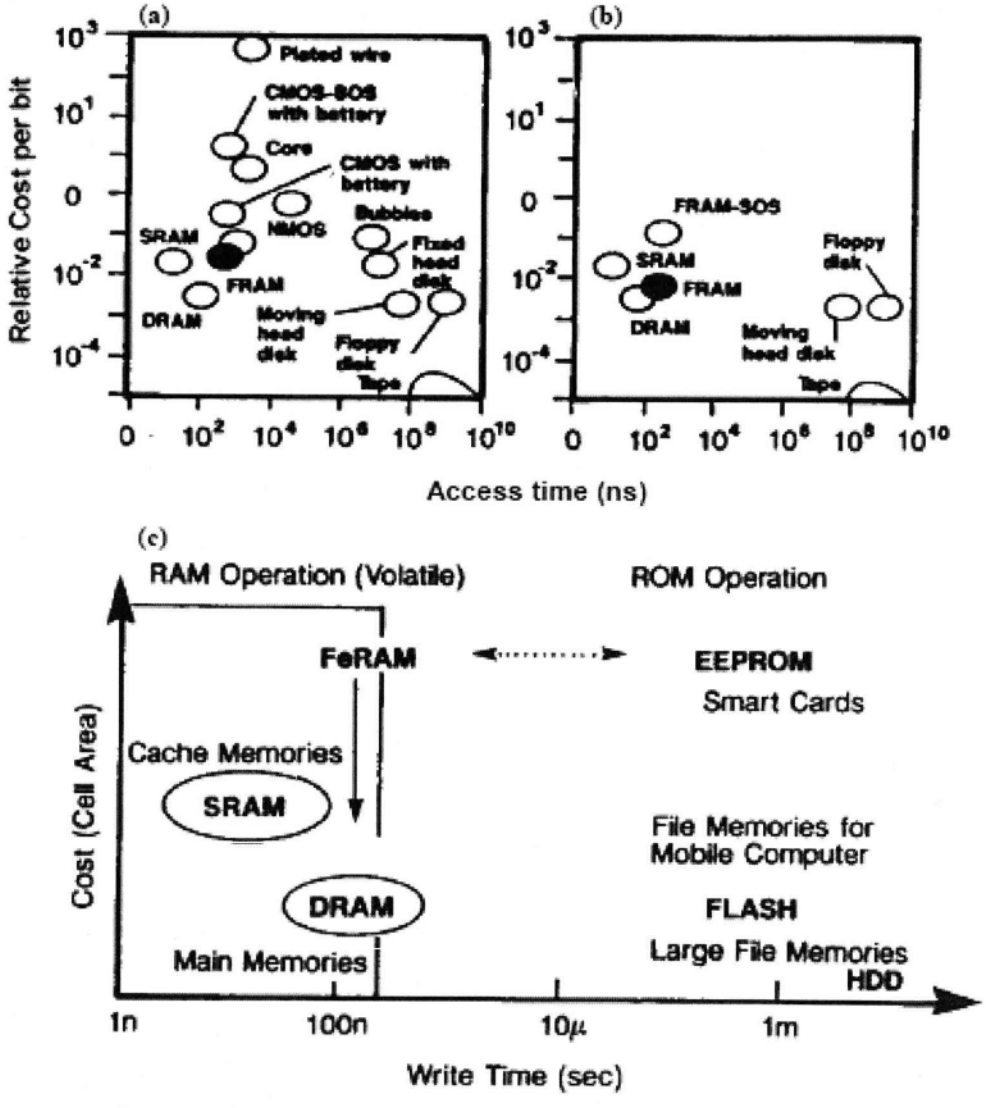

Figure 2.1: Cost per bit versus access time: **(a)** for various kinds of digital memory in use in 1988; **(b)** projections for 1998 made in 1989; **(c)** 1999 comparisons by NEC [5]

The following sections describe the phenomenon of ferroelectricity and how ferroelectric memories operate; the properties required for a FeRAM; candidate materials and present issues.

2.1.1 Principles of Ferroelectricity

This section attempts to provide a brief account of ferroelectricity principles and also describes how a ferroelectric memory operates [1]. The phenomenon of ferroelectricity in ferroelectric materials is analogous to the ferromagnetism in ferromagnetic materials. Just as ferromagnetic materials exhibit a spontaneous magnetic moment at zero magnetic field, ferroelectric crystals also exhibit a spontaneous electric dipole moment per unit volume or polarisation at zero electric field. This behaviour is observed below a certain transition temperature, named the Curie temperature above which the conversion of ferroelectric phase into paraelectric phase occurs. Moreover this always has higher symmetry than the ferroelectric phase and is in a non-polar state where dipoles are randomly oriented in crystal giving rise to zero polarisation. In order to describe the essential feature of ferroelectricity, a hypothetical model of a two dimensional crystal AB (oversimplified) is assumed, shown in Figure

2.2 [1]. The A ions, expressed as carrying a negative charge are located at the lattice points and B ions carrying a positive charge are located on the horizontal lines joining A ions. At equilibrium, B ions always lie closer to one of the two adjacent A ions than to the other. This situation can be explained in terms of potential between two adjacent A ions. There are two equilibrium positions in which a B ion can stay, but to change from one state to another, energy must be provided to overcome an energy barrier ΔE. Let us assume that at a given temperature T, all the B ions are closer to the A ions on their left and consider each AB group as an electric dipole. In this situation the structure can be visualised as the top two layers of (Figure 2.2 (a)) and the assembly of dipoles can be expressed as the same rows in (Figure 2.2 (b)). In this state, the crystal is said to be spontaneously polarised: with a dipole moment per unit volume i.e. spontaneous polarisation. The crystals exhibiting this property are called pyroelectric and the direction of spontaneous polarisation is called the polar axis.

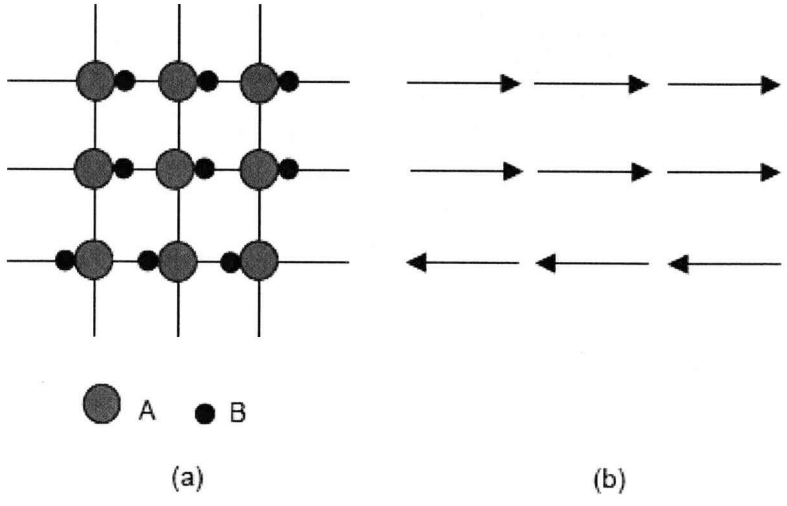

Figure 2.2: Schematic representation of structure and dipoles in a hypothetical 2-D crystal

2.1.1.1 Ferroelectric Domains

Alignment of dipoles in one of the polar directions may extend only over a region of the crystal and there can be different regions in the crystal with aligned dipoles, which are oriented in many different directions with respect to one another. Regions of uniform polarisation are called domains, and they are separated by a boundary from one another called a domain wall. Ferroelectric domain walls are narrower than the domain walls in ferromagnetic materials. TEM observations have shown that ferroelectric domain walls are of the order 1-10 nm [6]. It should be noted

that ferroelectric domain walls should not be confused with grain boundaries in a polycrystalline material. Unlike grain boundaries, domain walls separate domains, which are inclined to each other by angles, governed by the crystal system of the ferroelectric.

The types of domain walls that can occur in a ferroelectric crystal depend upon the crystal structure and symmetry of both paraelectric and ferroelectric phases. The driving force for the formation of domain walls is the minimisation of the electrostatic energy of the depolarising field (E_d) and the elastic energy associated with the mechanical constraints arising due to ferroelectric-paraelectric phase transition. A depolarising field, oppositely oriented to the direction of remanent polarisation P_R, is caused due to the formation of a surface charge in the ferroelectric material at the onset of spontaneous polarisation at the transition temperature. This depolarisation field will form whenever there is a non-homogeneous distribution of the spontaneous polarisation (e.g. due to change in polarisation at the grain boundaries or due to the fall-off of the polarisation near the surface of ferroelectrics) and it can be very strong (of the order of MV/m), making the single domain state of the material energetically unfavourable. This electrostatic energy associated with the depolarising field can be minimised by: (1) splitting of the material into

oppositely oriented domains or (2) compensation of the electrical charge via electrical conduction through the crystal.

2.1.1.2 Ferroelectric Switching

Upon application of a DC electric field in the horizontal direction of Figure 2.2, the dipoles, which were already aligned in the field direction, will remain aligned, however, those which are antiparallel, will have a tendency to reorient themselves in the direction of electric field. As a sufficiently large electric field is applied, their dipoles will have the ability to align themselves in the direction of applied field. The phenomenon of polarisation reversal takes place by nucleation of favourably oriented domains and domain wall motion.

If it is assumed that our hypothetical crystal has an equal number of positive and negative domains then the net polarisation of the crystal will be zero. When an electric field E is applied, initial polarisation P increases linearly with the increasing electric field and the crystal behaves like a dielectric. This is due to the applied field not being large enough to switch any of the domains oriented opposite to its direction. A

plot between P and E is illustrated in Figure 2.3 and the linear region is shown as AB.

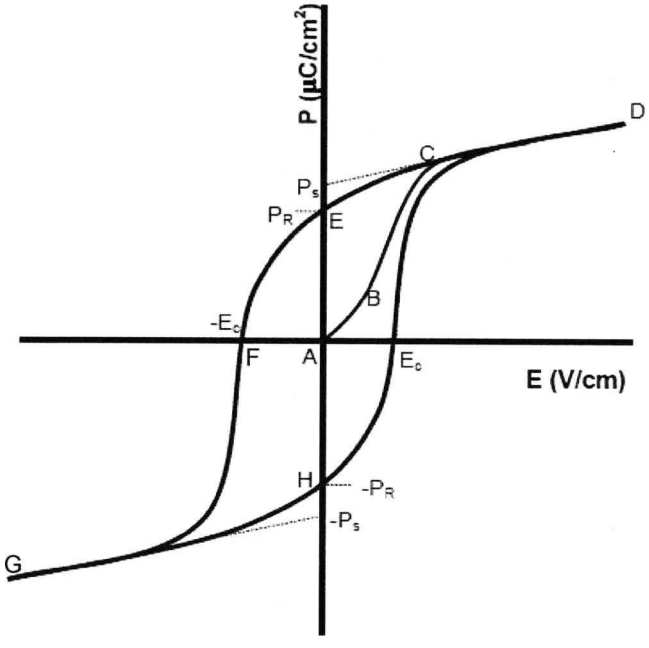

Figure 2.3: Characteristic hysteresis loops of a ferroelectric material

As the electric field is further increased, oppositely oriented domains start to reorient themselves and polarisation starts increasing rapidly (BC) until all the domains are aligned in the direction of the electric field, i.e. reach a single domain state (CD) when polarisation saturates to a value called saturation polarisation (P_S). Upon decreasing the electric field, the polarisation generally does not return to zero, however, follows path DE

and at zero field several domains remain aligned in the positive direction, thus the crystal exhibits a remanent polarisation (P_R). To return the crystal back to zero polarisation state, negative electric field is required (along the path EF) which is also called coercive field (E_C). Further increase of electric field in the negative direction will cause complete reversal of all domains in the direction of field (path FG) and the loop can be completed by following the path GHD. This relation between P and E is called a ferroelectric hysteresis loop, an important characteristic of a ferroelectric crystal. The principle feature of a ferroelectric crystal is not only the presence of spontaneous polarisation but also that this polarisation is reversible by application of an electric field.

2.1.1.3 Crystal Systems

The phenomenon of ferroelectricity is also influenced by the crystal system of the ferroelectric material. Only non-centrosymmetric crystal systems, which have unique polar axis/axes, can exhibit ferroelectricity. A polar axis is the one, which shows directionality, and none of the symmetry operations appropriate to the crystal class will switch this directionality. The value of spontaneous polarisation is dependent upon

temperature i.e. polarisation changes as the crystal temperature changes and electrical charges can be observed on the faces perpendicular to the polar axis. This effect is called the pyroelectric effect. However, not all the crystals with these characteristics show ferroelectricity, i.e. not all of them show reversibility of spontaneous polarisation on applying electric field. Therefore, a ferroelectric crystal is a pyroelectric crystal with reversible polarisation upon application of electric field.

2.1.1.4 Poling of Ferroelectrics

Due to the complex set of elastic and electric boundary conditions at each grain, ferroelectric grains in ceramics and polycrystalline films generally split into many domains (see Figure 2.4) [7].

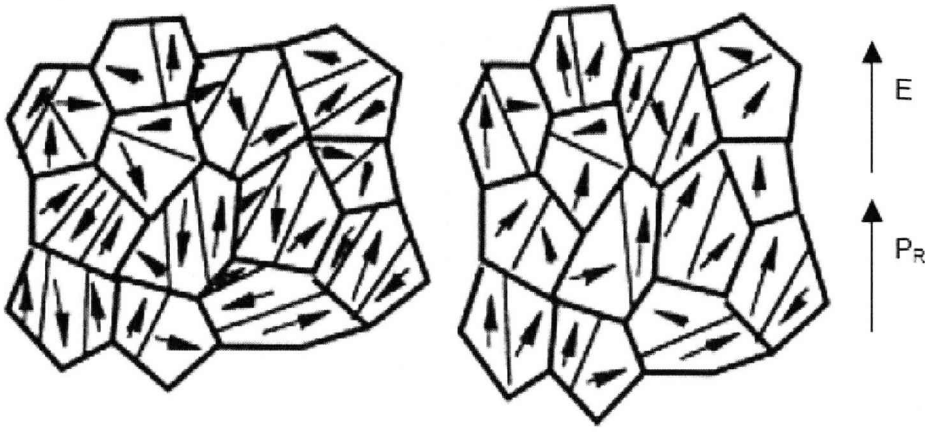

Figure 2.4: Illustration of the reorientation of domains in a polycrystalline ferroelectric material after poling [7]

If the direction of spontaneous polarisation is distributed randomly through the material then the material will show zero net polarisation and is non-polar. Such material will not be pyroelectric or piezoelectric. Polycrystalline ferroelectrics can be brought into a polar state by application of a strong electric field (10-100 kV/cm), usually at elevated temperatures. By this process, domains in an individual grain can be reoriented in the direction of the applied electric field. This material will have a non-zero polarisation even if all the domains do not reorient themselves completely. A single crystal without domains is said to be in a single or mono domain state. This state can also be achieved by poling the crystal. It should be noted that by definition poling of polycrystalline

material is possible only in ferroelectric materials. A polycrystalline pyroelectric (non-ferroelectric) or piezoelectric materials cannot be poled.

The polarisation at zero electric field is known as remanent polarisation (P_R) as mentioned earlier. Maximum remanent polarisation achieved in a polycrystalline ferroelectric material depends on the available domain states. Based on theoretical calculations [8], in a ferroelectric with only 180° domains, maximum P_R is $0.255P_S$. In a tetragonal ferroelectric with six available domain states, maximum P_R is $0.83P_S$. In a rhombohedral ferroelectric with eight possible domain states, maximum P_R is $0.87P_S$. In an orthorhombic ferroelectric with twelve possible domain states, $(P_R)_{max} = 0.91P_S$. However, actual polarisation is lower because of inability of all the domains to be completely reoriented due to; complex set of boundary conditions and some domains switching back to the original state after removal of the field. This may result from the strain associated with dimensional changes in the sample upon poling.

2.1.1.5 Measurement of Hysteresis Loop

Ferroelectric hysteresis loops can be measured experimentally using a Sawyer-Tower circuit [9], using an AC field. The output can be observed on the screen of an oscilloscope. The circuit is shown schematically in Figure 2.5. A plot of the voltage across the crystal versus the field dependent polarisation is the usual representation for this type of data. The capacitor C_0 is connected in series with the crystal.

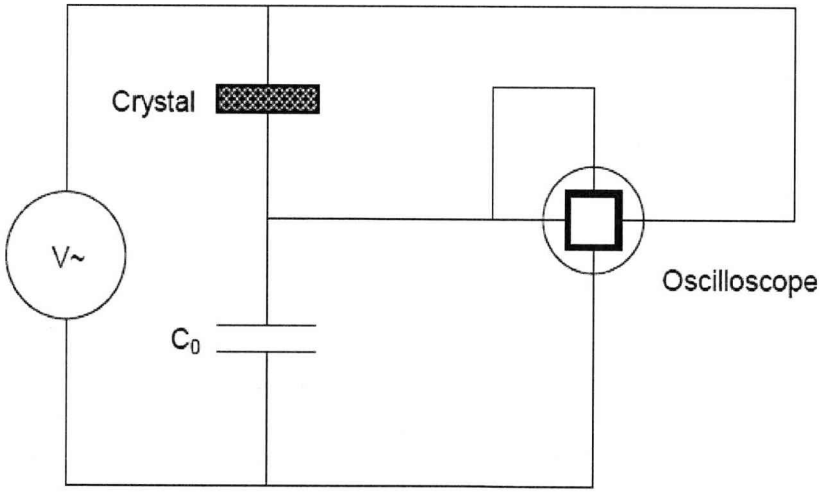

Figure 2.5: Schematic representation of Sawyer-Tower circuit

In this configuration, the voltage across C_0 is proportional to the polarisation of the crystal. This circuit not only measures the hysteresis, it also quantifies the spontaneous polarisation and coercive field E_C.

2.1.2 Basic Operation of a Ferroelectric Memory Cell

Most of the ferroelectric materials, which are potential candidates for ferroelectric devices including memories, are oxides such as barium titanate, lead titanate etc. These materials have structures all based on the perovskite ABO_3 structure. The crystal structure of the characteristic tetragonal perovskite unit cell is illustrated below (Figure 2.6), where A^{+2} ions occupy the corner of the unit cell, B^{+4} ion lies at the centre of the unit cell, and O^{-2} ions stay at the face centres of the unit cell.

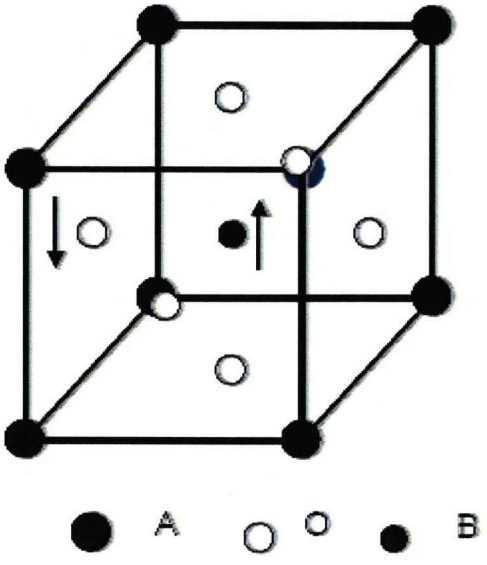

Figure 2.6: A typical ABO_3 perovskite unit-cell

Since the cubic phase is centrosymmetric, having no polar axis, there is no net spontaneous polarisation in the crystal. However, structural distortion at the Curie temperature causes the unit cell to change to a non-centrosymmetric tetragonal structure, which then gives rise to a net dipole moment (or spontaneous polarisation). Movement of the central atom, B, is the key to the ferroelectricity. It works as a 'switch' and can be moved up or down relative to other ions by application of an electric field. This characteristic of the central atom gives rise to the hysteresis behaviour in a ferroelectric material as shown in Figure 2.3. At zero field we have two stable states of polarisation $+P_R$ and $-P_R$, arbitrarily defined as states '0' or '1'. Binary information in the form of '0' and '1' can be

stored by moving this atom up or down. When the applied field is interrupted, the atom retains its position thereby preserving the data in the memory device. This phenomenon can be termed as non-volatility and this property of a ferroelectric can be utilised to make a non-volatile memory device, generally known as FeRAM (ferroelectric random access memory) device. The movement of the central atom is very fast and can be moved numerous times e.g. for 10^{12} switching cycles.

A typical memory cell is schematically shown in Figure 2.7. In the current devices, the memory cells are arranged in a square matrix. Therefore, a 1-megabit memory cell will have 1000 rows (drive line) and 1000 columns (word line). To overcome the cross-talk problem between two neighbouring cells, each memory cell capacitor is isolated from its neighbours by means of a pass-gate transistor. Each bit is written by applying one half a short voltage pulse along a row and the other half along a column. In this state, pulses add up to switch the polarisation state only at the particularly addressed cell. Two reading schemes for the FeRAMs are being explored, namely: destructive readout (DRO) where the information must be rewritten after every read operation and non-destructive readout (NDRO) where information can be read over and over again until the next write operation [10]. DRO is the most likely used

scheme in the present generation FeRAMs as it closely resembles a DRAM. In DRO, the bit is read when a positive switching voltage is applied to the memory cell in the same way as the writing voltage is applied. If the data is already stored as state '0' or $+P_R$, then only a linear non-switching response is measured in the form of a voltage across as 10-50 ohm resistor. If the data was stored as state '1' or $-P_R$, a switching response greater than the linear response is measured as it contains the additional displacement current term dP/dt where P is the polarisation. A sense amplifier then compares this response with that of a reference cell which is always polarised in $+P_R$ or state '0'.

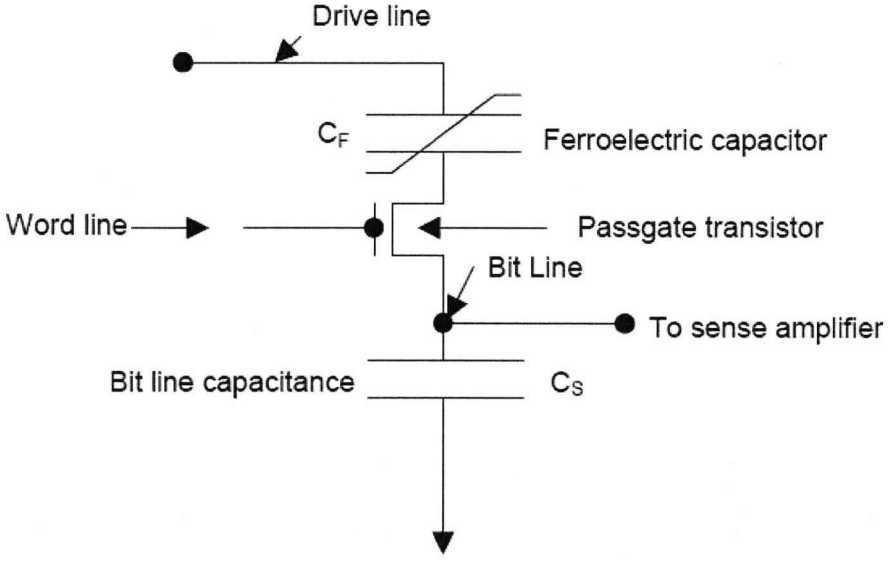

Figure 2.7: Schematic diagram of a typical memory cell

2.1.3 Characteristics of a FeRAM Material

A FeRAM memory should show exhibit:

- Low electrical conductivity,
- Good leakage and breakdown characteristics,
- Large switching polarisation, necessary to store larger amount of data,
- A low switching time (5-200 ns) for faster devices,
- High Curie temperature, above 100°C,
- Good aging and retention characteristics,
- Fatigue resistance up to a minimum of 10^{12} switching cycles (fatigue is defined as rapid decay in the polarisation with increase in the polarisation reversal cycles during bipolar switching),
- Low power consumption i.e. low switching voltage (1-5V),
- Good imprint characteristics (imprint is caused by development of an internal field in the ferroelectric capacitor, leading to a progressive of the hysteresis loop along the field axis).

2.1.4 Reliability of Ferroelectrics

Ferroelectric materials used for FeRAM cells have three main characteristics, affecting the reliability of data retention:

1. Data Retention Characteristics. Figure 2.8 depicts the data retention characteristics. As time T elapses, the polarisation charge Q decreases. This characteristic determines the data retention capability of a non-volatile memory. It can be acceleration tested by increasing the temperature of operation and is predominantly affected by material properties. From the view of circuit design, this characteristic can be improved by optimising the write voltage value of the ferroelectric capacitor.

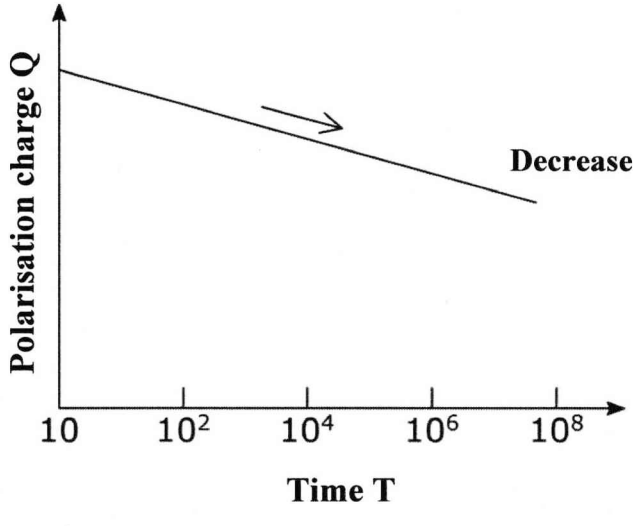

Figure 2.8: Data retention characteristics

2. Fatigue Characteristics. The fatigue characteristics refer to the tendency of the polarisation charge Q to decrease as a result of repeated polarisation reversals, illustrated in Figure 2.9.

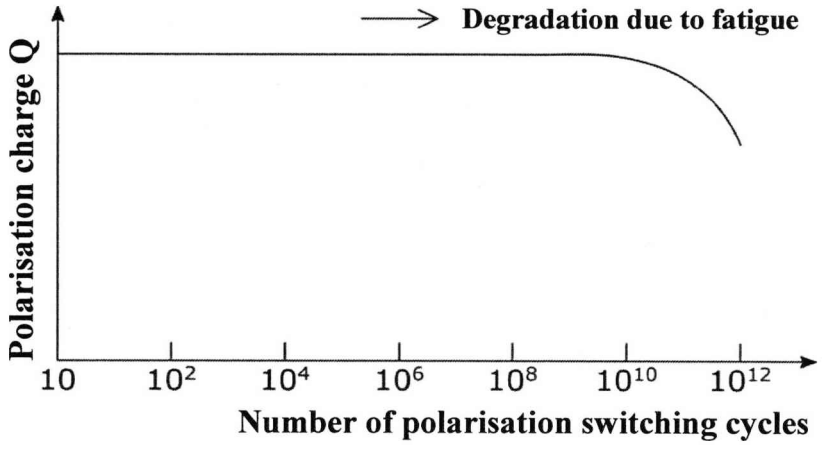

Figure 2.9: Fatigue characteristics

The horizontal axis of this graph indicates the number of times the polarisation reversed, while the ordinate shows the polarisation charge. Fatigue characteristics are reported to be highly dependent on the operating voltage value, with deterioration occurring faster at higher operating voltages [11]. For FeRAM, data rewriting is necessary not only when writing but also when reading; this results in an increase in the number of polarisation switching cycles. Considering the retention described above as a FeRAM

operation mode, ideally write/read should be operated with a voltage as low as possible.

3. Relaxation Characteristics. Up to now, a hysteresis characteristic of a ferroelectric capacitor has been considered ideal and its time dependency neglected. A real hysteresis characteristic follows the curve depicted in Figure 2.10. At V_F = 0V where the point of remanent polarisation is, the polarisation charge decreases a little bit in dependence of time, this means P_R decreases from 'F' to 'A' and from 'C' to 'D' in Figure 2.10. respectively. This is a short term decrease in Q while the retention characteristics describe the loss of Q over a long period of time.

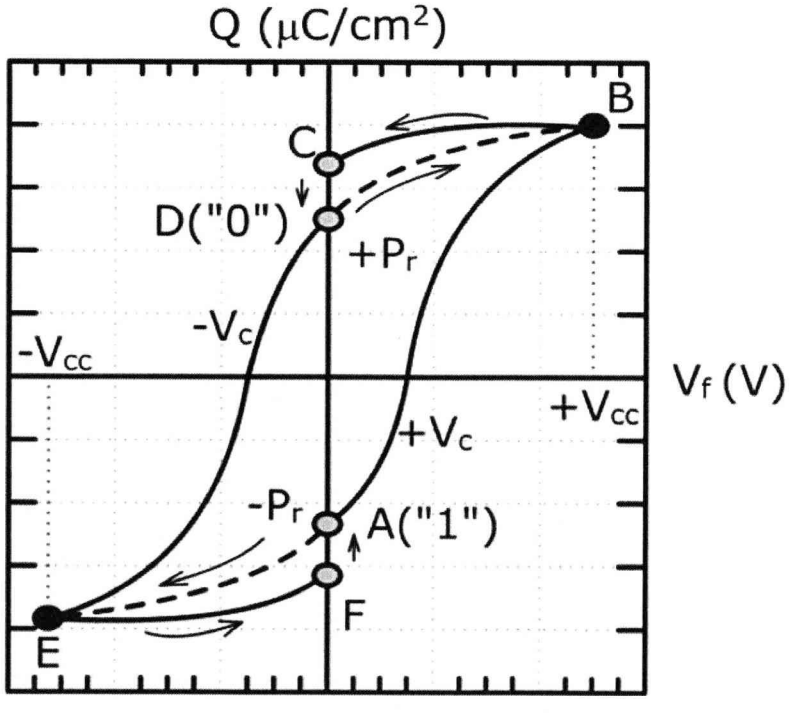

Figure 2.10: Hysteresis loop

2.1.5 Electrode Materials for Ferroelectric Capacitors

In an integrated ferroelectric thin film memory, top and bottom electrodes are required to switch the memory device between two polarisation states on the application of an electric field. Importance of electrodes cannot be underestimated as they greatly affect device performance in terms of microstructure and properties. Choice of an electrode material is governed by many factors, summarised as follows:

- Sufficiently low electrical resistance.
- Chemical compatibility with the underlying semiconductor and ferroelectric.
- Adequate adhesion to the ferroelectric film and other components in contact.
- Morphological stability under processing conditions.
- Ability to act as diffusion barrier.
- Ability to control the microstructure and properties of the ferroelectric.

Based on the above criteria, they can be broadly divided into two categories of materials: metals and oxides. Most common ferroelectric

materials such as PZT and SBT are deposited under highly oxidising conditions so it becomes necessary for the bottom electrode to be stable under these conditions. This is a major limiting factor upon the choice of electrode. This research investigates the deposition of thin film SBT with a metal electrode (Pt) for the reasons stated in the forthcoming sections.

2.1.5.1 Metal Electrodes

Conducting metal electrodes has been the most popular choice due to the ease of deposition. Figure 2.11 shows a plot between partial pressure of oxygen and temperature, which highlights the stability conditions of different metals as compared with their oxides [12]. It is evident that the choice is limited to few noble metals such as Pt, Au or Ag. However, Ag and Au react with the ferroelectric perovskites during their processing, which limits their use. This makes Pt the only feasible choice for the electrode material. Pt has been extensively used as the bottom electrode for ferroelectric thin films.

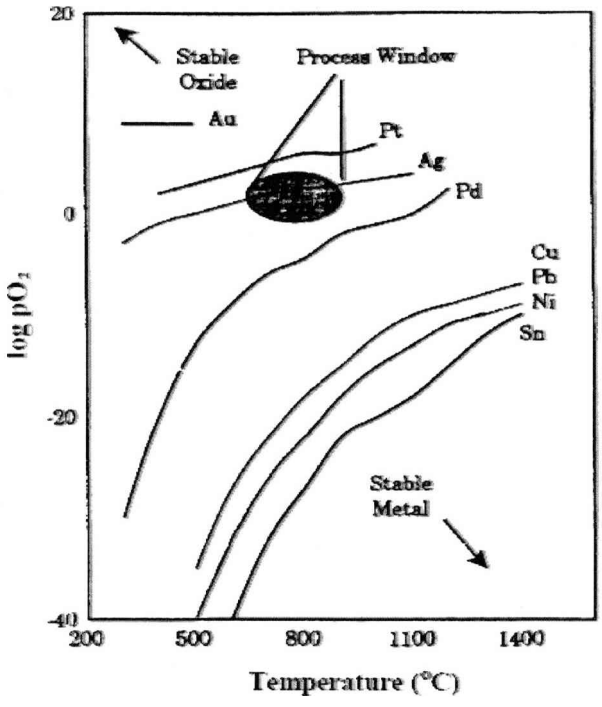

Figure 2.11: Stability regime of many metal electrodes with respect to their oxide in the FeRAM processing conditions [12]

Usually Ti (and sometimes Ta) has been used as an intermediate layer to improve the adhesion between Pt and underlying SiO_2 layer. However, Pt/Ti electrodes suffer from two major drawbacks:

1. Formation of hillocks due to stress relief in Pt films, leading to capacitor shorting.

2. Pt/Ti interactions leading to alloy or compound formation such as TiO_2, Pt_3Ti, Ti_5S_3.

This hillock and compounds formation can lead to significant changes in the morphology and microstructure of thin films [12].

2.1.5.2 Oxide Electrodes

An alternative to Pt electrodes for FeRAM applications has evolved in the form of conducting oxide electrodes. It was shown that PZT films deposited on $Yba_2Cu_3O_7$ (YBCO) bottom electrodes did not suffer from fatigue [13]. Additionally, oxide electrodes are morphogically stable during ferroelectric film processing and do not suffer from hillock formation. However, PZT films deposited on the conducting oxide electrodes exhibit comparatively lower resistivity and poorer leakage characteristics than the PZT films on Pt electrodes [12].

2.2 Ferroelectric Thin Film Materials

For FeRAM device applications, an ideal candidate material should have the properties mentioned in Section 2.1.3. Of the hundreds or even thousands of known ferroelectric materials, only few are suitable for switching applications and be integrated into semiconductor technology. Research towards the development of memory materials has been continuous and growing since the 1950s. First generation materials were KNO_3, $Bi_4Ti_3O_{12}$ (in DRAMs and FEFETs), $BaMgF_4$ (in FEFETs) [14,15]. In particular, KNO_3 thin films possessed a very high remanent polarisation and well defined coercive fields but its hygroscopic nature makes it incompatible with standard IC processing technology. A review of the ferroelectric properties of these materials can be read elsewhere [16]. Later, $PbZr_xTi_{1-x}O_3$ (PZT) emerged as a promising candidate for these applications [17]. However, PZT films on metal electrodes suffer from fatigue (i.e. drastic loss in the remanent polarisation) upon cyclic switching for 10^{10} switching cycles. Moreover, PZT films are difficult to fabricate with controlled stoichiometry due to the presence of lead because of its high volatility under PZT processing conditions. It also leads to severe processing complications including environmental hazard issues and contamination problems.

Bismuth layered perovskite oxides such as $SrBi_2Ta_2O_9$ (SBT) emerged as the next generation materials after PZT as SBT thin films do not suffer from fatigue on Pt coated Si substrates [18]. This paved the path for a new area of research into the field of ferroelectric memory devices. However, some serious problems with SBT were present, such as lower remanent polarisation in the polycrystalline state. Also, high structural anisotropy in ferroelectric properties make it essential to grow highly epitaxial SBT films in an appropriate orientation, an important issue to be managed. The present study focuses on the growth of epitaxial SBT thin films with different deposition techniques. SBT is discussed in detail in subsequent sections with respect to its crystal structure, properties, current research into SBT thin film deposition, and unsolved issues with SBT thin films.

2.2.1 Strontium Bismuth Tantalate (SBT) Thin Films

Stoichiometric SBT is defined as $SrBi_2Ta_2O_9$, an attractive alternative to PZT because it was shown that SBT films deposited on Pt did not suffer from fatigue, as illustrated in Figure 2.12 [18]. Additionally SBT films demonstrated longer polarisation retention and possessed the ability to maintain good electrical properties even when the SBT film was less than 100 nm thick.

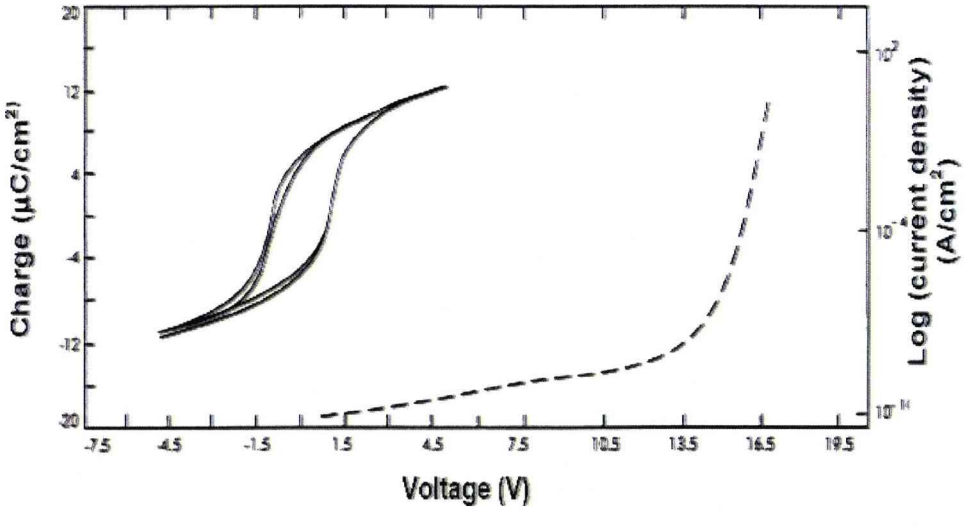

Figure 2.12: Solid curves shows the hysteresis loop of a SBT film on Pt/Si before and after switching for 10^{12} cycles. Dashed curve is a plot of leakage current versus voltage in a 240 nm thick $SrBi_2Ta_2O_9$ film at 293K. At intended operating voltage of 5V leakage current is 1.0 nA/cm^2 [18]

SBT belongs to the category of Bi-layered perovskite oxides, a family of Aurivillius phases with the general formula $(Bi_2O_2)^{2+}$ $(A_{n-1}B_nO_{3n+1})^{2-}$ where A is an alkaline earth element (e.g. Sr, Ca, Ba), B is a tetravalent or pentavalent element (e.g. Ta, Nb, Ti), and n denotes the number of perovskite units sandwiched between bismuth oxide layers, varying from 2 to 5 (for SBT, n is 2 as can be seen from the general formula) [19].

It is well known that SBT is ferroelectric at room temperature and its room temperature structure is orthorhombic. Its space group is $A2_1am$ and the primitive unit cell of SBT contains 28 atoms with two formula units. The crystal structure of SBT is schematically shown in Figure 2.13 [18].

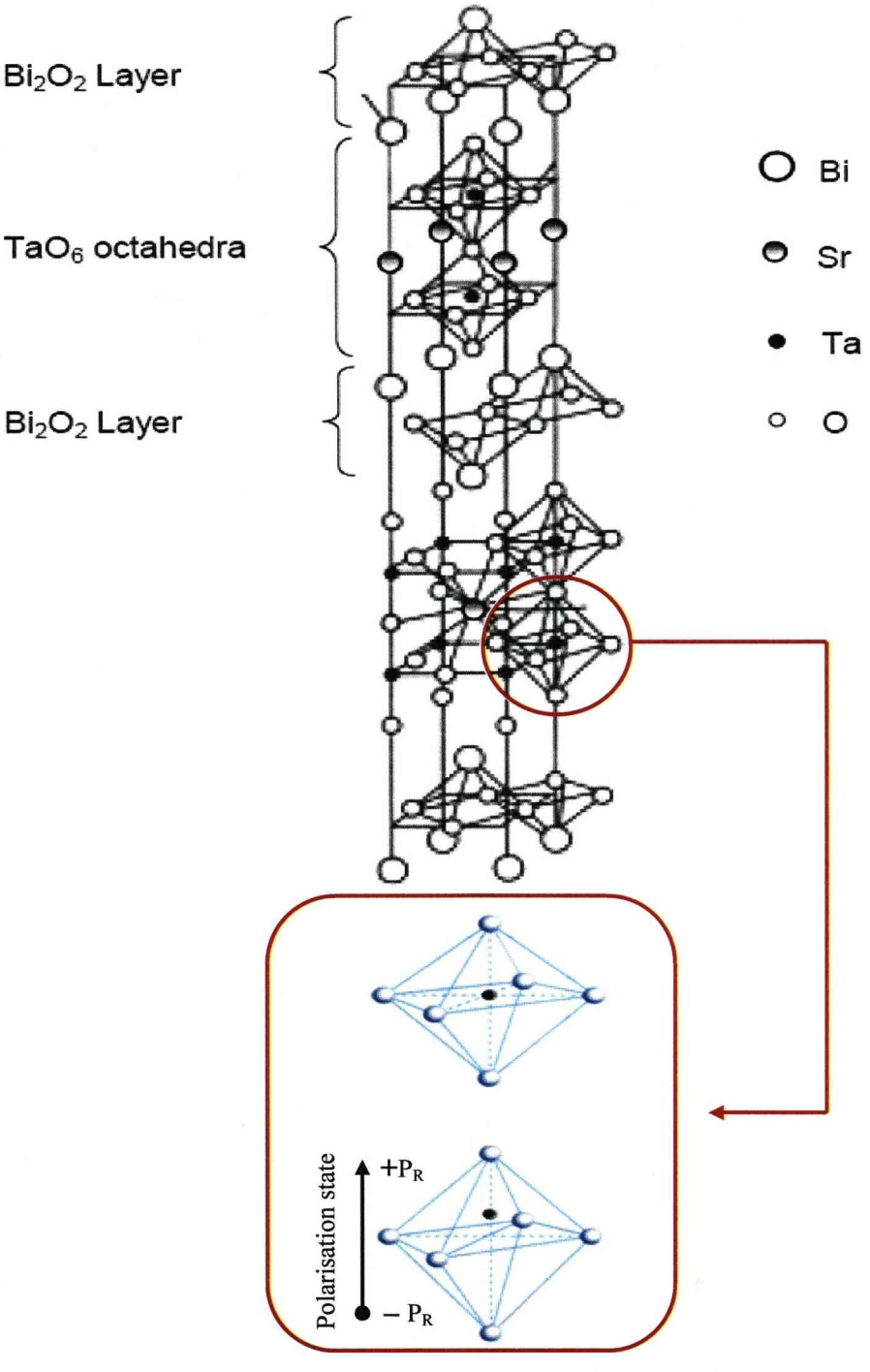

Figure 2.13: Crystal structure of SBT illustrating TaO_6 octahedra sandwiched between Bi_2O_2 layers. The polarisation state is highlighted in the red close-up box where the Ta is displaced above the oxygen plane [18].

The lattice constants of this unit cell are a = 5.531Å, b = 5.534Å, and c = 24.98Å, and as observed from these lattice constants, the structure of SBT is highly anisotropic [20]. This high degree of structural anisotropic in SBT results in high degree of anisotropic in ferroelectric properties. Most importantly is its remanent polarisation. It has been reported that the remanent polarisation is negligible along the c-axis and is maximum along the a-axis [21]. In SBT, ferroelectricity arises from the structural distortion due to the transition from paraelectric phase, which is tetragonal, to the room temperature ferroelectric phase. This transition occurs at 608K (i.e. Curie temperature). Distortion takes place in two ways: first, the atomic displacements along the orthorhombic a-axis from the corresponding positions in the parent tetragonal structure, and second, the rotation of TaO_6 octahedral around the c- and a-axes. The first factor is responsible for the spontaneous polarisation along the a-axis. In contrast, displacements along the b- and c-axes are cancelled due to the presence of glide and mirror planes, respectively, and thus they do not contribute to the total polarisation (see Figure 2.13).

The absence of fatigue in SBT has been probed by many research groups. It has been concluded that the high mobility of oxygen vacancies leads to improved fatigue resistance [22,23]. Furthermore, weak domain wall

pinning could be the reason for the absence of electrical fatigue in the SBT films [24]. Weak domain wall pinning in SBT can be viewed as a self-recovery mechanism during bipolar switching which helps in the rejuvenating of remanent polarisation. The weak domain wall pinning has been attributed to two factors: smaller magnitude of the remanent polarisation in SBT which results in the weaker charge trapping and/or lower charge density at the domain boundaries compared to PZT. Another factor is relatively low oxygen vacancy concentration in the perovskite sub-lattice in the SBT unit cell.

Additionally, an important aspect of SBT is the improvement in the ferroelectric properties of SBT by altering its composition. It has been shown that Bi-excess and Sr-deficient SBT films possess higher remanent polarisation and lower coercive field as compared to the stoichiometric films [25,26]. This is due to larger distortion in the TaO_6 octahedra because of substitution of larger Sr^{2+} ions by smaller Bi^{3+} ions [21]. Authors also reported the theoretical remanent polarisation of stoichiometric polycrystalline SBT to be about 18 $\mu C/cm^2$. The remanent polarisation of SBT can be increased up to 20 $\mu C/cm^2$ by substitution of Ta with Nb [27,28]. This increase has been attributed to the enhanced structural distortion due to stronger covalent interaction of bonds in the

octahedral unit after substitution of Ta with Nb. However, this substitution leads to a substantial increase in the coercive field, making the Nb doped SBT less attractive. For a solid solution of SBT-SBN, $SrBi_2Ta_{1-x}Nb_xO_9$, coercive field increases up to three times at x=1 compared to the value at x=0.

2.3 Epitaxial Oxide Thin Films

Although research into oxide thin films has continued since the 1960s, it was the discovery of high temperature superconductivity in 1986 [29], which provided a major impetus to the research in the field of multi-component complex oxide thin films. Consequently, many areas of interest have emerged such as ferroelectric devices, optoelectronic devices, CMR devices etc (see Table 2.1). These oxides are the subject of scientific studies because they represent immense promise for the 21st century solid-state devices. Although in the past these materials have been used as bulk material for many applications, it is the thin film form of these oxides, which makes them more attractive for various applications. For example, integration of semiconductor technology with epitaxial metal oxide thin films such as superconducting oxides is a very promising field of research for many device applications.

Property	Materials	Application
High temperature superconductivity	$YBa_2Cu_3O_7$, $Bi_mSr_2Ca_{n-1}Cu_nO_{2n+m-2}$	Power transmission, Communications, Microwave Devices
Ferroelectricity, Piezoelectricity	$Pb(Zr_xTi_{1-x})O_3$, $SrBi_2Ta_2O_9$	Memories, Data Storage Devices, Sensors, Actuators
Optics	Nb_2O_5-SiO_2-Na_2O-Ba_2O_3-TiO_2	All optical switching devices
Magnetism	$(La_xCa_{1-x})MnO_3$, Ferrites, Garnets	Magnets (hard and soft), Tunnel junctions
Thermal barrier coatings	ZrO_2, Al_2O_3	Heat resistant coatings e.g. for heat exchangers

Table 2.1: Important oxides and their applications [29]

The growth of epitaxial metal oxides on single crystal substrates usually requires temperatures higher than those in the processing of semiconductor devices. It still remains a major challenge for most of the thin film processing groups to bring the deposition temperature down to acceptable limits. Ideally, a manufacturing process for fabricating metal oxide thin films should have:

1. Capability to produce highly oriented films in a reproducible manner at lowest possible deposition temperatures,
2. Ability to produce stoichiometric films of complex compositions,
3. Compatibility with the integrated Si circuit with respect to the deposition temperature,
4. Ability to produce uniform thickness with good conformal coverage,
5. Ability to produce patterned and layered heterostructures in a reproducible way,
6. Low cost operation system.

In later sections, different processing techniques are discussed with primary emphasis on liquid-injection MOCVD and atomic layer chemical vapour deposition ALCVD.

2.3.1 Major Issues

Even though thin film deposition of epitaxial metal oxides has been researched since the 1960s and significant progress has been made of all fronts, there are several fundamental issues yet to be dealt with. To reduce the deposition temperature for depositing epitaxial films is the foremost challenge for most of the processing techniques, barring some chemical processes. Other aspects involve production of stable phases with precise composition and correct oxygen content, good structure and morphology of the films, high degree of desired orientation, and issues regarding the nucleation and growth of the films. Choice of device compatible and cheap substrates and deposition over larger area substrates are the main bottlenecks in the commercial success. The interdependence of various parameters, for example processing temperature and epitaxy, poses serious questions regarding the choice of optimum conditions. In this section, it has been attempted to briefly elucidate these problems and the on-going efforts to handle them.

2.3.1.1 Deposition Temperature and Orientation

Most of the metal oxides require high temperature for epitaxial growth, usually growth temperatures being 700 – 800°C, extremely high when compared to epitaxial growth temperatures of metals and semiconductors which fall usually between 200 – 500°C. These temperatures are very high when considering the processing compatibility with semiconductor circuit processing. The effect of deposition temperature is direct on the epitaxy, although it also depends upon the type of processes. Usually if the deposition temperature is lowered, then the degree of epitaxy deteriorates. However, there are few reports of deposition at lower temperatures by MOCVD processes [30].

2.3.1.2 Phase Stability and Stoichiometry Control

Due to thin film growth processes in general being non-equilibrium in nature, it becomes very important to have knowledge regarding phase evolution under a given set of process parameters and how a desired phase can be obtained if they are altered accordingly. This problem arises predominantly in terms of deposition temperature and oxygen activity.

Most perovskite oxides are not only complex oxides, but they also have some specific oxygen level for desired properties. These complexities put enormous restriction on the processing conditions to produce the correct phase. Chemical complexity of these oxides also illustrates problems regarding the correct stoichiometry of the films.

This is particularly difficult in some processes, however, metal organic chemical vapour deposition (MOCVD) has emerged as one of the most promising processes to address this problem with considerable success and it has been demonstrated successfully that films can be deposited without any loss of stoichiometry [31]. Figure 2.14 known as the Ternary phase diagram illustrates the stable phases in the SBT system [32,33]. The reference point for stoichiometric Aurivillius SBT is $SrBi_2Ta_2$. The dashed line passes through the stoichiometric $SrBi_2Ta_2$ point and corresponds to varying Bi content with Sr/Ta remaining constant.

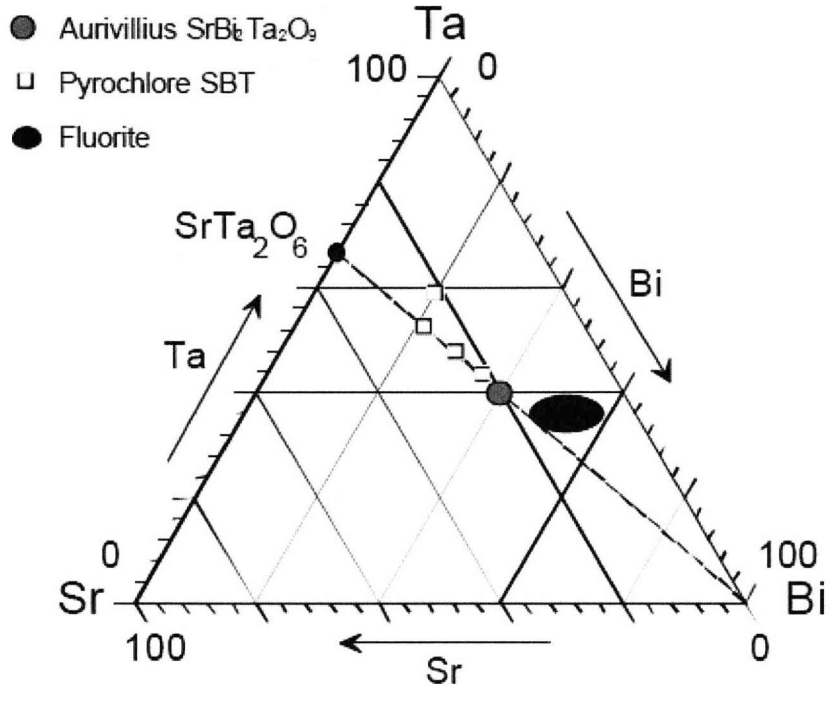

Figure 2.14: Ternary Phase diagram of SBT illustrating the stable phases in the SBT system where the dashed line passes through the stoichiometric $SrBi_2Ta_2O_\delta$ ($6 < \delta < 9$) point and corresponds to varying Bi content with Sr/Ta remaining constant [32].

2.3.1.3 Substrate Effects

The most important factor affecting epitaxy is the nature of the substrate. The substrate for the epitaxial films should essentially be a single crystal substrate. The choice of substrate is limited by various factors such as crystal symmetry, orientation, lattice parameter, surface energy considerations, surface finish, chemical nature, coefficient of thermal

expansion and most importantly, the application for which the film is being deposited. In particular, thermal expansion mismatch between the substrate and the thin film is particularly important. A high degree of thermal mismatch causes the generation of either tensile or compressive strains in the film during cooling back down to ambient temperatures. If these are sufficiently large, the thin film may crack or delaminate. Substrate preparation is also an important step towards depositing epitaxial films. In many instances, surface contamination can lead to dramatic changes in the epitaxy.

2.4 Ferroelectric Thin Film Deposition Techniques

Deposition technology can be regarded as the major key to the creation of devices such as computers, since microelectronic solid-state devices are based on material structures created by thin-film deposition. Electronic engineers have continuously demanded films of improved quality and sophistication for solid-state devices, requiring a rapid evolution of deposition technology. Equipment manufacturers have made successful efforts to meet the requirements for improved and more economical deposition systems and for in situ process monitors and controls for measuring film parameters. An additional reason for the rapid growth of deposition technology is the improved understanding of the physics and chemistry of films, surfaces, interfaces, and microstructures made possible by the remarkable advances in analytical instrumentation during the previous twenty years. A better fundamental understanding of materials leads to expanded applications and new designs of devices that incorporate these materials.

There are numerous deposition technologies for material formation. Since the concern is with thin-film deposition methods for forming layers in the thickness range of a few nanometres to about ten micrometres, the task of

classifying the technologies is made simpler by limiting the number of technologies to be considered. Basically, thin-film deposition technologies are either purely physical, such as evaporative methods, or purely chemical, such as gas and liquid-phase chemical processes. A considerable number of processes that are based on glow discharges and reactive sputtering combine both physical and chemical reactions; these overlapping processes can be categorised as physical-chemical methods. The following is a brief description of the principles, salient features, applications, and selected literature references of the more important technologies for thin-film deposition and formation.

The thin films investigated in this thesis were all grown on liquid injection MOCVD reactors. Further details of the technique and development work carried out are presented in Chapter 3.1.

2.4.1 Evaporative Technologies

Although evaporative technology is one of the oldest techniques used for depositing thin films, thermal evaporation or vacuum evaporation, it is still widely used in the laboratory and in industry for depositing metal

and metal alloys. When depositing, the following sequential basic steps occur: (1) a vapour is generated by boiling or subliming a source material, (2) the vapour is transported from the source to the substrate, and (3) the vapour is condensed to a solid film on the substrate surface.

2.4.1.1 Molecular Beam Epitaxy (MBE)

Molecular beam epitaxy (MBE) is a sophisticated, finely controlled method for growing single-crystal epitaxial films in a high vacuum (10^{-11} Torr) [34]. The films are formed on single-crystal substrates by slowly evaporating the elemental or molecular constituents of the film from separate Knudsen effusion source cells (deep crucibles in furnaces with cooled shrouds) onto substrates held at a temperature appropriate for chemical reaction, epitaxy, and re-evaporation of excess reactants. The furnaces produce atomic or molecular beams of relatively small diameter, which are directed at the heated substrate, usually silicon or gallium arsenide. Fast shutters are interposed between the sources and the substrates. By controlling these shutters, one can grow superlattices with precisely controlled uniformity, lattice match, composition, dopant

concentrations, thicknesses, and interfaces down to the level of atomic layers.

The most widely studied materials are epitaxial layers of III-V semiconductor compounds, however, silicon, metals, silicides and insulators can also be deposited as single-crystal films by this versatile and uniquely precise method. Complex layer structures and superlattices for fabricating gallium arsenide hetero-junction solid-state lasers, discrete microwave devices, optoelectronic devices, wave-guides, monolithic integrated optic circuits, and totally new devices, have been created. An additional important advantage of MBE is the low temperature requirement for epitaxy, which for silicon is in the range of 400°C – 800°C, and for gallium arsenide 500°C – 600°C. Several production systems with associated analytic equipment are now available [34]. The extremely limited product throughput, the complex operation, and the expensive equipment are, at present, the major limitations of this promising deposition technology for production applications.

2.4.2 Glow-Discharge Technologies

The electrode and gas-phase phenomena in various kinds of glow discharges (especially rf discharges) represent a rich source of processes used to deposit and etch thin films. Creative exploitation of these phenomena has resulted in the development of many useful processes for film deposition (as well as etching).

2.4.2.1 Plasma Deposition of Inorganic/Organic Films

Plasma deposition of inorganic films and plasma polymerisation of organic reactants to produce films of organic polymers involve the introduction of a volatile reactant into a glow discharge, which is usually generated by an rf force [34]. The reactant gases or vapours are decomposed by the glow discharge mainly at surfaces (substrate, electrodes, walls), leaving the desired reaction product as a thin solid film. Plasma deposition is a combination of a glow-discharge process and low-pressure chemical vapour deposition, and can be classified in either category. Since the plasma assists or enhances the chemical vapour deposition reaction, the process is usually denoted as PACVD or

PECVD. The possibilities for producing films of various materials and for tailoring their properties by judicious manipulation of reactant gases or vapours and glow-discharge parameters are very extensive. Plasma deposition processes are used widely to produce films at lower substrate temperatures and in more energy-efficient fashion than can be produced by other techniques. For example, they are widely used to form secondary-passivation films of plasma silicon nitride on semiconductor devices, and to deposit hydrogenated, amorphous silicon layers for thin-film solar cells. Debris particles falling from the rf electrode onto the substrate, produced from the plasma is one of the disadvantages of this technique. In addition, thickness uniformity across large substrates may also be poor in comparison with atomic layer chemical vapour deposition (ALCVD).

2.4.2.2 Physical Vapour Deposition (PVD)

Physical vapour deposition (PVD) are atomistic deposition processes in which material is vaporised from a solid or liquid source in the form of atoms or molecules, transported in the form of a vapour through a vacuum or low pressure gaseous (or plasma) environment to the substrate

where it condenses. To attain target evaporation, the following steps are performed; electron-beam (e-beam), pulsed laser (PLD), plasma spray and sputtering. Ion-beam sputtering is possibly the most common PVD technique, whereby a source of ions is accelerated towards the target to generate a flux. A third electrode can be added to increase deposition rates by generating more electrons for ionisation. However, magnetron sputtering refers to the process of utilising a magnetic field to capture and spiral electrons in the vicinity of the target. This process is advantageous as the thin film deposited by sputtering is exceptionally rapid (~1μm/min). However, charge damage of the surfaces is due to ion bombardment and the method is not normally applied to thin ferroelectric layers.

2.4.3 Gas-Phase Chemical Processes

Methods of film formation by purely chemical processes in the gas or vapour phases include chemical vapour deposition and thermal oxidation. Chemical vapour deposition (CVD) is a materials synthesis process whereby constituents of the vapour phase react chemically near or on a substrate surface to form a solid product [35]. The deposition technology

has become one of the most important means for creating thin films and coatings of a large variety of materials essential to advanced technology, particularly solid-state electronics where some of the most sophisticated purity and composition requirements must be met. The main feature of CVD is its versatility for synthesising both simple and complex compounds with relative ease at generally low temperatures. Both chemical composition and physical structure can be tailored by control of the reaction chemistry and deposition conditions. Fundamental principles of CVD encompass an interdisciplinary range of gas-phase reaction chemistry, thermodynamics, kinetics, transport mechanisms, film growth phenomena, and reactor engineering.

Chemical reaction types basic to CVD include pyrolysis (thermal decomposition), oxidation, reduction, hydrolysis, nitride and carbide formation, synthesis reactions, disproportionation, and chemical transport. A sequence of several reaction types may be involved in more complex situations to create a particular end product. Deposition variables such as temperature, pressure, input concentrations, gas flow rates and reactor geometry and operating principle determine the deposition rate and the properties of the film deposit. Most CVD processes are chosen to be heterogeneous reactions. That is, they take

place at the substrate surface rather than in the gas phase. Undesirable homogeneous reactions in the gas phase nucleate particles that may form powdery deposits and lead to particle contamination instead of clean and uniform coatings. The reaction feasibility (other than reaction rate) of a CVD process under specified conditions can be predicted by thermodynamic calculations, provided reliable thermodynamic data (especially the free energy of formation) are available. Kinetics control the rate of reactions and depend on temperature and factors such as substrate orientation. Considerations relating to heat, mass, and momentum transport phenomena are especially important in designing CVD reactors of maximum efficiency. Since important physical properties of a given film material are critically influenced by the structure (such as crystallinity), control of the factors governing the nucleation and structure of a growing film is necessary.

2.4.3.1 Metal Organic Chemical Vapour Deposition (MOCVD)

The growth of thin layers of compound semiconducting materials by the co-pyrolysis of various combinations of organometallic compounds and hydrides, known generically as metal organic chemical vapour deposition

(MOCVD), has assumed a great deal of technological importance in the fabrication of a number of opto-electronic and high speed electronic devices. The initial demonstration of compound semiconductor film growth was first reported in 1968 and was initially directed towards becoming a compound semiconductor equivalent of "Silicon on Sapphire" growth technology [36]. Since then, both commercial and scientific interest has been largely directed toward epitaxial growth on semiconductor rather than insulator substrates. State-of-the-art performance has been demonstrated for a number of categories of devices, including lasers, PIN photo-detectors, solar cells, phototransistors, photo-cathodes, field effect transistors and modulation doped field effect transistors. The efficient operation of these devices requires the grown films to have a number of excellent material properties, including purity, high luminescence efficiency, and/or abrupt interfaces.

Figure 2.15 highlights the process stages occurring in MOCVD. Using a thermally decomposed chemical precursor at the substrate surface, together with oxygen will form metal-oxide layers. Typically, the required pressures to undergo this process lie between ~1 mbar and

atmospheric. Below is an illustration of the key stages of the aforementioned process:

1. An inert gas is used to deliver the precursor to the heated substrate.
2. Precursor is thermally decomposed with the presence of oxygen to form a metal oxide thin film on the substrate.
3. Using the transport gas stream to extract produced reaction products.

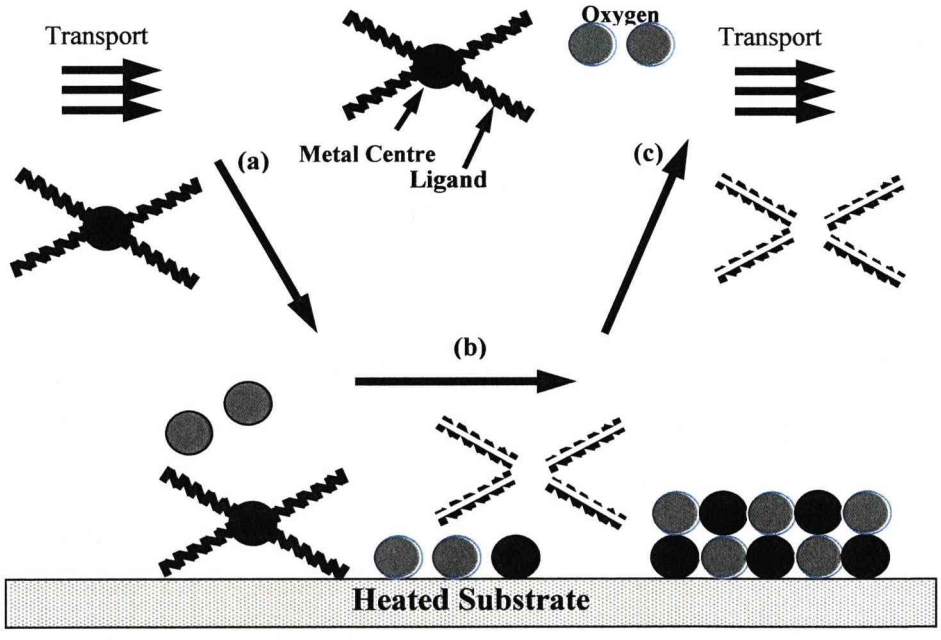

Figure 2.15: Metal organic chemical vapour deposition (MOCVD)

Commonly, precursor molecules contain a metal atom which is surrounded by organic ligands that plays a significant role. Precursor molecule is assisted by the ligands to exist stably in the gas phase without decomposing and with sufficient vapour pressure to allow adequate mass transport to the substrate. Therefore, thermal decomposition of the precursor occurs, forming a metal oxide film. There are two oxygen sources present, either as a gas form added in the reactor or from the metal-organic molecule itself, which is liberated during decomposition.

Precursor decomposition taking place with the absence of huge quantities of carbon and other contaminants, will guarantee higher film qualities. Consequently, to achieve a successful film growth, choices of precursor and precursor chemistry are vital. The above description briefly outlines the basics of the MOCVD technique, however, there are further influential elements impacting on film growth and quality emphasised below:

- Gas flow and composition
- Cleanliness of system and substrate
- Purity of precursor
- Surface effects, nucleation, adsorption and desorption

- Gas phase reactions
- Temperature
- System pressure and precursor partial pressure
- Precise and repeatable reactor control
- Precursor operating temperature windows to enable reliable and repeatable precursor transportation and decomposition

Using a 'bubbler', containment of precursors takes place where it exists as a liquid or is diluted in a liquid inside a sealed vessel. Inert gas is bubbled through the vessel and precursor vapour is transported via the inert carrier gas to the reaction chamber. In order to avoid condensation, bubblers and lines are normally heated, and the system will often be run at low pressure to assist volatilisation.

Using MOCVD as a method of growing films is beneficial as it ensures: good film uniformity over large areas and films of high quality, in addition to high growth rates for semiconductor applications. Nonetheless, thin films at the atomic level are difficult to control and often must be post-annealed to achieve correct stoichiometry and morphology, which is a drawback to this process.

2.4.3.2 Liquid Injection MOCVD

MOCVD has been adapted by replacing the precursor bubbler with a pulsed liquid injection system of automotive origin. An adequate volatile solvent is used to dissolve the precursor. This step is advantageous as relatively non-volatile or temperature sensitive precursors can be used. This technique has extended the range of precursors available to film growers since it would be impossible to use a conventional bubbler. Rapid, precise and flexible precursor metering occurs when utilising pulsed liquid injection, which can later be exploited to grow unique thin film structures such as nano-laminates. The potential exists for controlling composition at the atomic level to form original materials and structures, not thermodynamically favoured, thus cannot be made by alternative methods [37,38].

2.4.3.3 Atomic Layer Chemical Vapour Deposition (ALCVD/ALD)

A low-pressure coating technique, which has recently increased in popularity, is known as atomic layer chemical vapour deposition (ALCVD) and usually referred to as atomic layer deposition (ALD). It

encompasses cyclic chemical reactions between precursor active species and surface bonded hydroxyl groups. Deposition of precise thin film thickness with good uniformity and step coverage can be achieved [39,40]. Figure 2.16 illustrates the process whereby a four-coordinate simple chloride precursor as an example to show the chemical reactions occurring. Firstly, (Figure 2.16 (a)) via an inert carrier gas, a pulse of precursor vapour is transported to the heated substrate on which hydroxyl groups are present at its surface. Secondly, (Figure 2.16 (b)) reaction occurs between the precursor chloride groups with the surface hydroxyls, causing the precursor to bond to the surface. As a result, hydrogen chloride is liberated as reaction products. The precursor possesses two oxygen groups at that stage; bonding the metal atom to the surface, and two outward facing the chloride groups. A pulse of water vapour is introduced in the final two stages (Figure 2.16 (c) and (d)) which reacts with chloride groups to form hydroxyls and liberates hydrogen chloride.

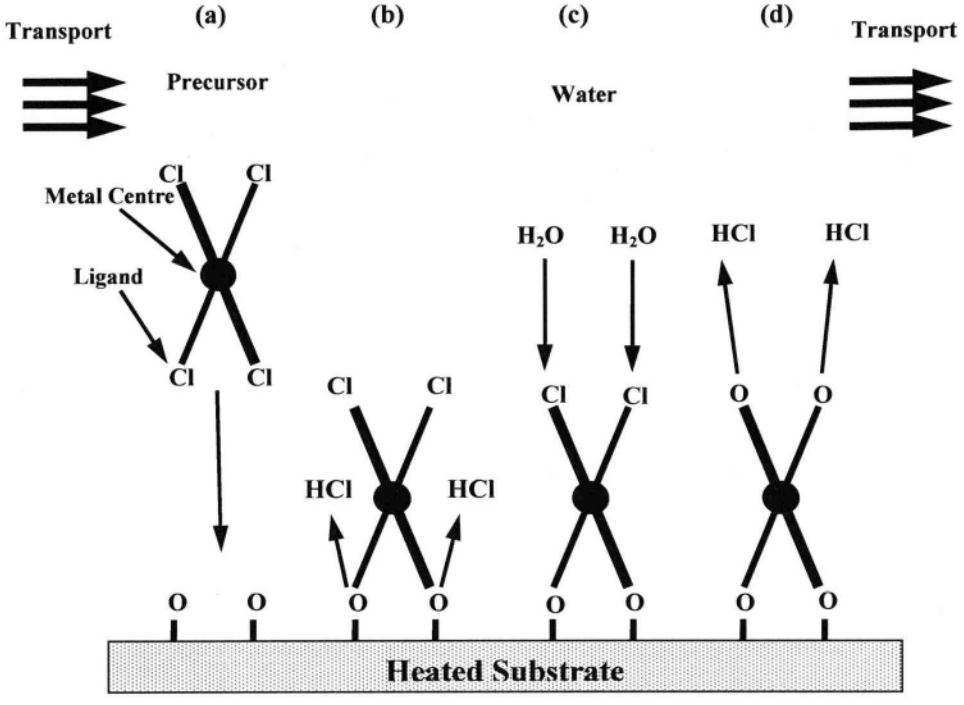

Figure 2.16: Atomic layer chemical vapour deposition (ALCVD)

The distinctive feature of ALD is that the reactions are saturative (Figure 2.17). This makes the film growth self-limiting that, in turn, gives the method a number of advantages as summarised in Table 2.2. The self-limiting growth ensures that each cycle (possibly excluding the very first cycles) deposits the same amount of material on all surfaces independent of the precursor dose received as long as the dose is high enough to saturate the reactions. Consequently, the ALD method offers excellent large area uniformity and conformity. In addition, film thicknesses are

accurately controlled simply by the number of deposition cycles applied. This makes it also straightforward to tailor film composition at an atomic layer level. Preparation of multicomponent and multiplayer materials is further facilitated by the fact the process temperature windows are often reasonably wide so that binary processes are easy to combine [41,42].

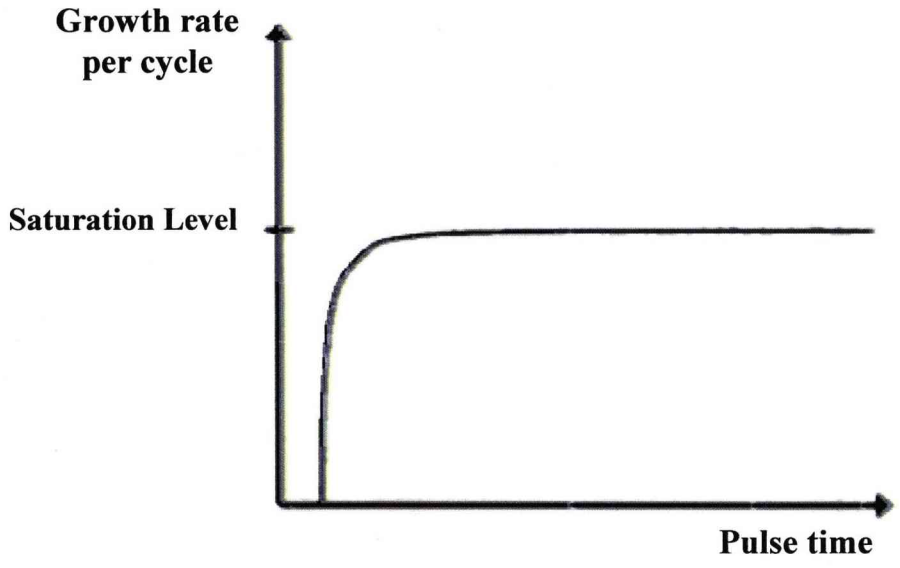

Figure 2.17: illustrates growth rate/cycle versus pulse time and the point of saturation

Characteristics feature of ALD	**Implication for film disposition**	**Practical advantages**
Self-limiting growth process	Film thickness is dependent only on the number of deposition cycles	Accurate and simple thickness control
	No need for reactant flux homogeneity	Large area and batch capability Excellent conformity No problems with inconstant vaporisation of solid precursors
	Atomic level control of material composition	Capability to produce sharp interfaces, nanolaminates, and superlattices
Separate dosing of reactants	No gas phase reactions	Allows use of precursors highly reactive towards each other, thereby enabling effective precursor utilisation and short cycle times
	Sufficient time is given to complete each reaction step	High quality materials are obtained at low deposition temperatures
Wide processing temperature windows	Processing conditions of different materials are readily matched	Easy preparation of multilayer structures in a continuous process

Table 2.2: Advantages of ALD technique

Precautions must be considered so that ALD precursors are not thermally decomposed at the operating temperature used, otherwise CVD type

processes will occur. Depending on precursor thermal stability, ALD temperatures will range between 150°C to 300°C. For very thin films (<10 nm) this method is useful where fine control and accuracy are paramount. However, this technique is impractical for thicker films due to long deposition times.

2.4.3.4 Jet Vapour Deposition (JVD)

Jet vapour deposition is a patented, novel technique for depositing thin films of a variety of metals, semiconductors, dielectrics, and organics. Figure 2.18 (a) is a schematic diagram of a JVD system, and Figure 2.18 (b) shows its key feature; jet vapour source. The jet vapour source consists of a dual-nozzle, through which a supersonic jet of a light carrier gas, such as He, is formed. Kinetic energy liberated by the precursor and carrier gas jet impacting the surface is sufficient to cause oxide film formation. Systems operate with the jet fixed, moving the substrate underneath in a raster pattern [43].

The major advantages of the JVD are; high impact energy promoting film adhesion and making it possible to grow films at room temperature. The

deposition rate can be precisely controlled from below 1 monolayer per minute to as high as 10 microns per minute by adjusting the gas injection parameters. The drawback to this process is the irregular surface topography which leads to thickness variation as a result of local changes in gas stream kinetic energy.

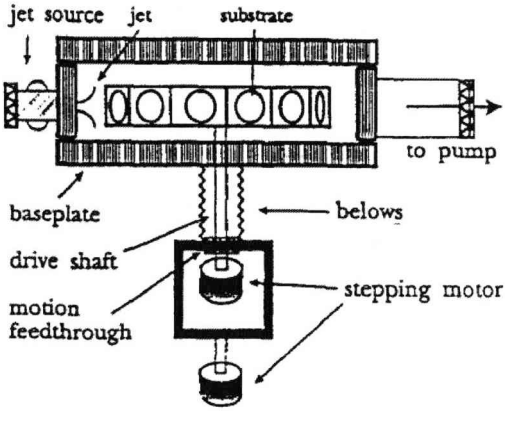

Figure 2.18 (a): Jet vapour deposition [43]

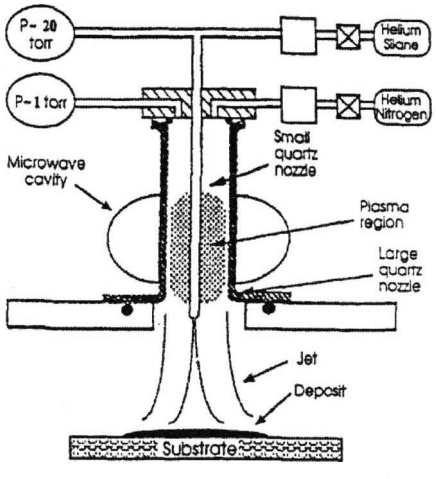

Figure 2.18 (b): Jet vapour source [43]

2.5 Superlattice Approach to the Synthesis of Ferroelectric SBT Thin Films

Ferroelectric thin films are commonly featured in a range of non-volatile ferroelectric memory applications for its highly desirable performance features [44,45,46]. These thin films provide; fatigue-free properties, large area film uniformity, conformal step coverage, high growth throughput and precise composition control. Strontium bismuth tantalate, SBT is an attractive material used in these applications [47]. The perovskite structure of SBT is recognised for its low intrinsic defect density and superior resistance to fatigue degradation [18].

Pursuing dielectric layers which demonstrated uniform stoichiometry and thickness, high dielectric constants, large breakdown fields and high conformity, stimulated the search for substitutions to the numerous deposition techniques of SBT [48]. Here are but a few depositing methods: physical vapour deposition, solution deposition (sol-gel, metal organic decomposition MOD [49]), and chemical vapour deposition [35] (MOCVD [50,51,52] and ALD [53]).

Firstly, to fully appreciate and understand the reason behind choosing a superlattice approach of depositing SBT, the positives and negatives of using alternative deposition techniques will be discussed. Chemical vapour deposition (CVD) is recognised for its importance in SBT preparation as it achieves high compositional and thickness uniform deposition over a large area with high step coverage [35]. However, for CVD to produce high-quality products, it requires high growth temperatures. Consequently the extreme temperatures damage underlying layer and polymer resists. Even when evaporation is performed at a lower temperature, the films suffer from poor conformity and poor adhesion to the substrate.

The technique of MOCVD solves the above problem. Briefly, this deposition technique is where volatile metal-organic compounds are transported in the vapour phase simultaneously and in the presence of oxygen, thermally decompose on a heated substrate [54]. MOCVD illustrates excellent conformal deposition and film uniformity, high film densities and large area growth [55] at device dimensions of less than 2 μm.

Once again, this deposition technique has severe restrictions, due to a shortage of stable and soluble metal-organic precursors and strict temperature regime. The standard precursors [56,57] exhibit varying decomposition characteristics and physical properties, resulting in bismuth incorporation inefficiency, composition control problems and poor film uniformity.

Overcoming these restrictions by using "single source" precursors e.g ($Sr\{Ta(OEt)_6\}_2$) [47,57], result in additional drawbacks. It is true that the metal : metal ratio in the precursor complements the requirements of the deposited oxide film, however, the varied volatilities of ($Sr(OR)_2$) and ($Ta(OR)_{5)}$ fragments initiate detachment of the Sr and Ta components in the gas phase and deposited oxide [58]. Moreover, the precursors also contain an unsaturated Sr centre, thus are damaged by moisture and become inefficient.

As a method of improving the MOCVD, alkoxide precursors, e.g $Sr(Ta(OEt)_5(dmae))_2$ [dmae = $OCH_2CH_2NMe_2$] [59,60] and separate Bi-alkoxide co-precursor, $Bi(mmp)_3$ [mmp=($OCMe_2$-CH_2OMe)] [61] are inserted into the heterometal alkoxide, hence, inhibiting gas-phase

dissociation, decreasing the air-sensitivity and representing the complexes more thermally stable.

However, this method causes an additional impediment, the simultaneous evaporation of strontium tantalate and bismuth precursors leads to competition between the incorporation of Sr and Bi in the deposited oxide [62]. In order to alleviate these problems, $SrTa_2O_6/Bi_2O_3$ superlattices (SLs) and the effect of post-deposition annealing will be investigated. An SL structure refers to the layering of the $SrTa_2O_6$ on Bi_2O_3 and works by converting the distinct layers of Bi_2O_3 and $SrTa_2O_6$ into a single layer of polycrystalline SBT post-growth annealing. With the purpose of exploring the effect of anneal temperature on the structure, crystallinity and composition of the SLs, results from MEIS, HR-TEM and XRD will be examined.

To conclude, the investigation of SL approach to SBT, the atomic layer deposition (ALD) technique will be utilised. Succinctly, ALD is a surface-controlled layer by layer deposition process, whereby gaseous precursors are sequentially dosed into a vacuum chamber under computer control [63]. To achieve controlled atomic-level deposition, ALD involves alternating, self-limiting surface reactions. Several advantages of

using ALD are the excellent thickness control and perfect step-coverage of high aspect ratio structures achieved. Unlike MOCVD, precursors in ALD react rapidly with available chemisorptions sites and are not thermally decomposed during transport or on growth surface.

2.6 References

[1] Reviewed by F. Jona and G. Shirane, *Ferroelectric Crystals*, Dover Publications, New York (1993).

[2] M. Sayer, and K. Sreenivas, *Science*, **247**, 1056 (1990).

[3] X. Yu and M. Sayer, *J. Can. Ceram. Soc.*, **55**, 1 (1986).

[4] K. Screenivas, A. Mansingh and M. Sayer, *J. App. Phys.*, **61**, 411 (1987).

[5] J.F. Scott and C.A. Paz de Arauja, *Science*, **246**, 1400 (1989); and J.F. Scott, Ferroelectric Memories, Springer Series in Advances Microelectronics-3, 2000.

[6] S. Stemmer, S.K. Streiffer, F. Ernst and M.F. Ruhle, *Phil. Mag. A*, **71**, 713 (1995).

[7] D. Damjanovic, *Rep. Prog. Phys.*, **61**, 1267 (1998).

[8] R.W. Whatmore, *Rep. Prog. Phys.*, **49**, 1335 (1986).

[9] C.B. Sawyer and C.H. Tower, *Phys. Rev.*, **35**, 269 (1930).

[10] S. Sinharoy, H. Buhay, D.R. Lampe and M.H. Francombe, *J. Vac. Sci. Tech. A*, **10** (4), 1554 (1992).

[11] *"FRAM Quality & Reliability"* a review, Fujitsu Limited (2001).

[12] H.N. Al-Shareef and A.I. Kingon, in *Ferroelectric Thin Films: Synthesis and Properties,* eds. C.A, Paz de Arauja, J.F. Scott and G.W. Taylor, **193** (1996).

[13] R. Ramesh, W.K. Chen, B. Wilkens, H. Gilchrist, T. Sands, J.M. Tarascon, V.G. Keramidas, D.K. Fork, J. Lee and A. Safari, *Appl. Phys. Lett.*, **61**, 1537 (1992).

[14] W.J. Takei, N.P. Formigoni and M.H. Francombe, *J. Vac. Sci. Tech.*, **7**, 442 (1970).

[15] S. Sinharov, H. Buhay, M.H. Francombe, W.J. Takei, N.J. Doyle, J.H. Rieger, D.R. Lampe and E. Stepke, *J. Vac. Sci. & Tech. A*, **9**, 409 (1991).

[16] M.H. Francombe and S.V Krishnaswamy, *MRS Proceedings* (Pittsburgh), **179**, 200 (1990).

[17] A. Croteau, S. Matsabura, Y. Miyasaka and N. Shobata, *Jpn. J. Appl. Phys.*, **26**, 18 (1987).

[18] C.A. Paz de Arauja, J.D. Cuchiaro, L.D. McMillan, M.C. Scott and J.F. Scott, *Nature*, **374**, 627 (1995).

[19] B. Aurivillious, *ARK. Kemi*, **1**, 463 (1949).

[20] A.D. Rae, J.G. Thompson and R.L. Withers, *Acta Crystallogr. Sect. B*, **48**, 418 (1992).

[21] Y. Shimakawa, Y. Kubo, Y. Nagakawa, T. Kamiyama, H. Asano and F. Izumi, *Appl. Phys. Lett.*, **74**, 1904 (1999).

[22] T.-C. Chem, C.-L. Thio and S.B. Desu, *J. Mater. Res.*, **12**, 2628 (1997).

[23] A.R. James, S. Balaji and S.B. Krupanidhi, *Mater. Sci Eng.*, **B64**, 149 (1999).

[24] H.N. Al-Shareef, D. Dimos, T.j. Boyle, W.L. Wareen and B.A Tuttle, *Appl. Phys. Lett.*, **68**, 690 (1996).

[25] T. Atsuki, N. Soyama, T. Yonezawa and K. Ogi, *Jpn. J. Appl. Phys.: Part I*, **34**, 5096 (1995).

[26] T. Noguchi, T. Hase and Y. Miyasaka, *Jpn. J. Appl. Phys.: Part I*, **35**, 4900 (1996).

[27] A. Furuya and J.D. Cuchiaro, *J. Appl. Phys.*, **84**, 6788 (1998).

[28] Y. Shimakawa, Y. Kubo, Y. Tauchi, T. Kamiyama, H. Asano and F. Izumi, *Appl. Phys. Lett.*, **77**, 2749 (2000).

[29] J.G. Bednorz and K.A. Muller, *Z. Phys.*, **B64**, 189 (1986).

[30] S.K. Dey and P.V. Alluri, *MRS Bulletin*, June, 37 (1996).

[31] B. Dam, J.H. Rector, J. Johansson, S. Kars and R. Griessen, *"Stoichiometric Transfer of Complex Oxides by Pulsed Laser Ablation"*, E-MRS Spring Meeting, Cola 95, Strasbourg, May 22-26 (1995).

[32] H. Bachhofer, PhD thesis, Infineon Technologies and University of Aachen and University of Regensburg, (2001).

[33] C.D Gutleben, *Mater. Res. Soc. Symp. Proc.*, **433**, 109 (1996)

[34] K. Seshan, Handbook of Thin-Film Deposition Processes and Techniques – Principles, Methods, Equipment and Applications (2nd Edition). William Andrew Publishing/Noyes (2002).

[35] T. Ami, K. Horinaka, C. Isobe, N. Nagel, M. Sugiyama, Y. Ikeda, K. Watanabe, A. Machida, K. Miura, M. Tanaka, *Mater. Res. Soc. Symp. Proc*, **415**, 195 (1996).

[36] R.A. Fischer, *Precursor Chemistry of Advanced Materials: CVD, ALD and Nanoparticles.* Birkhäuser Publisher (2005).

[37] L. M. Hitchman, A.C. Jones, M.L. Hitchman, "*Chemical Vapour Deposition: Precursors and Processes*", Royal Society of Chemistry (2009).

[38] Materials Research Society, "*Ferroelectric Thin Films: Symposium*", Materials Research Society, (2003).

[39] A. Londergan, "*Atomic Layer Deposition Applications 3*", The Electrochemical Society, (2007).

[40] T.D. Steiner, "*Semiconductor nanostructures for optoelectronic applications*", Artech House, (2004).

[41] H.S. Nalwa, "*Handbook of Thin Film Materials: Deposition and processing of thin films*", Academic Press, (2002).

[42] J.R. Groza, J.F. Shackelford, E.J. Lavernia, M.T. Powers, "*Materials processing handbook*", CRC Press, (2007).

[43] A. Pique and D.B. Chrisey, "*Direct-write Technologies for Rapid Prototyping Applications: Sensors, Electronics and Integrated Power Sources*", Academic Press Publishing (2002).

[44] A. Gensbittel, A.F. Degardin, A.J. Kreisler, M. Guilloux-Viry, A. Perrin, P. Crozat, *Ferroelectronics*, **288**, 103 (2003).

[45] G. Rosenman, D. Shur, Y.E. Krasik, A. Dunaevsky, *J. Appl. Phys,* **88** (11), 6109 (2000).

[46] R. Ramesh, S. Aggarwal, O. Auciello, *Mater. Sci. Eng. R*, **32** (6): 191 (2001).

[47] H. Funakubo, K. Ishikawa, T. Watanabe, M. Mitsuya and N. Nukaga, *Adv. Matter. Opt. Electron*, **10**, 193 (2000).

[48] G.D. Wilk, R.M. Wallace, J.M. Anthony, *J. Appl. Phys.*, **89**, 5243 (2001).

[49] T. Mihara, H. Yoshimori, H. Watanabe, C.A. Paz de Arauja, *Jpn. J. Appl. Phys.*, **34**, 5233 (1995).

[50] I.M. Watson, *Chem. Vap. Deposition,* **3**, 9 (1997).

[51] T. Li, S.B. Desu, C.H. Peng, M. Nagata, *Appl Phys Lett.*, **68**, 616 (1996).

[52] F. Felten, J.P. Senateur, F. Weiss, R. Madar, A. Abrutius, *J. Phys. IV*, France, **5**, C5-1079 (1995).

[53] M. Leskalä and M. Ritala in *Handbook of Thin Film Materials* vol 1, pp **103**, ed H.S. Nalwa Academic Press (2002).

[54] H Funakubo, N Nugaka, K Ishikawa, T Watanabe, *Jpn J Appl Phys.*, **38**, L199 (1999).

[55] N. Nukaga, K. Ishikawa, K. Shinozaki, N. Mizutani and H. Funakubo: *Key. Eng Mater.* **169-170**, 145 (1999).

[56] J.F. Roeder, B.C. Hendrix, F. Hintermeier, D.A. Desrochers, T.H. Baum, G. Bhandari, M. Chappius, P.C. Van Buskirk, C. Dehm, E. Fritsch, N. Nagel, H. Wendt, H. Cerva, W. Honlein, C. Mazure, *J. Eur. Ceram. Soc.*, **19**, 1463. (1999).

[57] C. Isobe, T. Ami, K. Hironaka, K. Watanabe, M. Sugiyama, N. Nagel, K. Katori, Y. Ikeda, C.D. Gutleben, M. Tanaka, H. Yaamoto, H. Yagi, *Integrated Ferroelectrics*, **14**, 95 (1997).

[58] H. Kodakura, Y. Okuhara, M. Mitsuya and H. Funakubo, *Chem. Vap. Deposition*, **6**, 225 (2000).

[59] A.C. Jones, N.L. Tobin, P.A. Marshall, R.J. Potter, P.R. Chalker, J.F. Bickley, H.O. Davies, L.M. Smith,G.W. Critchlow, *J. Mater. Chem.*, **14** (5), 887 (2004).

[60] R.J. Potter, P.A. Marshall, J.L. Roberts, A.C. Jones, P.R. Chalker, M. Ritala, M. Vehkamäki, P.A. Williams, H.O. Davies, N.L. Tobin, L.M. Smith. *MRS Fall 2003*, **784**.

[61] P.A. Williams, A.C. Jones, M.J. Crosbie, P.J. Wright,J.F. Bickley, A. Steiner, H.O. Davies, T.J. Leedham, G.W. Critchlow, *Chem. Vap. Depos.*, **7**, 205 (2001).

[62] P.R. Chalker, R.J. Potter, J.L. Roberts, A.C. Jones, L.M. Smith, M. Schumacher, *J. Crystal Growth*, **272**, (1-4), 778 (2004).

[63] M. Leskelä, M. Ritala, *J. Phys. IV* Fr. **9-Pr8**, 837 (1999).

Chapter 3 Experimental Methods

3.1 Aixtron AIX 200FE Liquid Injection MOCVD Reactor

3.1.1 Introduction

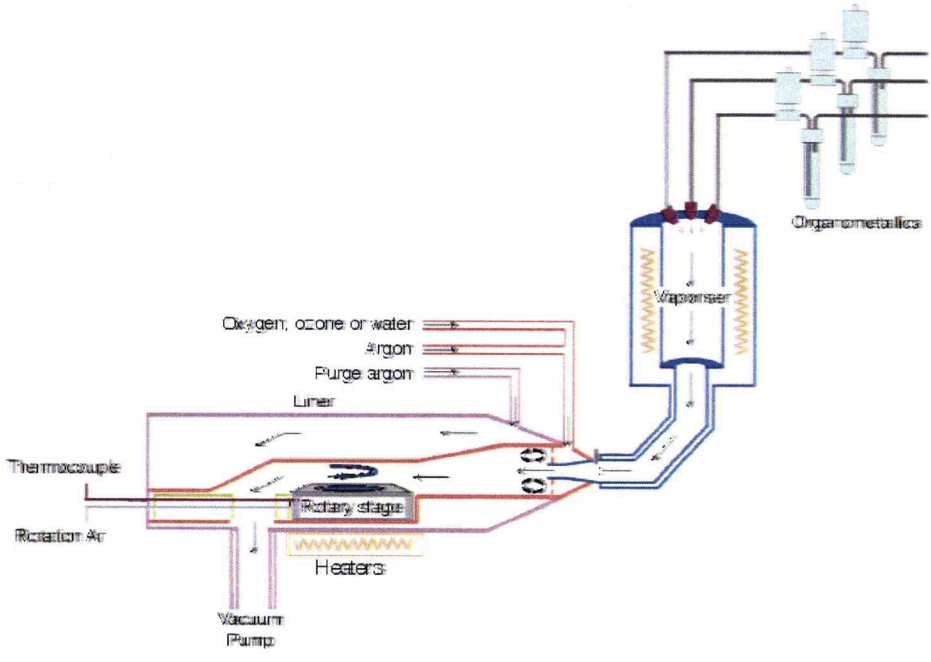

Figure 3.1: Aixtron AIX 200FE liquid injection MOCVD reactor

Figure 3.1 illustrates the Aixtron AIX 200FE liquid injection MOCVD reactor that was used for the thin film deposition experiments presented in this thesis (with assistance from Dr. R. Potter). The pulsed liquid

injection technique has recently been developed [1,2] and is based on the accurate metering and dispensing of liquid precursors into a hot wall reactor. This approach assists in making film deposition precisely controlled so that epitaxial oxides, magnetic hetero-structures and superlattices can be grown [3,4].

The system encompasses a Jipelec Trijet^{TM} injection solvent delivery system, which is connected to a horizontal flow CVD reactor. The reactor can take a 2 inch (50 mm) diameter wafer mounted on a rotary graphite susceptor stage.

Three individual liquid injectors are incorporated into the system, which feeds a single vertically mounted vaporiser, which in turn feeds a horizontal quartz reactor chamber. Figure 3.1 highlights the central elements and mechanism of the system's flow.

The reactor chamber lies within a cylindrical quartz liner vacuum vessel, which eases the process of cleaning and maintenance of the inner reactor chamber. The graphite stage is a simple and straightforward design allowing access (loading and unloading) to the reactor.

A carrier solvent (e.g. hexane) is used to dissolve or dilute precursors, which are stored in pressurised glass storage bottles connected by delivery tubes to the liquid injectors. The injectors are based upon an automotive component and are essentially miniature solenoid valves, which precisely meter, dispense and spray precursor into the vaporiser in an accurate controlled manner (Figure 3.2).

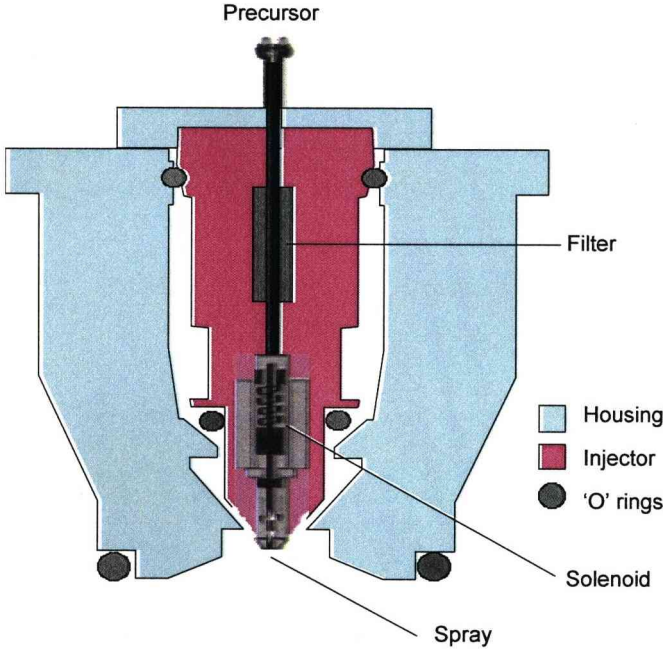

Figure 3.2: Representation of an injector

Ensuring that the storage bottles and lines stay at ambient temperature, enables usage of thermally sensitive materials without the risk of

decomposition. A stream of heated argon carrier gas is provided for each injector tip to ensure transportation of the precursor into and through the vaporiser.

The cylindrical vaporiser is approximately 40 mm across and 300 mm long, leading into a reduced diameter 90° swept bend, which feeds the reaction chamber. Banks of embedded cartridge heaters and thermocouples allow five independent zones in the vaporiser to be controlled up to a maximum temperature of 250°C. At the entrance to the reactor chamber, a Venturi type mixing system enables oxygen and argon to be mixed. The silicon wafer (2-inch, 50 mm diameter) to be coated, is placed on a horizontal gas driven graphite rotary stage supported in a graphite susceptor block. A bank of five electrically tuneable infrared lamps is used to heat the susceptor, which are controlled by a thermocouple embedded inside the susceptor.

A water-cooled filter, is situated downstream of the reactor chamber, where non-volatile materials are condensed and separated. The gas stream then enters the vacuum pump, which exhausts into an externally vented extraction duct. A five stage dry rotary vacuum pump is used,

which has inter-stage cooling and a nitrogen purge. A butterfly throttle valve situated at the pump inlet and regulates the reactor's pressure.

To ensure accurate deposition thickness, the substrate stage has a rotary drive, as there are variations in deposition rates along the axis of gas flow. This is due to precursor depletion as oxide grows on the wafer, susceptor and reactor walls. Mass flow controllers (MFCs) regulate all of the gas supplies to provide stable and repeatable reactor flow conditions. An MFC is also used to supply gas for pressurising the precursor bottles, which is set to continuously purge to exhaust via a pressure regulator.

A computer system controls the various injector conditions such as continuous opening or pulsing; pulse duration, frequency and count. The system also controls the reactor temperature, pressure and flow. In practice, it is normal to run the injectors in pulsed mode, due to the small volumes of precursor used.

The integrated control system is capable of executing deposition recipes, which have been previously written in a user-friendly code (CACE3) and stored in one of the two PCs. The equipment has extensive safety procedures and all control commands pass through an overriding safety

programmable logic controller (PLC), hardwired to prevent all foreseeable hazardous operations.

3.2 Film Thickness and Deposition Rate Measurement

It is vital to quantify the growth rate by measuring the film thickness. An estimation of the average film thickness is achieved by measuring the weight gain of a wafer after deposition. This is done using Equation (3.2), assuming constant film density and wafer area.

$$t_a = \frac{10^7 \times W_w}{\rho \times A_w} \qquad \textbf{(3.2)}$$

t_a = Average film thickness (nm)

W_w = Weight gain of wafer (g)

A_w = Area of silicon wafer (cm^2)

ρ = Film density ($gm.cm^3$)

The accuracy of weight-gain measurements is limited by numerous factors such as; weight, silicon wafer area and film composition and density. To overcome these limitations, each individual factor has been examined and where possible the error quantified.

3.2.1 Silicon Wafer Area

For this coating work, two-inch diameter silicon wafers containing two small orthogonal reference flats were used. The dimensional specification enclosed within each set of wafers presents the diameter tolerance as ± 0.25 mm. The maximum and minimum wafer areas, excluding the flats, are 2048 mm^2 and 2007 mm^2 respectively. From the above values, the film thickness error attributed to diameter variation is very small (~ ± 1%) and maybe ignored.

3.2.2 Film Composition and Density

As reactor conditions vary, fluctuations appear within the layer composition and density. Therefore, such sources of variation are not always possible to quantify accurately.

In parts of this thesis work, to calculate film thickness, assumed density values have been used and stated. This is logical if no density change is expected or little composition variation is shown by analysis. Total mass

deposition has been used as a further dependable method of displaying results when density and composition are unknown.

3.3 Electron Beam Analytical Methods

3.3.1 Introduction

The discovery of the light microscope in the late sixteenth century by the Dutch optician Zacharias Janssen offered the possibility to study the outer shape of small pieces of materials. However, it was not before the late nineteenth century that the microscope was used to study the polycrystalline microstructure of metals [5]. Although the majority of the elements of the periodic table were already known at this time, the internal structure of materials was unknown. Suitable experimental techniques were invented some decades later (X-ray diffraction and electron diffraction) that made structural analysis of the interior of materials possible. Shortly after, the electron microscope was developed, which soon offered a spatial resolution superior to optical microscopes.

In order to appreciate the way in which an electron microscope works and the meaning of the information it provides, it is important that the nature of the possible interactions between the electron beam and the other parts of the microscope (e.g. lenses or camera) and between the electrons and the specimen are understood. In its simplest form, the interaction between

the electron beam and a material can be seen in Figure 3.3. This interaction leads to numerous effects, many of which provide valuable analytical information.

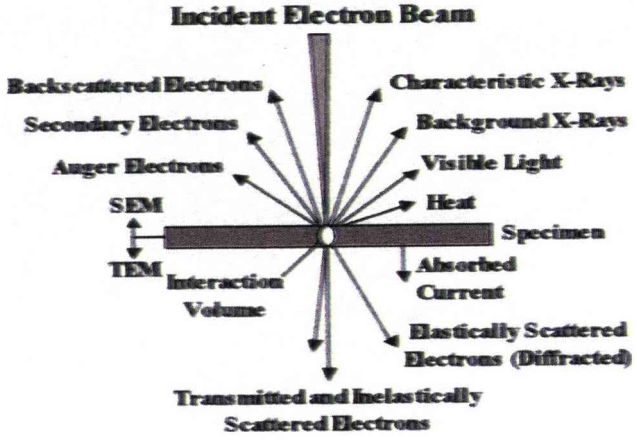

Figure 3.3: Electron beam interactions [6]

In almost all types of electron microscope, primary electrons enter the specimen and the same or different electrons leave it again to form the image. Consequently, it is vitally important to understand the interactions, which are possible between high-energy electrons and the atoms of the specimen. Without this understanding it is not possible to properly interpret the image, diffraction pattern or analytical spectrum, produced by the microscope. Hence, when an incident beam impinges on the sample, electrons maybe scattered in two different ways:

1. Elastic Scattering is a process, which although it might change the trajectory of the primary electrons, does not change their energies. This type of scattering results from Coulombic interactions (i.e. involving electrostatic charges) between the primary electron and both nucleus and all the surrounding electrons. This is known as Rutherford scattering and it gives rise to a strongly "forward peaked" distribution of scattered electrons. The change of trajectory yields the following effects:

    - Backscattering of electrons
    - Diffraction of Transmitted electrons: TEM diffraction patterns

2. Inelastic scattering is a general term, which refers to any process that causes the primary electron to lose a detectable amount of energy. In terms of the facilities usually available to electron microscopists, energy lost would need to be substantially more than 0.1 eV before it could be detected. Inelastic collisions result from different processes:

- Heating. Small amounts of energy transferred to the atomic lattice via thermal vibration (phonon excitation), appearing as a diffuse background in images.
- Cathodoluminescence, emission of visible light by fluorescence.
- Background X-rays, appearing as a continuum-wavelength noise, also known by the German name "Bremmstrahlung" meaning "breaking radiation".
- Characteristic X-rays at specific wavelengths.
- Secondary electrons of low energy ejected by the primary electron beam or backscattered electrons.
- Auger electrons ejected from an atom's outer shell of electrons.
- Plasmon scattering by characteristic energy transfer to valence or conduction electrons (in metals) causing collective electron oscillations.
- Characteristic electron energy loss due to individual atom ionisation, plasmon or phonon scattering. The technique of electron energy loss spectroscopy (EELS) uses the characteristic electron energy reduction to analyse composition.

The extent of beam penetration into the sample is dependent upon several factors; atomic number of the elements present and the kinetic energy of the incident beam. Figure 3.4 highlights the occurring electron interactions at different depths of penetration for a 20 KeV beam striking a sample of atomic number 28 (Si) [6].

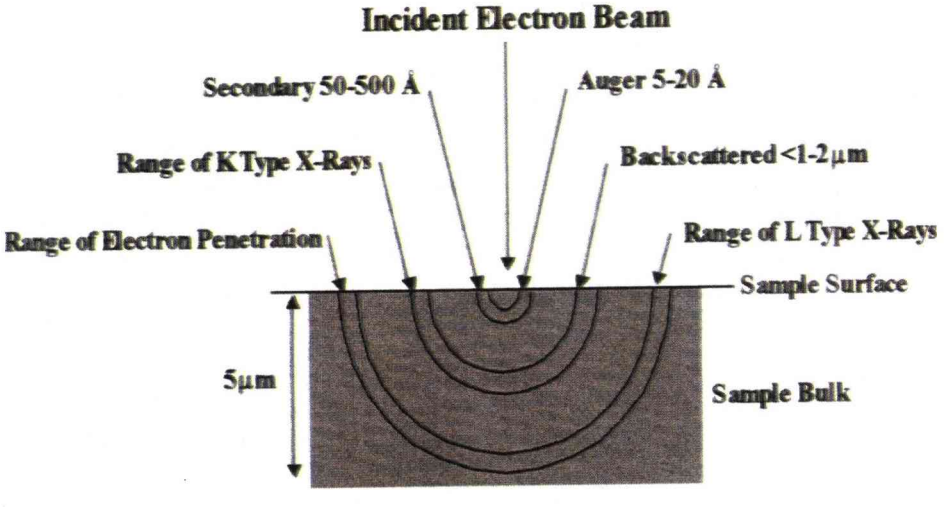

Figure 3.4: Beam penetration and effect depth in silicon (Z = 28) [6]

In the following sections, the main electron beam analytical techniques used in this work are described in more details.

3.3.2 Auger Electron Spectroscopy (AES)

Auger electron spectroscopy (AES) is a surface-specific analytical technique that utilises a high-energy electron beam as an excitation source. Atoms that are excited by the electron beam can relax via the emission of "Auger" electrons. AES measures the kinetic energies of the emitted Auger electrons, which are characteristic of elements present at the surface and "near-surface" of a sample (see Figure 3.5) [7].

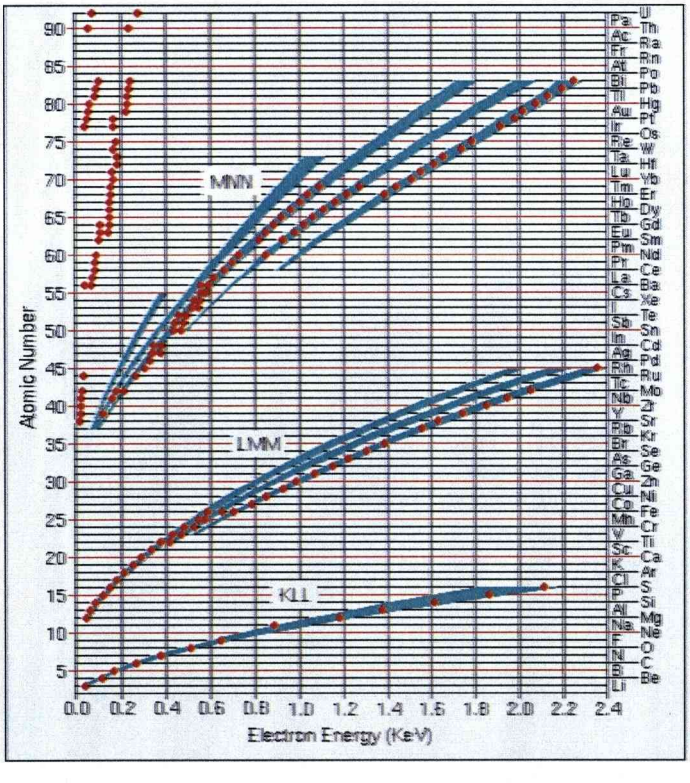

Figure 3.5: Auger peaks in the KLL, LMM, MNN transitions [7]

The benefits of Auger analysis are that the electron beam can be "rastered" over a large or small surface area. Or it can be directly focused on a small surface feature. This ability to focus the electron beam to diameters of 10 nm and less makes AES an extremely useful tool for elemental analysis of small surface features. The ability to raster the electron beam over an adjustable surface area provides control over the size of the analytical area. Moreover, rapid data acquisition (5-20 minutes), detection of elements heavier than He and high spatial resolution since a focused electron beam is used to excite the specimen.

The basic AES process starts with removal of an inner shell atomic electron to form a vacancy (See Figure 3.5). Several processes are capable of producing the vacancy, but bombardment with an electron beam is the most common. The inner-shell electron hole is filled by an outer shell electron. Energy must be simultaneously released. A third electron, the Auger electron, escapes carrying the excess (kinetic) energy in a radiation-less process. The process of an excited ion decaying into a doubly charged ion by ejection of an electron is called the Auger process. Alternatively, an X-ray photon can be emitted with the same energy. For low atomic number elements, the most probable transitions occur when a K-level electron is ejected by the primary beam, an L-level electron drops

into the vacancy, and another L-level electron is ejected. Higher atomic number elements have LMM and MNN transitions that are more probable than KLL.

Auger electrons are denoted by these energy transitions (Figure 3.6) therefore the Auger electron below is termed KL_1L_2; however other energy transitions, not necessarily from different shells may also occur e.g. KL_1L_1.

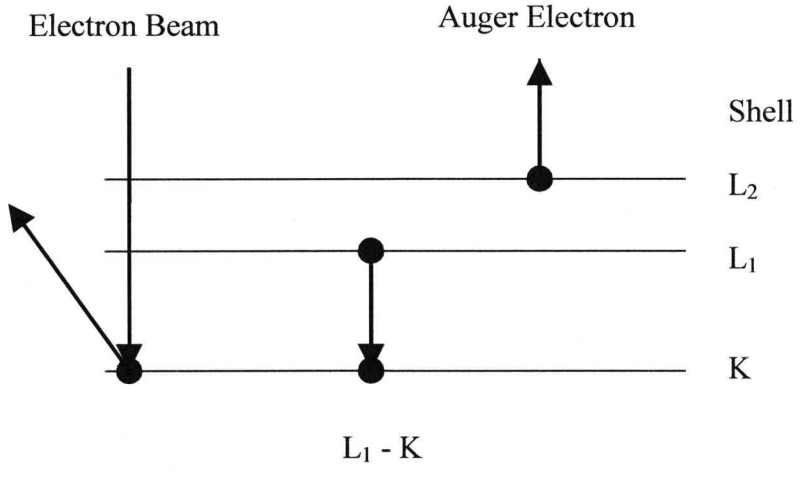

Figure 3.6: Generation of a KL_1L_2 Auger electron

Auger electrons in the energy range 20 – 2500 eV can only travel short distances in a solid and are unable to escape from the sample unless they are within approximately 5 – 20 Å of the surface making AES well suited

to measuring surfaces and very thin films. Surface sensitivity and easy scattering of Auger electrons also dictates that measurements have to be carried out in ultra high vacuum conditions (10^{-10} Torr). H and He cannot be detected by AES since these atoms only contain one filled electron shell, therefore the multi-shell energy transfer process, which generates Auger electrons cannot occur.

The AES analyses reported in this thesis were carried out using a Varian Scanning Auger Spectrometer (courtesy of Dr. Gary Critchlow of Loughborough University). Atomic compositions were measured from the bulk of the film, free from surface contamination by combining AES with sequential argon ion bombardment until consecutive data points gave comparable compositions. The compositional accuracy achievable by this procedure is ±0.5 at.% if calibration is carried out using appropriate powder samples of known composition.

3.3.3 Transmission Electron Microscopy (TEM)

In the late 1920's E. Ruska built the world's first transmission electron microscope (TEM). His pioneering work was acknowledged by the award of the Nobel Prize for Physics in 1986. By the 1950's, a major driving force for the usage of electron microscopes (EM) was the desire to overcome various limitations of the light microscope. It was evident that using electrons with wavelengths less than 0.1 nm, the resolution could be vastly better than light microscopes Moreover, the depth of field and depth of focus of electron microscopes has proved to be much better than those of a light microscope. For these reasons, two types of EMs were developed rapidly: scanning electron microscope (SEM) used to study surface morphology; and transmission electron microscope (TEM) enabling us to explore the internal structure of a thin specimen.

Originally, the mechanism of TEM was based on the physical principle that by using magnetic lenses, a charged particle could be focused. In doing so a "magnifier" similar to an optic microscope could be built. The discovery of wave properties of electrons drastically expanded our understanding of potential applications of a TEM. Moreover, TEM provides the ability to examine the structure, composition and properties

of specimens in sub-microscopic detail, a crucial technique for real-space imaging of defect structures in crystalline materials. The point-to-point image resolution currently available in TEM is better than 0.2 nm, comparable to the interatomic distances in solids. In addition, TEM has experienced revolutionary developments in both theory and electron optics, becoming one fundamental research tool for materials characterisation.

Compared to SEM, the TEM beam energy is much greater, typically between 50 – 300 keV, as the incident electrons require higher energy to pass through a thin sample. Elastic scattering of electrons in crystalline materials makes possible accurate structure analysis and characteristic diffraction patterns using electrons with different energy-losses. In doing so; scattered electrons generate TEM images, in either bright or dark field.

Bright field imaging exploits low angle electron scattering from the primary beam. Electrons are scattered by either a) high atomic number elements through a higher angle, which appears as a darker region in an image or b) low atomic number elements scattering through a small angle which appears as a lighter region in an image. Contrary to the bright field

image, dark field imaging examines electron scattering at higher angles, where low atomic number elements appear dark, and higher atomic number elements appear light. Whether bright or dark field is selected, TEM images are exclusively dependant on sample composition and structure.

It is vital that samples are examined in a condition as close to the natural state as is possible. This can be disadvantageous as specimen preparation often involves performing elaborate preparative steps to the sample ensuring it complies with the TEM criteria listed below:

1. Complete absence of water or similar volatile components.
2. Ability to remain unchanged under high vacuum conditions.
3. Stability when exposed to electron beam damage (physical and thermal stress).
4. Regions of both electron transparency and electron opacity.
5. Appropriate thickness for the TEM – electrons pass through ~ 5 microns, but beyond more than a few 100 nm, they lose energy and so cannot be imaged by the lenses. Consequently, the specimen thickness must be no greater than a few hundred nanometres.

As TEM involves spontaneous interactions between the electrons of the beam and atoms of the solid specimen, successful imaging is not always guaranteed. Each electron passing through the specimen has several possible outcomes. Most significantly are:

a) Electrons are undeflected – transmitted without interaction with any atom.
b) Electrons are deflected but lose no energy – elastically scattered.
c) Electrons lose a significant amount of energy and are deflected – inelastically scattered resulting in secondary electrons or X-rays may be excited.

If the above types of electrons are allowed to continue down the microscope, they will contribute to the image and all regions of the specimen looking identical. Contrast between areas of different thickness or composition would be indistinct. To overcome this problem and create contrast in the images, it is essential that scattered electrons are separated from unscattered electrons using the objective lens aperture.

A great advantage of the modern TEM is its versatile control systems. Not only can it explore the crystal structure using imaging and diffraction

techniques but also perform high-spatial resolution microanalysis using energy dispersive X-ray spectroscopy (EDS) and electron energy-loss spectroscopy (EELS). Thus determining chemical composition in a region smaller than a few nanometres is possible. TEM is therefore commonly regarded as high-resolution analytical electron microscopy. This is now becoming an indispensable technique for materials research.

In this work specimens were made, by bonding two samples together with epoxy resin. The coated sides of each sample facing one another (illustrated in Figure 3.7). The assembled parts were then sectioned across the plane by cutting with diamond cutting saw. The sample is then ground down by hand, while sample thickness was measured at regular intervals using Olympus BHM optical microscope. Once the thickness had been reduced, a 3 mm TEM copper support grid was glued to the specimen, for final thinning in a precision ion polisher (Gatan Ion Beam Mill).

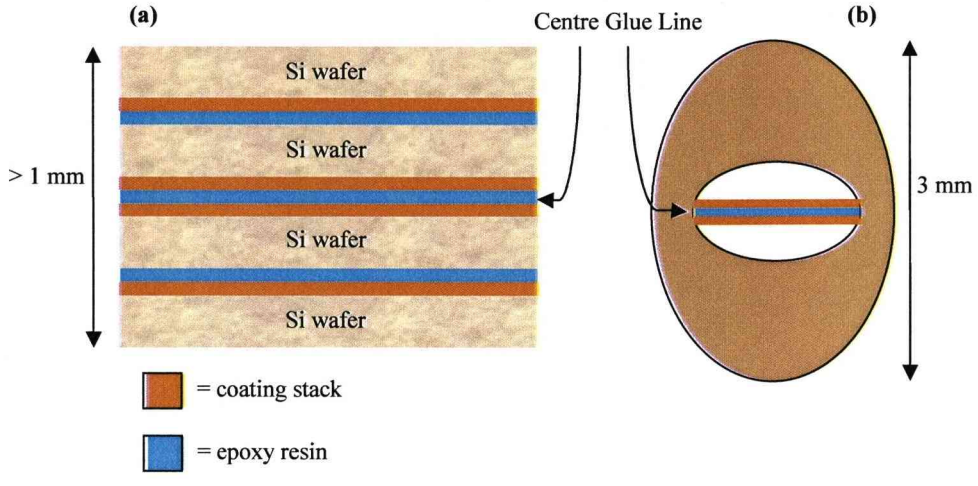

Figure 3.7 (a) shows a typical sandwich configuration for preparation of cross-section TEM specimens, deposited onto an n-type Si [100] wafer and **(b)** a diagram of the cross-section attached to a 3 mm copper TEM slot grid

The images in this thesis were produced using a JEOL 2000FX (at 200 keV) [8,9] as it provides lower resolution diffraction contrast imaging (with assistance from Dr. R. Murray). With a resolution of 2 nm and maximum magnification of x 800K, the JEOL 2000FX operates at 200 keV. The microscope was fitted with an Oxford X-Ray detector with an energy resolution of 135 eV at the Mn Kα energy. The EDAX Genesis^{TM} 4000 processing software, which controls the Oxford detector was used. When operated in scanning mode, elemental microanalysis can be carried out.

3.3.4 Scanning Transmission Electron Microscopy (STEM)

The VG HB 601 UX dedicated scanning transmission electron microscopy was used to produce STEM imaging and microanalysis (with assistance from Dr. P. Wang). The VG STEM is fitted with a cold field emission source - operating voltage of 100 kV. A current of 0.5 nA is delivered into a 0.8 nm probe when operating in microanalysis mode. The FEGSTEM has the capability of implementing high-resolution bright field and annular dark field imaging. It is fitted with an Oxford Link Pentafet, which has a windowless Si (Li) X-Ray energy dispersive detector operating at a solid collection angle of 0.2 sr. The Oxford Link Pentafet detector has an energy resolution of 135 eV at Mn Kα. To acquire and process X-ray data, an EDAX Gensis^{TM} 4000 software system was employed.

3.4 X-Ray Diffraction (XRD)

3.4.1 Introduction

X-rays are high-energy electromagnetic radiation [10]. They have energies ranging from about 200 eV to 1 MeV, which puts them between γ-rays and ultraviolet (UV) radiation in the electromagnetic spectrum (See Figure 3.8).

X-ray diffraction (XRD) characterisation has been used to identify crystalline and structural properties of thin film materials grown in this work. The technique is relatively sensitive and yields valuable atomic spacing and structural information regarding coatings both as-deposited and post thermal processing.

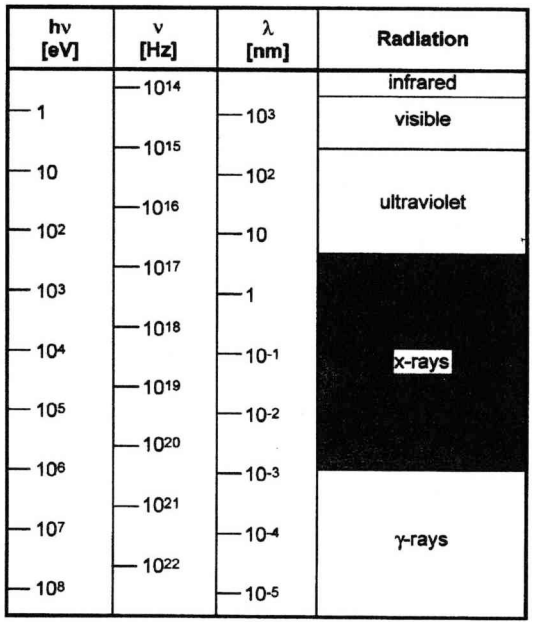

Figure 3.8: Part of the electromagnetic spectrum [10]

3.4.2 The Production of X-Rays

Commercial X-ray sources used for diffraction purposes are based on an X-ray tube consisting of two metal electrodes enclosed in a vacuum chamber, as shown in cross section in Figure 3.9. X-rays of a characteristic wavelength are generated by bombarding the target with high energy electrons. X-rays pass out at a shallow angle through a low absorption beryllium window (see Figure 3.9). The back of the target must be continuously cooled.

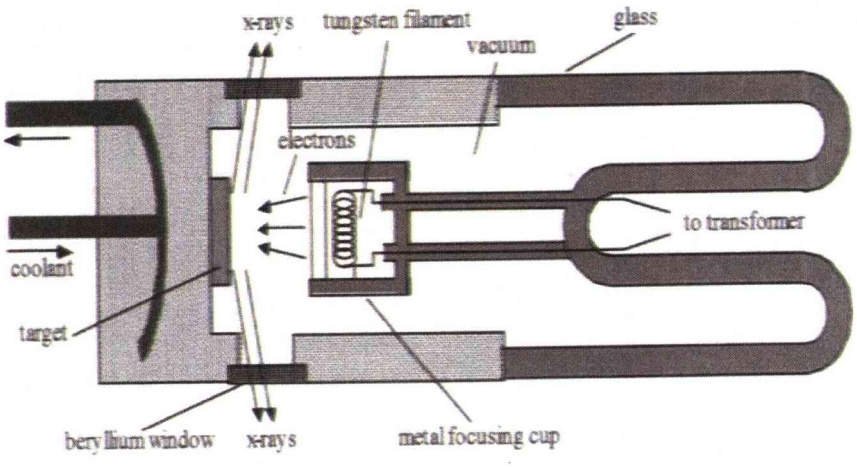

Figure 3.9: Schematic illustration of an X-ray source [6]

A typical X-ray spectrum illustrated in Figure 3.10, illustrates the variation in X-ray intensity as a function of wavelength for a Molybdenum source at range of accelerating voltages between 5 kV and 25 kV. Background radiation called "Bremmstrahlung" is due to electrons losing their energy in a series of collisions with the atoms that make up the target, as shown in Figure 3.10.

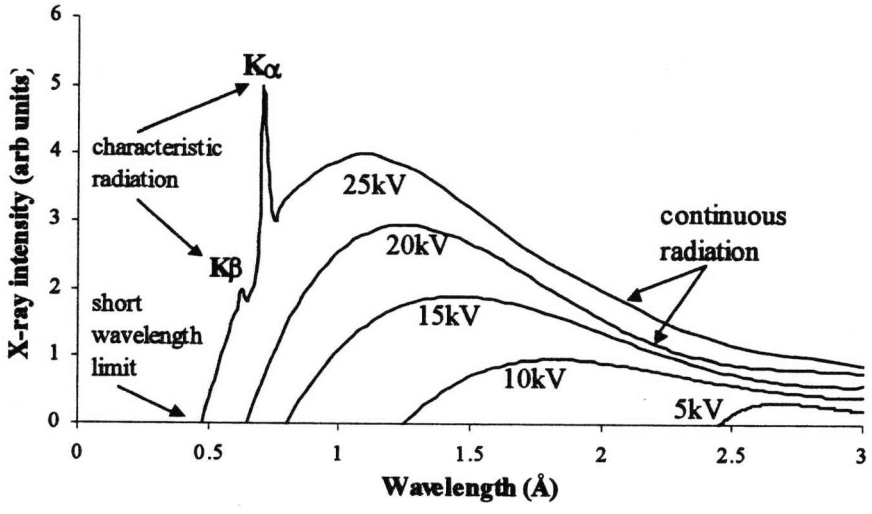

Figure 3.10: X-ray spectrum of molybdenum [6]

At 25 kV accelerating voltage, two high-intensity narrow characteristic radiation peaks appear, Kα and Kβ. Further resolution of the Kα peak reveals it to be a doublet of two closely related peaks $K\alpha_1$ and $K\alpha_2$. To explain the presence of Kα and Kβ peaks. If the incident electron has sufficient energy to eject an inner-shell electron, the atom will be left in an excited state with a hole in the electron shell, as illustrated in Figure 3.11. When this electron-hole is filled by an outer shell electron, an X-ray photon with energy equal to the difference in the electron energy levels is produced. The energy of the X-ray photon is characteristic of the target material. The sharp peaks, called characteristic lines, are superimposed on the continuous spectrum, as shown in Figure 3.10. It is these characteristic lines that are most useful in X-ray diffraction work.

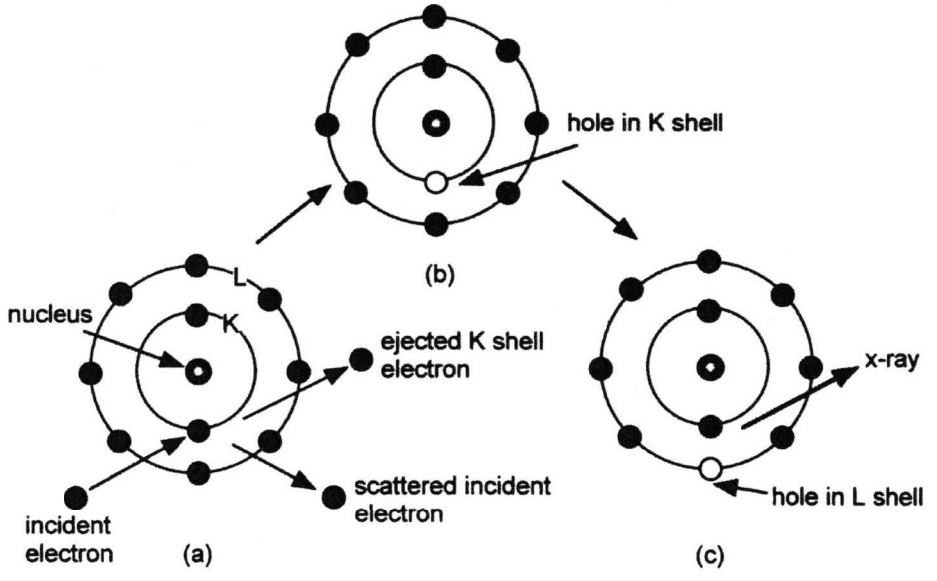

Figure 3.11: Illustration of the process of inner-shell ionisation and the subsequent emission of a characteristic X-ray

3.4.3 Filters

The process described earlier does not generate monochromatic X-rays as two specific wavelengths (Kα & Kβ) are produced. To ensure that only one wavelength is used for analysis, filtering is required. This can be achieved by placing a thin metal foil in the X-ray beam, which preferentially absorbs Kβ radiation. The chosen foil material is one atomic number less than the target material i.e. for the case of copper target (Z = 30), nickel is used (Z = 29).

The filter possesses a specific absorption characteristic or 'edge', whereby an incident X-ray removes a shell electron and so is absorbed. A higher shell electron then fills the vacancy produced and a fluorescent pulse is emitted. The behaviour of a nickel filter on a copper source is illustrated in Figure 3.12. For nickel the absorption edge occurs at a wavelength between Kα and Kβ.

The addition of a nickel filter reduces the intensity of the Kα peak somewhat, although the Kβ peak is virtually eliminated so the loss of signal strength is more than offset by the gain in resolution.

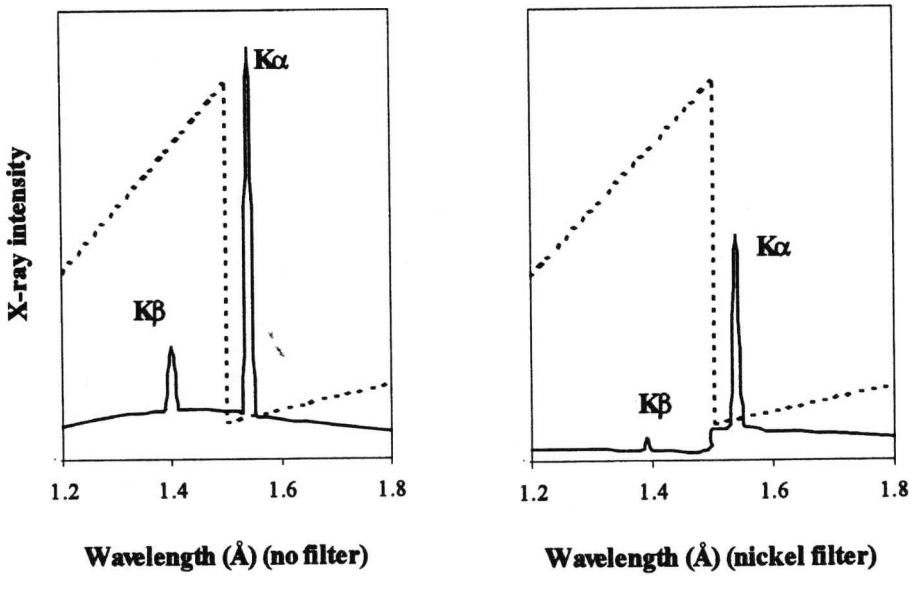

Figure 3.12: Effect of a nickel filter on a copper source [6]

3.4.4 Diffraction and Bragg's Law

An atom can scatter X-rays, and an atomic array can scatter waves constructively or destructively. If the scattered waves are in phase (coherent), they interfere in a constructive way and diffracted beams in specific directions are attained. These directions are governed by the wavelength (λ) of the incident radiation and the nature of the crystalline sample. Bragg's law, formulated by W.L. Bragg in 1913, relates the wavelength of the X-rays to the spacing of the atomic planes.

Two monochromatic parallel incident rays 1 and 2, are diffracted by two adjacent layers of atoms separated by a distance d (termed d-spacing) is shown in Figure 3.13. When the exiting rays (1' & 2') are in phase together, an increase in amplitude results. If however, the two rays are out of phase the resultant wave is of significantly lower amplitude. For exit rays 1' and 2' to be in phase and constructively interfere, the path length A-B-C must be equal to an integer multiple of the radiation wavelength used and the incident and exit angles (θ) must be equal.

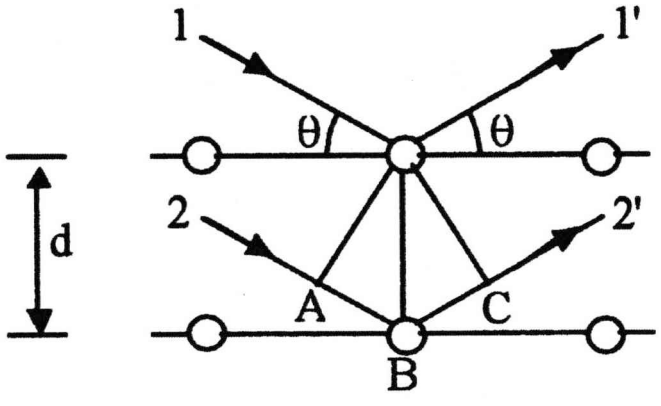

Figure 3.13: X-ray diffraction geometry

From the geometry of Figure 3.13 the extra distance travelled by ray 2-2 compared with 1-1 i.e. the distance A-B-C was first formulated by W.L. Bragg and is termed Bragg's Law (Equation 3.4.4).

$$N\lambda = 2d\sin\theta \qquad \textbf{(3.4.4)}$$

n = Integer

d = Atomic spacing (Å)

λ = Radiation wavelength (Å)

θ = Diffraction angle (°)

The technique requires the wavelength of electromagnetic radiation used to be smaller than the d-spacing, which is typically in the region of a few angstroms. Various metal sources are used to generate X-rays of different wavelengths, e.g. molybdenum λ = 0.709Å or copper λ = 1.5405Å to meet the requirements above. Hence, the nature of the material being studied determines the choice of wavelength. In this thesis, the diffraction studies were carried out using a copper source.

If a material is regularly ordered i.e. crystalline, it is possible to calculate the d-spacing by measuring the intensity and angle of the exit (diffracted) rays. In addition, comparing the data against standards assists with determining both structure and phase.

3.4.5 Rigaku Miniflex XRD Configuration

The plan layout of the Rigaku Miniflex X-ray diffractometer, used in this research is highlighted in Figure 3.14.

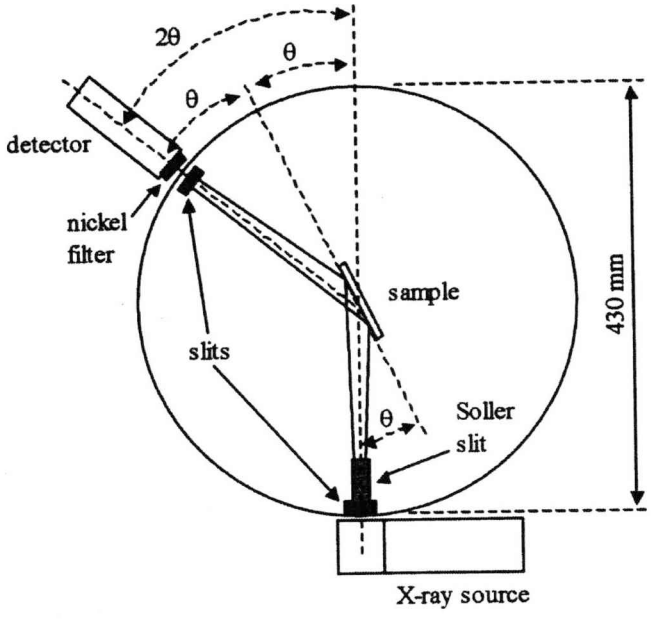

Figure 3.14: Rigaku Miniflex X-ray diffractometer

The system has a fixed X-ray source and two concentric horizontal rotary stages with the sample mounted vertically at the centre of the inner stage and able to rotate through an angle (θ). The outer rotary stage is electronically linked to the inner stage and moves the detector through

angles equivalent to 2θ such that the geometry defined by Bragg's law i.e. equal incident and exit angles, is maintained.

The X-ray beam exits the source and passes through a pair of vertical slits to narrow the beam and then through a Soller slit, an array of thin metal plates and gaps which confines the beam in the horizontal plane. At an incident angle θ, the X-rays strike the sample, which are diffracted through angle 180-2θ towards the detector. In front of which is a variable slit to reduce stray reflections and a nickel filter to remove Kβ radiation. The detector operates by counting for a set time the number of X-ray pulses above a predetermined threshold. The system is computer controlled and indexes the sample through a range of angular steps (θ) whilst simultaneously indexing the detector (2θ) and counting the diffracted X-ray pulses at each step. The file format consists of the pulse count versus the angular position of the detector (2θ).

3.5 Medium Energy Ion Scattering (MEIS)

3.5.1 Introduction

Medium energy ion scattering (MEIS) is a powerful technique in surface science for the determination of structural and compositional properties of surfaces and thin films. MEIS is a refinement of the more common technique of Rutherford backscattering spectrometry (RBS), but with enhanced depth and angle resolution. The Daresbury Laboratory of the Council for the Central Laboratory of the Research Councils (CCLRC) hosts the UK's national MEIS facility, which was developed jointly by Warwick and Salford Universities and officially opened in 1996.

Basically, a typical MEIS experiment uses a collimated beam of mono-energetic (typically 100 - 200 keV) light ions (usually H^+ or He^+) are focused onto a major crystallographic direction in the specimen. Energy and angle resolved detection of backscattered ions provides structural and compositional information [11]. The following physical principles are used:

- Mass - ions scattered from the surface of a material undergo energy loss by a "billiard ball" or Newtonian type collision with surface atoms where momentum and energy are conserved. The scattered ion energy relates directly to the mass of the scattering atom.
- Depth - ions scattered from below the surface lose energy inelastically at a rate proportional to the ion's path length in the target. This extra energy loss thus relates directly to the depth of the scattering atom. In favourable cases MEIS can achieve a depth resolution of one atomic layer.

Surface structure - when the ion beam is aligned with a crystallographic axis, the surface atoms shadow deeper atoms from the ion beam. This alignment can make the technique surface specific and, for a particular crystal, certain ingoing directions can allow the ion beam to illuminate only the top one, two, or three layers according to choice. Ions scattered from the second layer will have their outward paths blocked at certain angles by first layer atoms and so on. The variation in scattered ion intensity as a function of angle thus relates to the geometrical arrangement of surface atoms. A complete solution of surface structure

requires a comparison between experiment and simulation for several scattering geometries.

3.5.2 Ion-Atom Interactions

The interaction of an energetic ion with the atoms of a solid near its surface can be divided into four general categories. This division is based on the relationship between the distance of closest approach of the ion to the target nucleus, and the atomic and nuclear diameters of the ion and target. The distance of closest approach between atoms and nuclei is important in determining the nature of ion-atom interactions because if this distance is of order or less than the sum of atomic or nuclear radii, excitations can take place. Letting a_1, a_2, r_1, and r_2 represent the atomic and nuclear radii of the incident ion and target, respectively, and d the distance of closest approach, the following four processes will be considered (Figure 3.15):

- Elastic atomic collisions: are of primary importance at very low energies, typically less than 10 keV for ions such as Ar^+. The ion and atom barely penetrate before the ion is scattered and the

atom recoiled via a screened Coulomb interaction (Figure 3.15 (a)). In this case, the distance of closest approach is greater than the sum of the atomic radii of the ion and target [12].

- Inelastic atomic collisions with atomic excitation: these can occur for an energy characteristic of atomic energy levels. As the ion velocity increases, the probability for atomic excitation, including ionisation, increases. This occurs first for the outer shell electrons, and then for the inner shell electrons. The increasing probability of excitation leads to an increased emission of photons and electrons (Figure 3.15 (b)). These processes are most probable when the incident ion velocity is close to that of orbital electrons in specific shells. In general, protons must have energies of many keV to MeV. Although inelastic collisions have a high probability at such energies, their effect on the incident ion is limited to a slow loss in energy, and to negligible changes in direction.

- Elastic nuclear collisions: (Coulomb or Rutherford scattering) are important if the distance of closest approach between the ion and target nucleus is less than the sum of the atomic radii, but

still greater than the sum of the nuclear radii. In this case, the unscreened Coulomb potential accurately describes the interaction process. For small impact parameters, such as the head-on collision in (Figure 3.15 (c)), the incident ion undergoes a major change in direction while the nucleus of the target atom receives considerable recoil energy.

- Inelastic nuclear collisions with nuclear excitation: are least common since they require a distance of closest approach close to or smaller than the sum of the nuclear radii of ion and atom (Figure 3.15 (d)). Excitation of the target nucleus can be produced through the effects of either the Coulomb force or the nuclear force. Coulomb interactions are only possible when the incident ion energy exceeds that of the first excited state of the nucleus (usually 100 keV or greater). The energy lost by the ion, beyond the kinematic energy transfer, appears as excitation of the target nucleus and is eventually given up by photon emission. Interactions involving the nuclear force include excitation or the transfer of one or more nucleons from one nucleus to the other, followed by the emission of high-energy particles or photons, and often the creation of new isotopes.

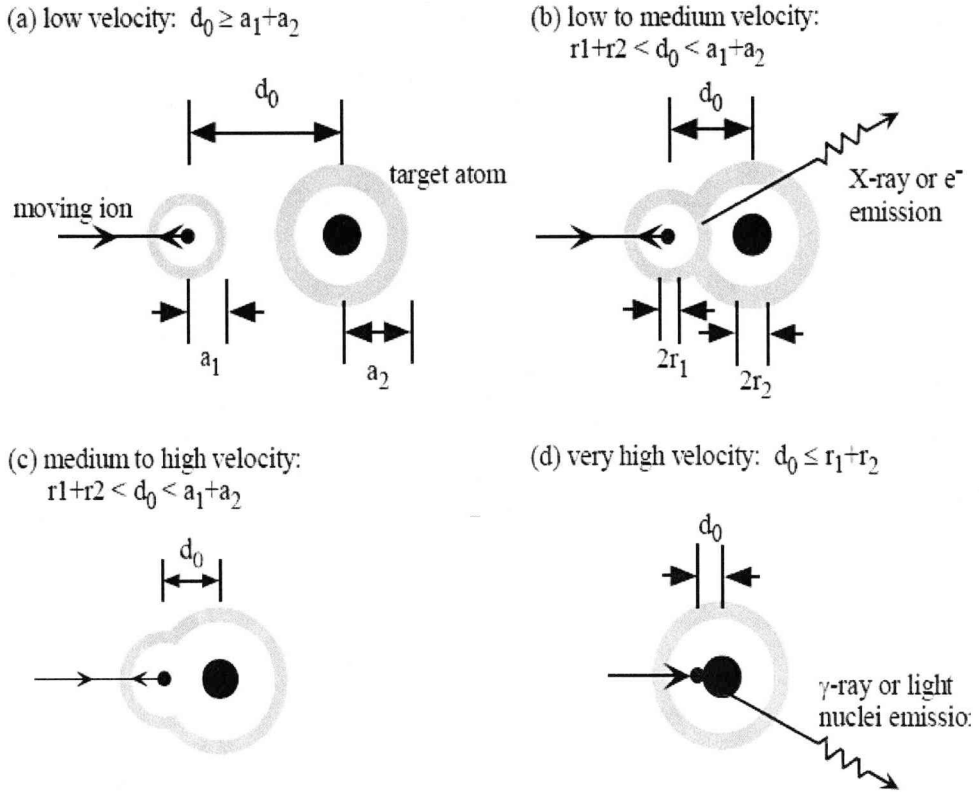

Figure 3.15: Schematic illustration of head-on ion-atom collisions illustrating four general types of interactions based on different velocities and distances of closest approach [12]

Several incident ion techniques exist utilising these various interaction regimes. Low-energy ion scattering (LEIS) typically uses <10 keV noble gas ions, and falls within the regime of elastic atomic collisions. High-energy ion scattering (HEIS) utilising ~MeV light ions is in the regime of elastic and inelastic nuclear collisions. MEIS, with projectile ions of

usually H^+ or He^+ in the energy range 40 – 400 keV, lies in a region extending over both types of intermediate energy reactions (Figure 3.15 (b and c)). Both of these types of interactions lead to key aspects of the MEIS technique. Elastic nuclear collisions lead to the mass specificity, while inelastic atomic collisions lead to the electronic stopping, which is used to provide depth sensitivity. Furthermore, these two interaction regimes can be described by a simple (classical and non-relativistic) treatment of the scattering process.

To justify the absence of inelastic nuclear collisions in MEIS, one needs to just consider the Coulomb barrier. This is the energy that an ion must have for the distance of closest approach to be such that the nuclei just touch. This energy represents a qualitative lower limit to the ion energy at which nuclear reactions readily take place. For example, the Coulomb barriers for P^+ or He^+ ions incident on Al are approximately 3 and 6 MeV, respectively. More specifically, the distance of closest approach for a 100 keV P^+ incident head-on to Al is ~180 fm (calculated by equating the centre of mass energy to the Coulomb energy at the turn-around point), while the Al nuclear diameter is ~4 fm.

The particle/wave duality must be taken into account in the study of particles of atomic dimensions by consideration of the de Broglie wavelength. At 10 eV or higher, a proton has a wavelength that is much less than atomic spacings and can easily penetrate between the atoms of a solid. For instance, a 100 keV proton has a de Broglie wavelength of order 10^{-3} Å. To be precise, as long as the scattering potentials do not vary over distances comparable to the wavelength of the scattered particle, then the classical formalism can be applied.

3.5.3 Description of the Facility

MEIS requires a rather sophisticated experimental setup, primarily due to the need for a very stable accelerator and complex detection device. In this section, the basic layout and equipment needed for the technique is briefly discussed. The facility consists of three sections: the high voltage enclosure (referred to as "the bun"), housing the ion source and accelerating lens; the transfer beam line; and the experimental end-station. The bun and beam-line are both computer controlled from a console in the end-station. A schematic of the equipment is shown in Figure 3.16.

A High Vacuum Engineering Europe (HVEE) hot cathode duo-plasmatron is used as an ion source, in which ions are formed when an arc is struck between a filament cathode (platinum) and a flat anode. Via mass flow controller, hydrogen or helium is fed into the region of the arc. The resulting plasma contains positive and negative ions as well as electrons. The discharge is shaped and confide by a magnetic field, and an aperture in the anode plate allows a small plasma bulge to emerge from the source. To extract ions from the bulging plasma boundary, a high field is used, which later forms a beam. Theoretically a beam can be produced from any elemental gas, although MEIS experiments generally only require either hydrogen or helium.

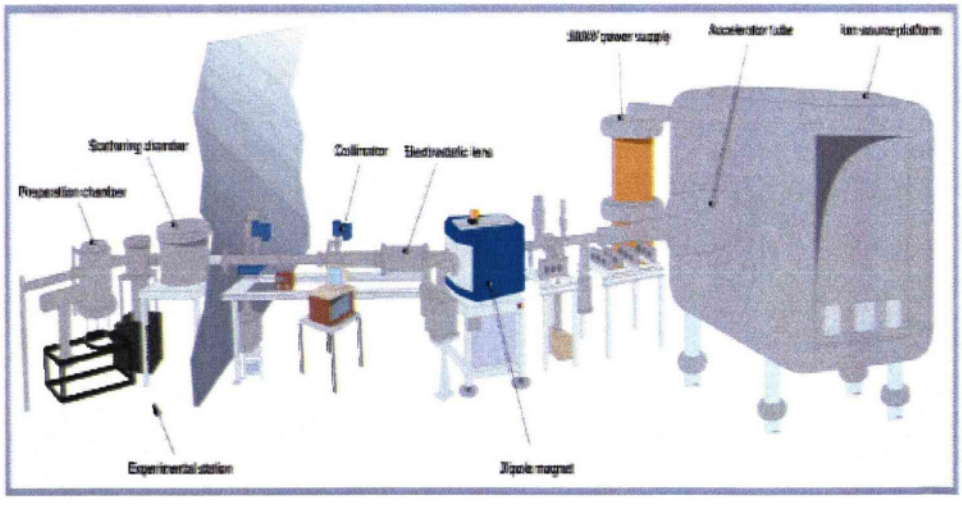

Figure 3.16: MEIS facility and major components [Daresbury website]

The beam line contains many beam defining, focusing and steering components. The beam defining components, movable slits and apertures are very rarely moved and are normally kept static at predetermined positions. The main focusing elements are often adjusted, particularly to defocus the beam during sample alignment. The scattering chamber is under ultra high vacuum (UHV, down to $8x10^{-11}$ mbar) and houses the sample goniometer, the toroidal electrostatic ion analyser (TEA), the beam-defining aperture, beam current monitor and all the associated feed-throughs. This chamber includes standard instrumentation such as; power supplies for electron beam heating, power supplies for the TEA and detector and a bias supply for the beam current monitor. A pneumatically operated gate valve connects the chamber to the beam line and a manually operated gate valve connects the chamber to the storage chamber through which samples are transferred. In normal operation this chamber remains under UHV and would only be vented in exceptional circumstances.

In 1998 [11], a beam monitor was installed in the scattering chamber to measure a fixed dosage of the beam. The monitor is subjected (around 300V) to suppress secondary electrons. It is constructed from an array of parallel vertical strands of 50 μm diameter gold-coated tungsten wire.

The reading from the monitor corresponds to 0.4 of the current transmitted to the sample allowing consistent sample exposure and a precise comparison of the results.

The ion source and beam-line deliver a beam of mono-energetic, low-divergence (<0.1°) ions into the scattering chamber and onto the sample. Scattered ions are analysed according to their energy and scattering angle by the TEA illustrated in Figure 3.17. It uses the field created by positive and negative voltages to bend the scattered ions through 90° and onto a detector. A field of ±6 kV across the analyser plates is required to bend 100 keV ions a trajectory though the TEA.

Analysed ions enter a detector assembly once they pass through the TEA. The first component of a detector is a pair of channel plates to amplify the tiny charge pulse generated by each ion (typical gain figure of 10^6). The electron charge cloud produced by the channel plates impinges on a two-dimensional area detector which determines the position of the charge cloud and hence the energy and angle of the scattered ion.

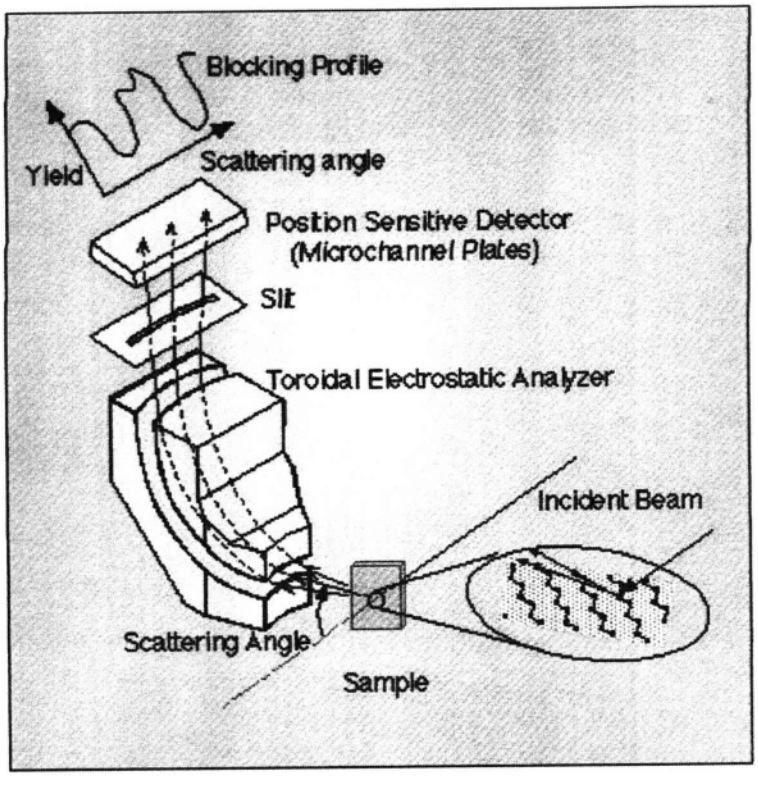

Figure 3.17: Toroidal electrostatic analyser [6]

Measurement is carried out in two stages, firstly alignment of the beam with a particular crystallographic direction and secondly, data acquisition. Sample alignment requires repeated scan and orientation changes of the sample to minimise the scattered ion count, effectively lining up the layers of underlying atoms. The three axes of the goniometer (see Figure 3.18) are scanned in turn to produce a plot of the integrated counts, illustrating when alignment is achieved.

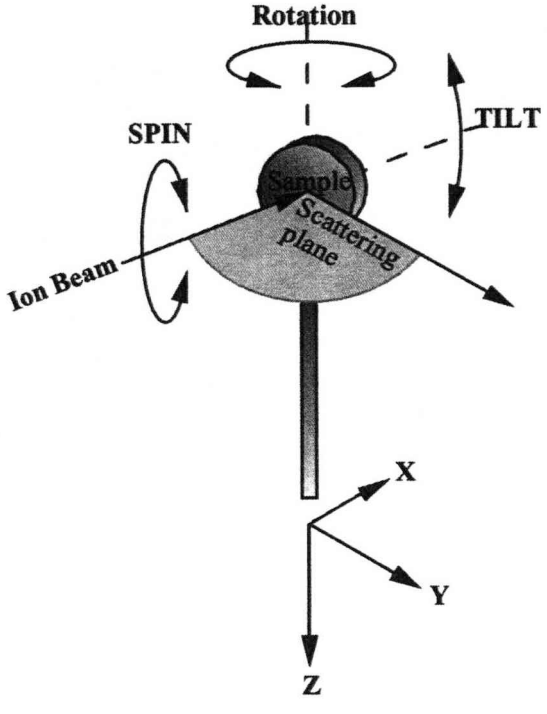

Figure 3.18: MEIS axes of alignment

3.5.4 MEIS Experimental Set-Up and Measurements

Using the following conditions as standard, MEIS measurements were taken (with assistance from Dr. T. Noakes):

Ion Source	200 keV He^+
Beam Current	< 200 nA
Beam Dimensions	Rectangular, 0.5 mm high, 1 mm wide
Substrate	Si [100]
Sample Charge Dose	2 μC
Energy per Pass	2% of pass energy
Ion Source Incidence Angle	Surface normal (100)
Scattered Ion Analysis Angle	Exit on surface [111]
TEA Angle	125°

Samples are firstly aligned to detect the Si substrate [100] crystal plane and surface normal then rotated to align the incident ion beam along the [111] crystal plane. This effectively shadows any Si atoms below the first one or two layers of the Si substrate contribution. The TEA was set at 125° to detect scattered ions in the range 55 keV to 190 keV. A strongly

blocked direction is present along the sample surface normal corresponding to the [100] crystal plane at a scattering angle of approximately 55° (depending on each sample alignment). Figure 3.19 shows a schematic of the incidence beam, surface scattering and bulk atom blocking. For clarity, surface layers of SiO_2 and deposited coating have not been shown.

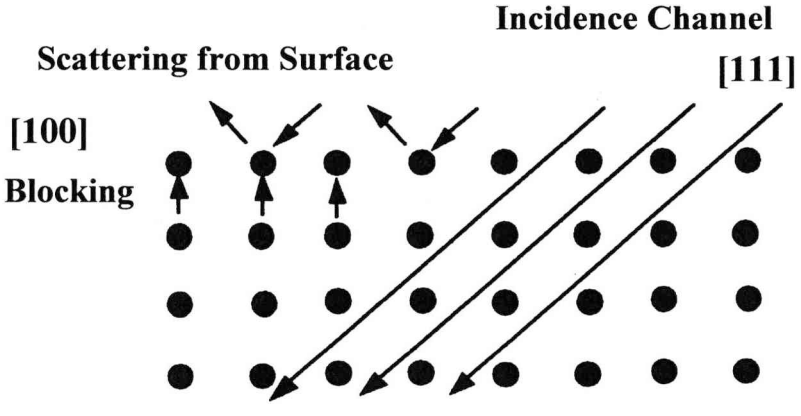

Figure 3.19: MEIS beam and sample alignment

The set-up shown in Figure 3.19 maximises the system sensitivity to thin surface layers present on the substrate and minimises scattering from the crystalline silicon. The measurement process consists of multiple scans stepping down the TEA pass energy in stages to initially detect high

energy and surface scattering followed by lower energy and deeper scattering. Multiple windows are obtained which are then "tiled" together to form the composite image. The numerical data gathered from the ion count versus energy projection is then used as a basis to calculate the composition and film thickness of the surface layers. To carry out this calculation the data is imported into a proprietary software package; SIMNRA 5.0 developed by the Max Planck Institute for Plasma Physics. The program allows the MEIS energy and angle response of multiple composition and thickness layers to be generated and tested against experimental data until a good fit is achieved.

3.6 References

[1] J.P. Senateur, C. Dubourdieu, F. Weiss, M. Rosina and A. Abrutis, *Adv. Mater. Opt. Electron.* **10**, 155-161 (2000).

[2] J.P. Senateur, R. Madar, F. Weiss, O. Thomas and A. Abrutis, French patent FR 2707671 (1993), European patent EP 730671 (1994), US Patent US 945162 (1999).

[3] C. Dubordieu, M. Rosina, M. Audier, F. Weiss, J.P. Senateur, E. Dooryhee and J.L. Hodeau, *Thin Solid Films*, **400**, 81-84 (2001).

[4] F. Weiss, J.P. Senateur, J. Lindner, V. Galindo, C. Dubordieu and A. Abrutis, *J. Phys. IV* **9**(1), Pr8-283 (1999).

[5] T.G. Rochow and P.A. Tucker, "*Introduction to Microscopy by Means of Light, Electrons, X Rays, or Acoustics*" (2nd Edition), Plenum Publishing (1994).

[6] P.A. Marshall, *Liquid Injection MOCVD of Hafnium Oxide, Silicate and Aluminate High-K Dielectrics*, Published PhD, The University of Liverpool (2005).

[7] K.D. Childs, B.A. Carlson, L.A. Vanier, J.F. Moulder, D.F. Paul, W.F. Stickle and D.G. Watson in C.L. Hedberg, Ed., "*Handbook of Auger Electron Spectroscopy*", Physical Electronics, Eden Prairie, MN (1995)

[8] D.B. Williams and B. Carter, "*Transmission Electron Microscopy*" Vol.1, **180**, Plenum Publishing (1996).

[9] P.J Goodhew, and J. Humphreys, "*Electron Microscopy and Analysis*", Taylor and Francis (1998).

[10] C. Suryanarayana and M.G. Norton, "*X-Ray Diffraction A Practical Approach*", Plenum Publishing (1998).

[11] P. Bailey, T.C.Q. Noakes, C.J. Baddeley, G. van der Lanan, D. Brown, P.D. Quinn and D.P. Woodruff, *"Aspects of layer-by-layer composition analysis using MEIS"*, Current Applied Physics 3, **89-92** (2003).

[12] B.W. Busch, *Metal and Alloy Surface Structure Studies Using Medium-Energy Ion Scattering*, Published PhD, The State University of New Jersey (2000).

Chapter 4 MOCVD of Strontium Tantalate and Bismuth Oxide

4.1 Introduction

Applications ranging from: microwave and rf components [1,2]; to ferroelectric capacitors in Non-Volatile Ferroelectric (NV-FeRAM); and Dynamic Random Access Memory (DRAM) [3], all have one feature in common. They all use thin-film ferroelectrics. For these types of applications, the following factors are required from the ferroelectric film: large area film uniformity, high growth throughput, fatigue-free properties, conformal step coverage and precise composition control.

Several of the multicomponent metal oxides containing strontium and tantalum have a variety of important technological applications, one of which is strontium bismuth tantalate, $SrBi_2Ta_2O_9$ (SBT). SBT is regarded as a promising material for use in non-volatile ferroelectric memory applications [4,5,6]. It is a layer type bismuth compound consisting of Bi_2O_2 layers encompassed by cubic perovskite-like $SrTa_2O_7$ layers (two perovskite units thick) in its crystal structure [7]. These perovskite

structures are known for their excellent fatigue-free nature as even after an intense 10^{12} switching cycle, the remanent polarisation is not reduced and has a low coercive switching threshold [4].

For industrial manufacturing applications requiring the use of thin-film ferroelectrics, chemical vapour deposition (CVD) is well established for its importance technologically [8]. This is the case for the applications of SBT, which require high compositional and thickness uniform deposition over a large area with high step coverage. Although CVD is recognised for its technological significance, there is an insufficient research base regarding CVD-SBT film investigations [5]. This is largely due to the shortage of high quality precursor sources for strontium. Apart from the study in this thesis, there are only few groups [8,9,10], which have been investigating SBT film deposition by using the related method; metal organic chemical vapour deposition (MOCVD). As the demand for higher memory device densities in consumer electronic products increases, the deposition of ferroelectric thin-films by, MOCVD, has become essential [8,11]. The MOCVD process is distinguished by the use of metal-organic CVD precursors which are either evaporated or dissolved into a solvent to facilitate vapour transport. This latter process is termed 'liquid injection' MOCVD.

Several advantages of liquid injection MOCVD are obvious when compared to other commercially available ferroelectric deposition techniques, namely: a) excellent conformal deposition is achieved, which is necessary for an increasing level of integration into devices; b) MOCVD has reduced defect density; and c) a higher throughput can be obtained while maintaining precise stoichiometry and uniformity control [12,13].

To realise the benefits of precise stoichiometry and uniformity control, the precursors used have to meet some stringent requirements, such as thermal stability and volatility. Consequently these severe restrictions have slowed the development of MOCVD for SBT growth in particular. At the outset of this research, the lack of suitable metal-organic precursors was a notable factor. Conventional precursors that had been investigated such as $Sr(thd)_2$ (thd=2,2,6,6-tetramethylheptane-3,5-dionate), $Bi(C_6H_5)_3$, ($BiMe_3$), $Bi(O^tC_5H_{11})_3$, $Ta(OEt)_5$ and $Ta(OPr^i)_4(thd)$ [14,15], exhibit very different decomposition characteristics and physical properties. The variation in decomposition characteristics leads to inconsistency and results in several setbacks, including reduced bismuth incorporation efficiency, poor composition control and unacceptable film uniformity.

In order to address this mismatch and overcome these significant deposition problems, the strontium tantalate heterometal alkoxide precursors, $Sr\{Ta(OEt)_6\}_2$ and $Sr\{Ta(OPr^i)_6\}_2$ [5,15] have been used for the MOCVD of SBT. These "single source" precursors contain two (or more) of the elements required in the oxide film in a single stoichiometric compound. This 'single source' method is potentially advantageous as the nominal metal : metal ratio in the precursor should meet the stoichiometric requirements of the oxide film deposited.

However, there are also disadvantages of using such precursors. $Sr\{Ta(OEt)_6\}_2$, for example, can fragment into components of significantly different volatilities. The $(Sr(OR)_2)$ and $(Ta(OR)_5)$ fragments arise from detachment of the Sr and Ta molecular components in the gas phase and lead to a surplus of the more volatile Ta component in the deposited oxide [16] as bismuth is lost to the reactor walls. Another disadvantage is that the $Sr\{Ta(OR)_6\}_2$ precursors consist of an unsaturated Sr centre, making them susceptible to chemical attack by moisture, which reduces their efficiency (deposition rate), particularly in solution-based liquid injection MOCVD.

As a method of mitigating the aforementioned problem and improving the MOCVD of SBT, donor-functionalised alkoxide ligands, such as dimethylaminoethoxide (dmae=$OCH_2CH_2NMe_2$) and bis(dimethylamino)propanolate (bis-dmap=$OCH(CH_2NMe_2)CH_2NMe_2$) have been inserted into the heterometal alkoxide. This chemical insertion is performed to increase the ligand co-ordination surrounding the central Sr atom [17]. As a result; gas-phase dissociation is inhibited, decreasing the air-sensitivity and rendering the complexes more thermally stable.

A range of complexes of the type $(Sr\{Ta(OR)_5(L)\})_2$ (where R= Et, Pr^i and L= dmae, bis-dmap) were developed. Of these $Sr\{Ta(OEt)_5(dmae)\}_2$ proved to be the most effective precursor in terms of volatility and thermal stability. Moreover, this precursor has previously been utilised in atmospheric pressure liquid injection MOCVD of strontium tantalate [9]. The Sr:Ta ratio was discovered to be a function of substrate temperature and O_2 flow. Additionally, under optimum growth conditions, the Sr:Ta ratio was observed to be close to 0.5, which coincides with the $SrBi_2Ta_2O_9$ stoichiometry. Furthermore, investigations completed elsewhere, have investigated the deposition of SBT films, grown by liquid injected MOCVD with the $Sr\{Ta(OEt)_5(dmae)\}_2$ precursor. The

results from those studies illustrated good ferroelectric properties and improved stoichiometry control [18].

Alternative functional groups or 'ligands', which have been used as effective stabilisers of strontium tantalate heterometal alkoxide precursors are the donor functionalised alcohols. Examples of these include methoxyethanol (mee, $OCHCH_2OMe$), however, studies carried out elsewhere have verified that, in contrast to ($Sr\{Ta(OPr^i)_6\}_2$), the Sr:Ta mole ratio remains invariable during the distillation of $Sr\{Ta(OEt)_5(mee)\}_2$ [16].

As mentioned earlier, the state of technology for electronic device integration has advanced faster than the fundamental studies of material properties required to underpin these developments. Current semiconductor processing requires fabrication temperatures to be as low as possible, to optimise the properties of the ferroelectric/semiconductor device structures and minimise inter-diffusion or degradation.

For the deposition of SBT, it is necessary to complement the "single source" strontium tantalate precursors, with appropriate co-precursor Bi-alkoxides. The ($Bi(OR)_3$) (R = alkys) are likely to be suitable for this

purpose as they exhibit similar decomposition behaviour. The majority of Bi-alkoxide compounds are involatile polymers, however, the polymerisation can be inhibited using the sterically hindering 'mmp' ($OCMe_2CH_2OMe$) ligand, which has enabled the formation of the volatile monomeric complex, $Bi(mmp)_3$.

This chapter investigates the liquid injection MOCVD of the component precursors for SBT namely: the single source precursor $Sr\{Ta(OEt)_5(dmae)\}_2$ and the co-precursor $Bi(mmp)_3$. In addition, the effect of post-deposition annealing of the resulting strontium tantalate and bismuth oxide thin films has been investigated. These post-deposition annealing studies provide a baseline for the SBT annealing studies presented in Chapters 5 and 6. The Aixtron TriJet™ liquid delivery system was used for the deposition studies and characterisation of the strontium tantalate and bismuth oxide thin films has been made using the AES and XRD techniques described earlier in Chapter 3.

4.2 Experimental

Oxide films were deposited on the horizontal Aixtron AIX reactor (model 200FE) by liquid injection MOCVD. The reactor is fitted with the Trijet^{TM} injector system (details of which are located in Chapter 3.1). Strontium tantalate and bismuth oxide films were deposited on Si(100) substrates as received and without further pretreatment. Consequently, the thin films were deposited on a native SiO_2 of approximately 1 nm thickness. The precursors were dissolved, using 0.1 M precursor solutions in n-heptane. During deposition, substrate rotation (at approximately 60 rpm) was used to improve film uniformity. The strontium tantalate and bismuth oxide films were deposited over a range of substrate temperatures between 300 – 600°C at a reactor pressure of 5 mbar. The injector conditions for strontium tantalate and bismuth oxide precursors are presented in Table 4.1.

Parameter	strontium tantalate	bismuth oxide
Precursor injection rate	20.9 – 21.6 µl/h	18 – 18.7 µl/h
Injector frequency (pulses)	1 Hz (900)	1 Hz (600)
Evaporator temperature	200°C	150°C
Substrate temperature	300 – 600°C	300 – 600°C
Reactor pressure	5 mbar	5 mbar
Precursor solution concentration	0.1M in n-heptane	0.1M in n-heptane
Argon carrier gas flow rate (STP)	200 $cm^3 min^{-1}$	200 $cm^3 min^{-1}$
Oxygen flow rate (STP)	100 $cm^3 min^{-1}$	100 $cm^3 min^{-1}$
Substrates	Si (100)	Si (100)
Oxidant	Oxygen	Oxygen

Table 4.1: Reactor growth conditions (Aixtron AIX 200FE)

Details of the analytical techniques used in this chapter, for example; AES, XRD and MEIS are discussed in Chapter 3.

4.3 Results and Discussion

4.3.1 Growth Rates and AES Analysis of Strontium Tantalate

The single source precursor $Sr\{Ta(OEt)_5(dmae)\}_2$ was successfully used for the deposition of strontium tantalate (ST) films over substrate temperatures ranging from 300 – 600°C. Figure 4.1 illustrates the variation in oxide growth rate with substrate temperature. It is apparent that the growth rate of the ST films is found to be reliant on growth temperature. This is evident from the graph, as the growth rate above 300°C, increases with substrate temperature, which is consistent with an Arrhenius growth characteristic i.e. that the growth rate is governed by an activation energy. The growth rate then trails off above 550°C as decomposition on the reactor walls getters the gas-phase precursor and prevents further increase in the growth rate.

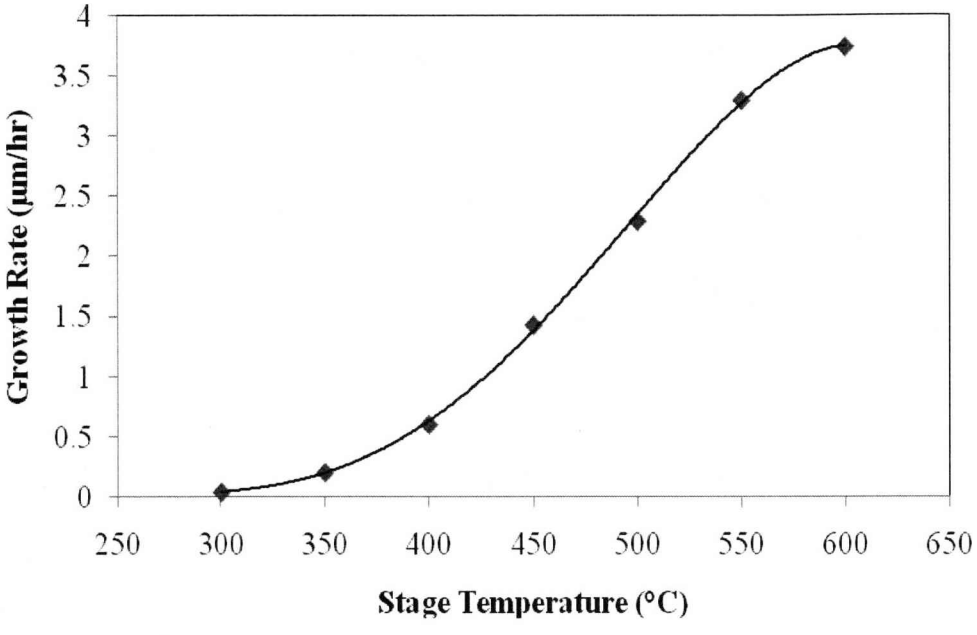

Figure 4.1: Strontium tantalate growth curve using $Sr\{Ta(OEt)_5(dmae)\}_2$

As discussed in Chapter 3, the errors in estimating the growth rate (figure 4.1) arise principally from the measurements of weight gain due to the film deposition. In the context of the data shown here the errors are estimated to be less than ± 10%. A significant factor in the estimation of growth rate is the density used to calculate the film thickness, which will vary according to whether the film is either a characteristic crystalline phase or an amorphous one.

The composition of the strontium tantalate films is found to be heavily dependent on growth temperature. This is illustrated in Table 4.2 and

Figure 4.2. As observed, the film composition is found to be slightly Ta-rich (Sr:Ta ~0.8 at 300°C) at the lowest growth temperature (300°C). Between 350 – 400°C the Sr:Ta ratio in the films reaches a maximum close to unity, followed by a linear decline of the Sr fraction with substrate temperature. The optimum growth temperature is found around 510°C. This is where the Sr:Ta ratio in the film is 0.5 - stoichiometry close to $SrTa_2O_6$ (for the SBT composition).

Moreover, the mass deposition rates have been examined closely in order to further understand the temperature dependence behaviour of the precursors. The temperature dependence of the Ta and oxygen (O) mass deposition rates follows similar trends to the overall strontium tantalate growth curve. In addition, the Sr mass deposition rate also follows a similar trend up to ~450°C; however, the Sr incorporation falls dramatically between 550 – 600°C. The mechanism accounting for the absence of strontium at higher temperatures can only be speculative. Preferential removal of strontium from the growth surface would require the formation of a volatile by-product from the $Sr\{Ta(OEt)_5(dmae)\}_2$ decomposition. Without the use of in situ spectroscopic techniques the formation of this by-product cannot be unequivocal. Analysis of the AES measurements, showed a correlation between the carbon (C) mass

deposition rate and the Sr-mass deposition trend. This suggests that the two reaction paths for the deposition of Sr and C are correlated. Residual carbon is derived from the incomplete decomposition of the metal-organic precursor and is consistent with other MOCVD studies using metal alkoxide precursors [19]. From these studies, it was found that the carbon contamination tends to decrease with increasing deposition temperature and increase at low oxygen gas phase concentrations. These trends can be readily ascribed to incomplete removal of the alkoxide ligand at low substrate temperatures, or the lack of available oxygen at low oxygen flow rate. The precise mechanism of C incorporation in the film is unknown and is beyond the scope of this study. Although no obvious increase in deposition was seen on the reactor walls or upstream of the substrate, the dramatic fall in Sr incorporation, at substrate temperatures above 550°C suggests that thermal decomposition of the precursor has led to pre-deposition (of possibly $SrCO_3$) and partial separation of the Sr and Ta components.

Substrate Temperature (°C)	Composition (at%)				Sr:Ta Ratio
	Strontium	Tantalate	Oxygen	Carbon	
300	10.6	13.17	71.53	4.73	0.81
350	11.7	10.6	72.3	5.37	1.10
400	12.4	11.55	72.5	3.5	1.07
450	10.45	13.9	73.05	2.6	0.75
500	9.27	16.63	67.9	6.23	0.56
550	6.87	19.83	72.6	0.73	0.35
600	0.6	25.47	71.87	2.07	0.02

Table 4.2: AES results of strontium tantalate

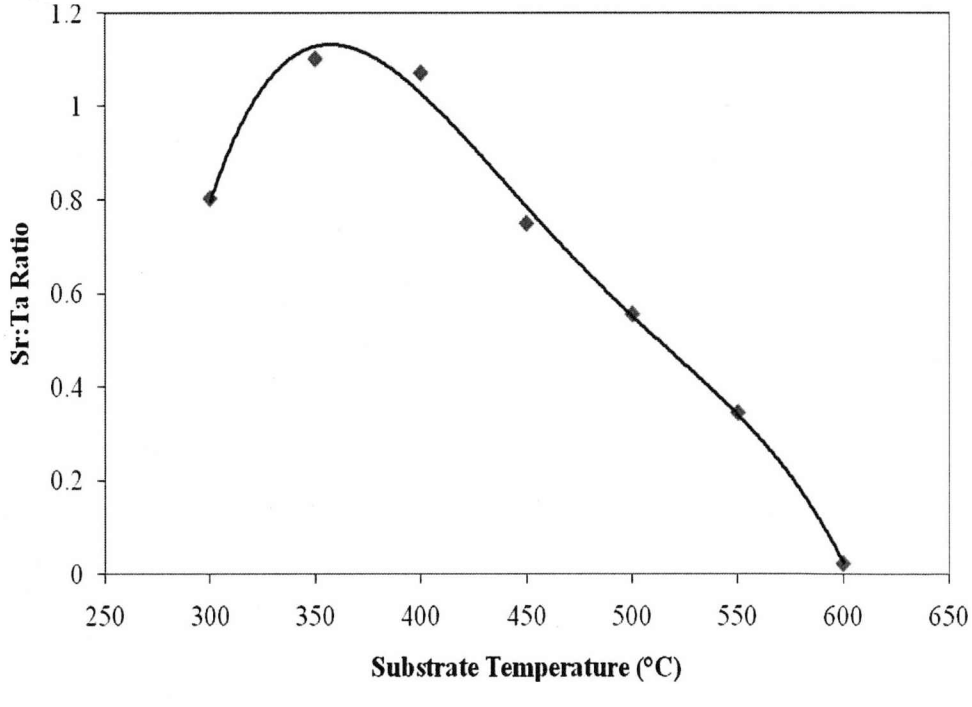

Figure 4.2: Sr:Ta ratio based on AES results

4.3.2 XRD Studies of Strontium Tantalate

The as-deposited ST films across the temperature range 300 – 600°C exhibit an amorphous-like microstructure and demonstrate no crystalline diffraction features in the corresponding X-ray diffraction (XRD) patterns. In order to fully comprehend the high temperature characteristics of the ST films, annealing studies were carried out, coupled with further analysis by XRD.

The annealing studies were focused on the films grown at ~500°C as these exhibited the Sr:Ta ratio close to 0.5 (shown by the AES results). It was evident after investigations at numerous annealing temperatures and times, that films undergo crystallisation at around 650°C (for 15 minutes) in air. The films formed an orthorhombic crystalline phase as illustrated in Figure 4.3. The diffraction pattern of the annealed film closely resembles that of a $Sr_{2.83}Ta_5O_{15}$ (Sr:Ta ratio of 0.57) phase identified by Siegrist et al. [20] (P4/MBM, ICSD; ID = 24663).

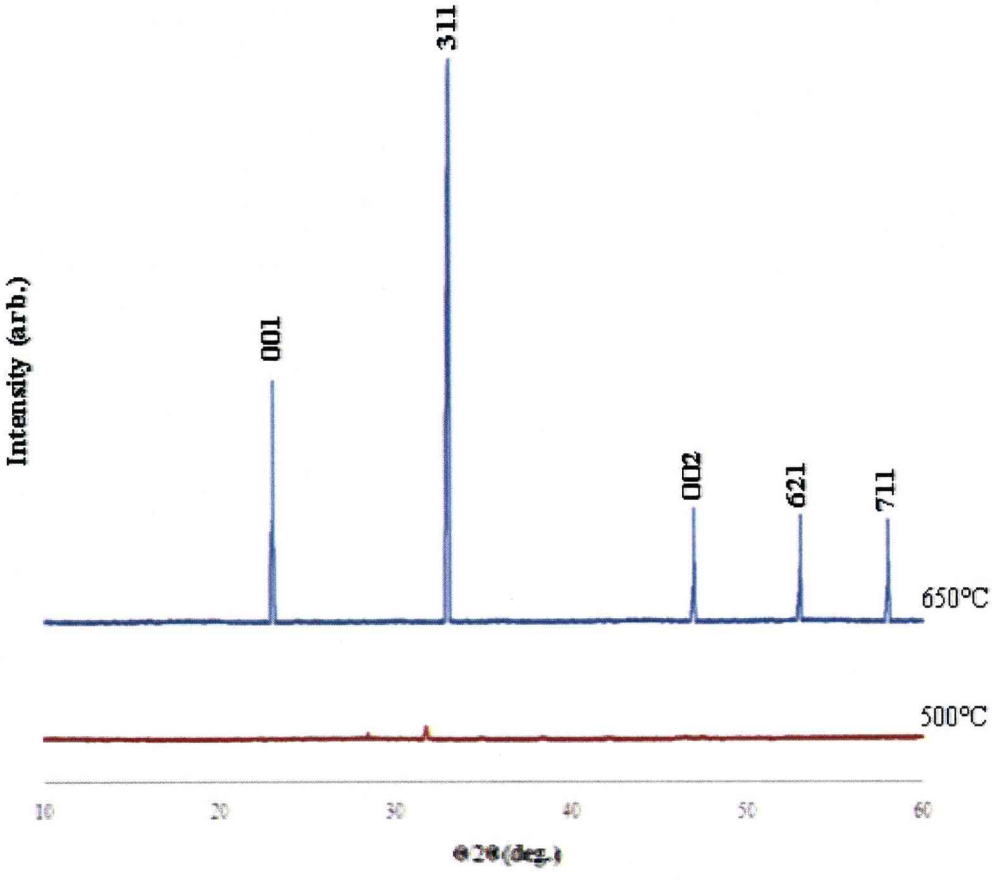

Figure 4.3: XRD patterns illustrating one strontium tantalate film deposited at 500°C and then annealed at 650°C for 15 min

4.3.3 Growth Rates and XRD Analysis of Bismuth Oxide

The progress in heterometal alkoxide chemistry described earlier $Sr\{Ta(OEt)_5(dmae)\}_2$, has led to the requirement of a compatible Bi source. Conventional sources ($Bi(C_6H_5)_3$)) and ($Bi(thd)_3$) are not particularly compatible with strontium tantalate, having significantly

higher thermal stabilities and different evaporation characteristics [5]. Bi-alkoxide, specifically $Bi(mmp)_3$, is a more suitable co-precursor, as it exhibits similar volatility and decomposition characteristics compared to the strontium tantalate heterometal alkoxide precursors. The precursor $Bi(mmp)_3$ was successfully used for the deposition of bismuth oxide films for substrate temperatures in the range 300 – 600°C. The variation in oxide growth rate with substrate temperature is illustrated in Figure 4.4. The most significant contribution to errors in the estimation of growth rate, arises from the use of crystalline densities rather than amorphous densities. The amorphous density of bismuth oxide is not readily available from the literature. However, it is the shape of the growth rate curve as a function of temperature that is the most important feature of the figure, rather than the absolute growth rates. The bismuth oxide growth rate curve from $Bi(mmp)_3$ correlates closely with the ST growth curve (Figure 4.1) from $Sr\{Ta(OEt)_5(dmae)\}_2$. This suggests that $Bi(mmp)_3$ is a suitable complementary source of Bi to the all alkoxide "single source" strontium tantalate precursors for SBT.

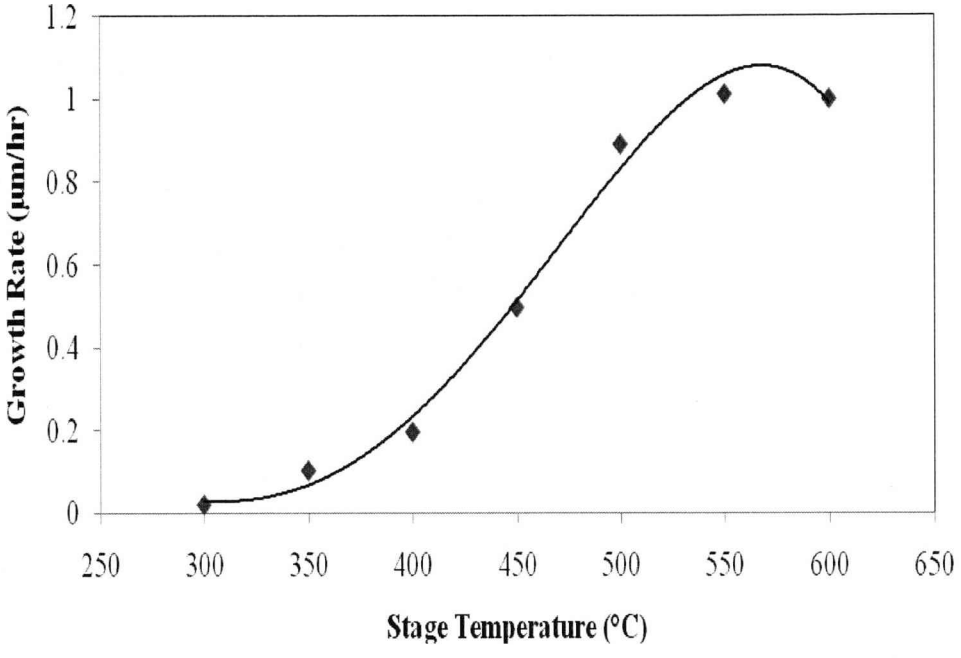

Figure 4.4: Bismuth oxide growth curve using $Bi(mmp)_3$

Figure 4.5 portrays an X-ray diffraction spectrum of a bismuth oxide film deposited at 500°C and 600°C. The diffraction pattern is dominated by a single peak due to the (111) reflection of α-Bi_2O_3 (P121/C1, ICSD; ID = 71396) [21].

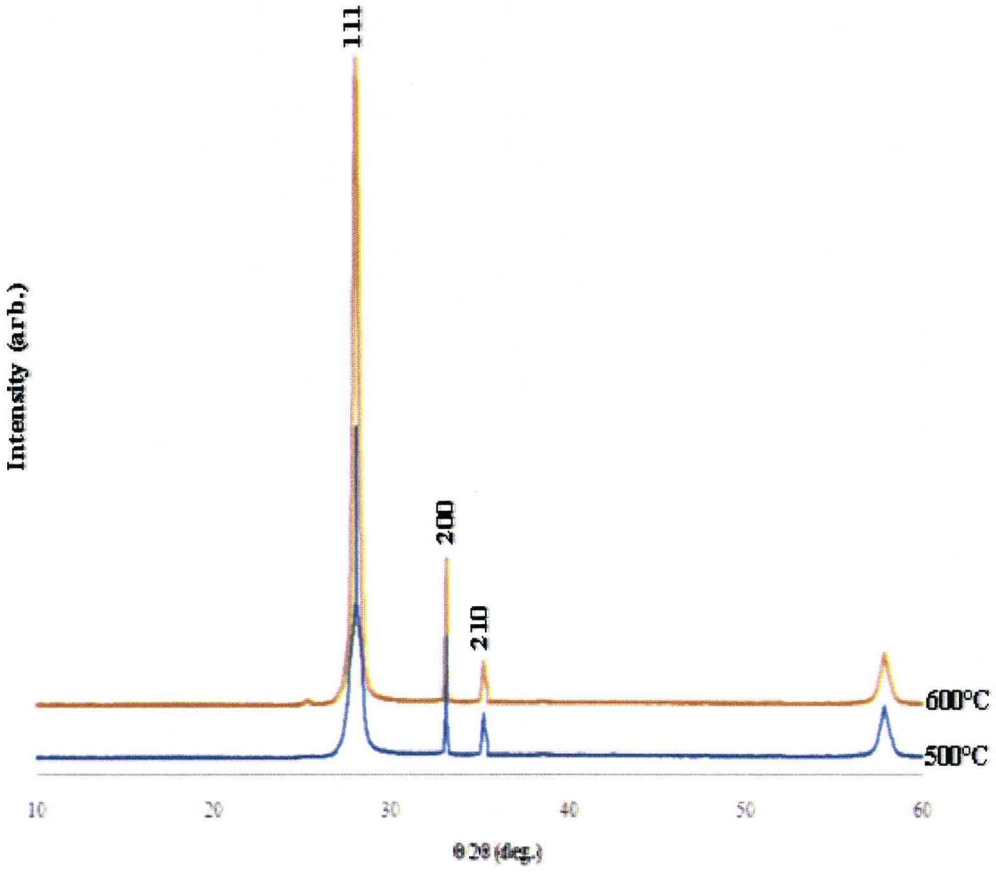

Figure 4.5: XRD pattern of a α-Bi_2O_3 deposited at 500°C and 600°C

4.4 Conclusions

In this chapter, the deposition of strontium tantalate and bismuth oxides thin films has been investigated from the single-source precursor $Sr\{Ta(OEt)_5(dmae)\}_2$ and $Bi(mmp)_3$ respectively. The composition of the strontium tantalate films was found to depend on growth temperature. The film composition was found to be tantalum-rich (Sr:Ta ~0.8) at the lowest growth temperature of 300°C. Between 350 – 400°C, the Sr:Ta ratio in the films reaches a maximum close to unity, followed by a decrease in the strontium content at higher temperatures. The 'optimum' growth temperature is found around 510°C, where the Sr:Ta ratio in the film is 0.5 - stoichiometry close to the $Sr:Ta_2O_6$ proportion found in the SBT composition. The $Bi(mmp)_3$ precursor deposited bismuth oxide over the temperature range of between 300 – 600°C. At higher temperatures X-ray diffraction revealed the films had a crystalline habit and consisted of the α-Bi_2O_3 phase.

4.5 References

[1] A. Gensbittel, A.F. Degardin, A.J. Kreisler, M. Guilloux-Viry, A. Perrin, P. Crozat, *Ferroelectronics*, **288**, 103 (2003).

[2] G. Rosenman, D. Shur, Y.E. Krasik, A. Dunaevsky, *J. Appl. Phys.*, **88** (11), 6109 (2000).

[3] R. Ramesh, S. Aggarwal, O. Auciello, *Mater. Sci. Eng. R.*, **32** (6): 191 (2001).

[4] C.A. Paz de Arauja, J.D. Cuchiaro, K.D. McMillan, M.C. Scott and J.F. Scott, *Nature*, **347**, 627 (1995).

[5] H. Funakubo, K. Ishikawa, T. Watanabe, M. Mitsuya and N. Nukaga, *Adv. Matter. Opt. Electron*, **10**, 193 (2000).

[6] J.F. Scott, F.M. Ross, C.A. Paz de Arauja, M.C. Scott, M. Huffman, in *Electroceramic Thin Films Part II: Device Applications* (Eds: O. Auciello, R. Ramesh), *MRS Bull*, **21** (7), 33, (1996).

[7] G.A. Smolenskii, V.A. Isupov and A.I. Agranovskara, *Sov. Phys. Solid State*, **1**, 149 (1959).

[8] T. Ami, K, Horinaka, C. Isobe, N. Nagel, M. Sugiyama, Y. Ikeda, K. Watanabe, A. Machida, K. Miura, M. Tanaka, *Mater. Res. Soc. Symp. Proc.*, **415**, 195, (1996).

[9] M.J. Crosbie, P.J. Wright, H.O. Davies, A.C. Jones, T.J. Leedham, P. O'Brien and G.W. Critchlow, *Chem. Vap. Deposition*, **5**, 9 (1999).

[10] A.C. Jones, N.L. Tobin, P.A. Marshall, R.J. Potter, P.R. Chalker, J.F. Bickley, H.O. Davies, L.M. Smith, G.W. Critchlow, *J. Mater. Chem.*, **14** (5), 887 (2004).

[11] S. Regnery, R. Thomas, H. Haselier, P. Ehrhart, R. Waser, P. Lehnen, S. Miedl, and M. Schumacher, *Mater. Res. Soc. Symp. Proc.*, **811**, D9.7.1 (2004).

[12] K. Ishikawa, N. Nukaga and H. Funakubo: *Jpn. J. Appl. Phys.*, **38**, 1970 (1999).

[13] N. Nukaga, K. Ishikawa, K. Shinozaki, N. Mizutani and H. Funakubo: *Key. Eng. Mater.*, **169-170**, 145 (1999).

[14] J.F. Roeder, B.C. Hendrix, F. Hintermeier, D.A. Desrochers, T.H. Baum, G. Bhandari, M. Chappius, P.C. Van Buskirk, C. Dehm, E. Fritsch, N. Nagel, H. Wendt, H. Cerva, W. Honlein and C. Mazure, *J. Eur. Ceram. Soc.*, **19**, 1463 (1999).

[15] C. Isobe, Ami, K. Hironaka, K. Watanabe, M. Sugiyama, N. Nagel, K. Katori, Y. Ikeda, C.D. Gutleben, M. Tanaka, H. Yaamoto and H. Yagi, *Integrated Ferroelectrics*, **14**, 95 (1997).

[16] H. Kodakura, Y. Okuhara, M. Mitsuya and H. Funakubo, *Chem. Vap. Deposition*, **6**, 225 (2000).

[17] W.A. Herrmann, N.W. Huber, O. Runte, Angew. *Chem. Int. Ed. Engl.*, **34**, 2187 (1995).

[18] W.C. Shin, K.J. Choi, E.S. Choi, C.M. Park and S.G. Yoon, *Int. Ferroelectrics*, **30**, 27 (2000).

[19] A.C. Jones, T.J. Leedham, P.J. Wright, M.J. Crosbie, K.A. Fleeting, D.J. Otway, P. O'Brien, M.E. Pemble, *J. Mater. Chem.*, **8**, 1885 (1998).

[20] T. Siegrist, R.J. Cava, J.J. Krajewski, *Mater. Res. Bul.*, **32**, 881 (1997).

[21] S.A. Ivanov, R. Tellgren, H. Rundlof, V.G. Orlov, *Powder Diffr.*, **16**, 227 (2001).

Chapter 5 MOCVD of Strontium Bismuth Tantalate – Superlattice Approach

5.1 Introduction

Non-Volatile Ferroelectric Random Access Memories (NV-FeRAM) are largely regarded as the ideal non-volatile memory due to their highly desirable performance features, namely: low power operation; high write speeds; high radiation hardness; and high endurance (read-write cycles). Strontium bismuth tantalate, $SrBi_2Ta_2O_9$ (SBT), is an emerging material for use in NV-FeRAM applications owing to its observed excellent resistance to fatigue degradation [1,2]. The ferroelectric phase of SBT is a layered bismuth oxide belonging to the m=2 Aurivillius family. Its structure can be considered as alternating Bi_2O_3 sheets and $SrTa_2O_6$ double perovskite-like layers.

SBT films have been deposited by a variety of techniques including metal-organic decomposition [3], pulsed laser ablation [4] and metal organic chemical vapour deposition (MOCVD) [5-8]. In MOCVD, the metal is transported in the vapour phase, via a volatile metal-organic

compound, which in the presence of oxygen, thermally decomposes on a heated substrate (e.g. Si, SiO_2, $SrTiO_3$). MOCVD has numerous advantages over other deposition techniques as it offers the potential for large area growth, excellent film uniformity, composition control, high film densities and high deposition rates. The process also offers excellent conformal step coverage at device dimensions of less than 2 μm. Furthermore, the MOCVD technique is compatible with existing processes used in silicon ULSI device fabrication. The development of MOCVD for the deposition of SBT has been restricted by a lack of suitable precursors. Conventional precursors, such as $Sr(thd)_2$ (thd = 2,2,6,6-tetramethylheptane-3,5-dionate), $Bi(C_6H_5)_3$, $BiMe_3$, $Bi(O^tC_5H_{11})_3$, $Ta(OEt)_5$ and $Ta(OPr^i)_4(thd)$ [9,10], have very different decomposition characteristics and physical properties. This disparity in the precursor properties results in poor film uniformity, composition control problems and reduced bismuth incorporation efficiency.

As discussed in Chapter 4, one solution to overcome the precursor issues for SBT growth, is to use ''single-source'' strontium tantalate heterometal alkoxide precursor, $Sr\{Ta(OEt)_5(dmae)\}_2$ (dmae = $OCH_2CH_2NMe_2$), which has been designed to regulate the Sr:Ta ratio [11,12] coupled with a separate Bi-alkoxide co-precursor, $Bi(mmp)_3$

(mmp=($OCMe_2$-CH_2OMe)) [13]. The separate $Bi(mmp)_3$ precursor allows independent control of the Bi incorporation. In practice, a common approach is to supply ''excess'' Bi to the growing layer [14,15] to ensure sufficient bismuth incorporation followed by annealing at temperatures between 700 – 800°C. The annealing causes 'out-diffusion' or expulsion of excess bismuth to the free surface producing the appropriate film composition and phase.

Initial attempts to depositing SBT were attempted using an approach based on the simultaneous injection of $Sr\{Ta(OEt)_5(dmae)\}_2$ and $Bi(mmp)_3$ precursor solutions. Measurement of the SBT film composition using AES indicated that at a growth temperature of 500°C layers consisting of the vital 1:2 Sr:Ta ratio required for the SBT stoichiometry were produced. The injection rate of the Bi precursor was varied between 0 – 25.2 ml/h to investigate the influence of $Bi(mmp)_3$ partial pressure on the Bi incorporation in the deposited SBT films. The total composition of the SBT films was determined using AES measurements, the results of this summarised in [16]. With increasing $Bi(mmp)_3$ partial pressure, the level of Bi incorporation increased noticeably in a non-linear manner. Moreover, the Sr incorporation is rapidly suppressed as the Bi content exceeds a few atomic percent.

To overcome the issue of introducing Bi into the film without loss of Sr, a series of Bi_2O_3 / $SrTa_2O_6$ superlattices (SLs) will be investigated in this chapter. In addition, the effect of post-deposition annealing on the film composition and microstructure will be analysed using cross section TEM (HR-TEM) and medium energy ion scattering (MEIS). These techniques enable a depth profile of the composition to be measured and reveal the structure of the SLs. X-ray diffraction (XRD) measurements are used to determine the crystallinity and phase of the films as-grown and post-annealing.

5.2 Experimental

A horizontal Aixtron AIX 200FE reactor fitted with a Trijet™ liquid injector system was used to deposit the oxide films. SLs were deposited via liquid injection MOCVD on Si(100) substrates using 0.1 molar precursor solutions in n-heptane. The precursors were vaporised at 200°C and transported into the reactor using a flow rate of 200 sccm of argon. Substrates were rotated at 60 rpm during deposition to improve film uniformity. Based on previous work (Chapter 4), a growth temperature of 500°C was used to control the Sr:Ta (1:2) ratio. A reactor pressure of 5 mbar was used and an O_2 flow rate of 100 sccm was chosen [11,12]. The precursors were independently injected using 1 pulse/sec with average flow rates of ~3 µl/pulse and ~2.9 µl/pulse for the $Sr(Ta(OEt)_5(dmae))_2$ and $Bi(mmp)_3$ respectively. A set of 15 period SLs were deposited using 20 pulses/period of $Sr\{Ta(OEt)_5(dmae)\}_2$ and 0 – 30 pulses/period of $Bi(mmp)_3$.

Medium energy ion scattering (MEIS) experiments were carried out using the CCLRC Daresbury facility [17]. A 200 keV He^+ ion beam was employed with a current of up to 200 nA and a dose per data set of 4.4 x 10^{15} atms/cm^2. The angle and energy of the scattered ions were

determined using a state-of-the-art toroidal electrostatic energy analyser with a position-sensitive detector. This allowed the simultaneous collection of ions from a 27° range of scattering angles and with a range of energies equal to 1.6% of the pass energy.

5.3 Results and Discussion

5.3.1 Growth Rates and AES Analysis of SBT

A series of bismuth oxide / strontium tantalate SLs were grown with varying thicknesses of Bi_2O_3 interlayers. A similar approach has been employed by Funakubo and co-workers to control the Bi incorporation in the deposition of the bismuth titanate phase, $Bi_4Ti_3O_{12}$ [18]. The effect of $Bi(mmp)_3$ pulses per period on film weight gain, is shown in Figure 5. 1. It indicates that the first 10 or so pulses of $Bi(mmp)_3$ per period do not contribute significantly to the film mass (growth rate). Auger electron spectroscopy (AES) analysis of these samples shows that the initial $Bi(mmp)_3$ pulses per period, do not result in measurable incorporation of Bi. However, more interestingly, the initial pulses of $Bi(mmp)_3$ are found to reduce the strontium incorporation, which tends to suggest that the bismuth precursor reacts with the growth surface and depletes the strontium at the surface (Figure 5.2). This also suggests that surface-reactions between the two precursors, rather than gas-phase ones, are responsible for the strontium depletion observed in co-deposited films [16].

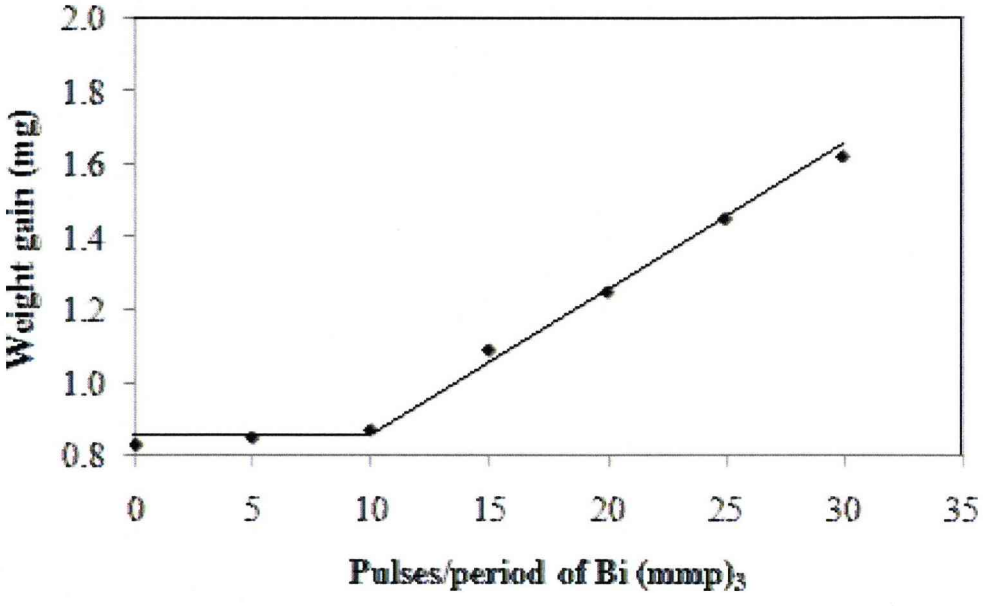

Figure 5.1: Weight gain (on 2" Si(100) wafers) measurements of 15 period strontium tantalate/bismuth oxide SLs as a function of $Bi(mmp)_3$ pulses/period using 20 pulses/period of $Sr\{Ta(OEt)_5(dmae)\}_2$

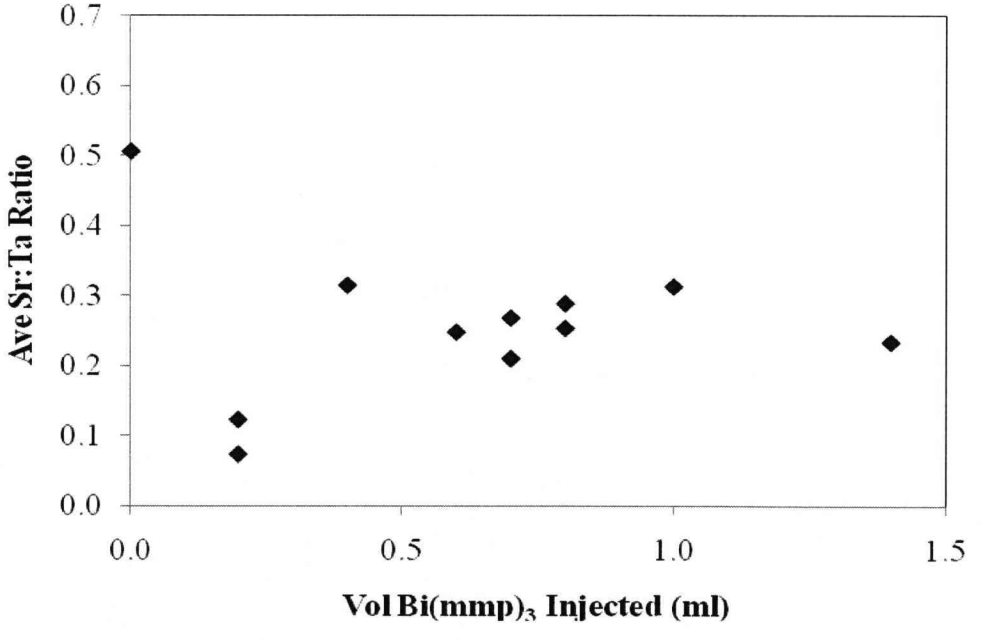

Figure 5.2: Strontium incorporation as the volume of $Bi(mmp)_3$ is injected

From a mass balance analysis of the SLs (assuming the oxide densities are 4.56 g/cm^{-3} and 8.9 g/cm^{-3} for strontium tantalate and bismuth oxide respectively) it was estimated that each strontium tantalate layer is ~5.7 nm thick and the bismuth oxide layer thickness increases in a linear fashion from 0 (using 10 pulses/period of $Bi(mmp)_3$) to ~6 nm (using 25 pulses/period of $Bi(mmp)_3$). Coupling this information together with AES analysis, showed that the SL deposited using 20 pulses/period of each precursor was closest to the required 1:2:2 Sr:Ta:Bi stoichiometry. Therefore the chosen sample for the annealing study was annealed at 600, 700 and 800°C for 15 minutes in air.

5.3.2 XRD Studies of SBT

Figure 5.3 illustrates the X-ray diffraction (XRD) patterns of the as-deposited and annealed SL obtained using the Cu $K\alpha_{1,2}$ line (λ=0.1542 nm). The most intense diffraction feature from the as-grown sample at ~28.1° (2θ) is due to the (111) reflection of α-Bi_2O_3 [19]. This is superimposed on a broader, less intense feature centred on 28.8°, believed to be the (111) reflection of fluorite phase SBT [20]. The fluorite structure in the SBT system has only eight fold co-ordinated cation sites

within its lattice. Sr^{2+} and Bi^{3+} are able to form stable eight-fold oxygen co-ordination, whereas the smaller Ta^{5+} would prefer an octahedral co-ordination. As a result, SBT compounds tend to form a defective fluorite structure in which Sr, Bi and Ta are surrounded by six (not 8) oxygen ions [21]. Hence, TaO_6 octahedra already exist in the fluorite phase. Therefore, it is believed that the transformation between amorphous SBT and the complex bismuth-layered perovskites goes through the fluorite structure [22]. The defective oxygen co-ordination, gives the SBT-fluorite structure a metastable nature. This fact, together with the random mixing of cations within the lattice, explains how the fluorite phase acts as an intermediate phase during the crystallisation of the bismuth-layered perovskite [23]. Consequently, the presence of the fluorite phase in Figure 5.3 is indicative of excess Bi and is expected to be present at the interfaces between bismuth oxide and the strontium tantalate layers in the superlattices.

After annealing the SL at temperatures of 600°C or above, the fluorite phase is transformed to either: a) a Bi-layered perovskite or b) a Bi deficit – pyrochlore phase. In this annealing study, the (111) feature of the α-Bi_2O_3 is suppressed on heating. The intensity of the underlying broad XRD feature increases with annealing temperature up to 700°C. This

suggests that Bi diffuses into the strontium tantalate layers, allowing the formation of more fluorite SBT. After annealing at 800°C, a slight shift in the main peak to 29.2° was observed and a number of weak diffraction features became visible. These features are consistent with the Aurivillius phase of SBT [24], where the main feature at 29.2° is the (115) reflection.

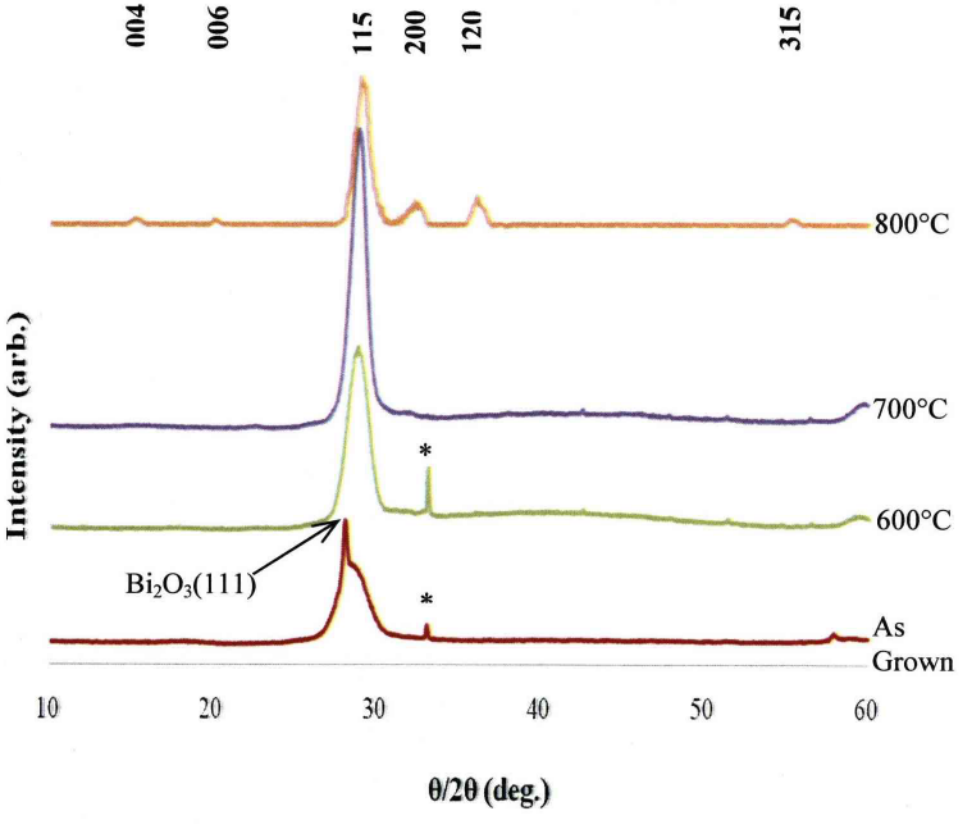

Figure 5.3: X-ray diffraction patterns of the 15 period SL deposited using 20 pulses/period of each precursor, as grown and after annealing for 15 mins in air. (Peaks marked with * are due to the Si(200) of the substrate)

5.3.3 MEIS Studies of SBT

MEIS was used in order to investigate the inter-diffusion occurring between the bismuth oxide and strontium tantalate layers during annealing. Due to the inelastic scattering processes that He-ions undergo as a function of depth below the sample surface, 1D energy distribution gives an effective depth profile of the target atoms. Figure 5.4(a) portrays the scattered ion energy–angle data tile obtained from the first three periods of the as-deposited (unannealed) SL. The darker regions indicate higher ion counts on the false colour scale used here. By taking a 'slice' through the '2D' data (energy versus angle) tile, a 1D energy spectrum is obtained. When this is analysed to account for scattering angles, compositional depth profile of the constituent elements can be determined. Figure 5.4(b) shows the 1D energy spectrum of the superlattice as a function of annealing temperature. It also includes elemental depth distribution obtained from the MEIS data of the as-deposited film after modelling in SIMNRA [25]. As illustrated by the elemental depth distribution, main peaks in the MEIS depth distribution result from a convolution of scattered ions from bismuth and tantalum atoms in adjacent bismuth oxide and strontium tantalate layers of the SL. The SIMNRA model, which uses the Ziegler-Biersack values of

electronic stopping power, reveals a repeat periodicity in the as-deposited SL. The periodic repeat length is of the order of ~10 nm, which is consistent with the cross section TEM data reported in the next section. The MEIS data shows that as the annealing temperature is increased, the inter-diffusion between the bismuth oxide and strontium tantalate layers progressively increases too. Following annealing for 15 minutes at 800°C, the superlattice is effectively converted to SBT. This observation is consistent with the the XRD data shown in Figure 5.3.

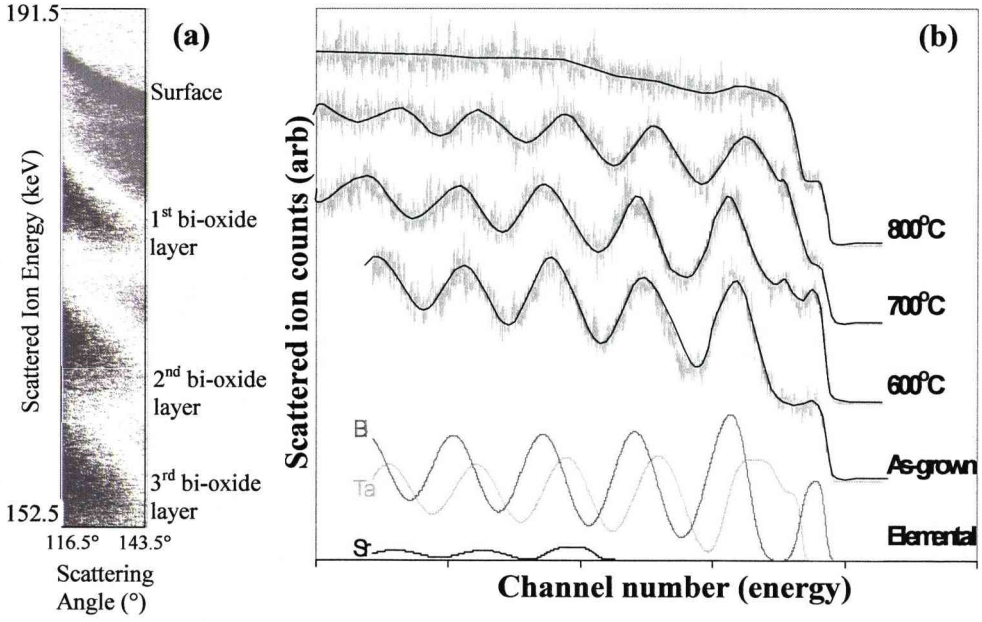

Figure 5.4: (**a**) MEIS 2D energy/angle data tile of the first three periods of an as-deposited SL. (**b**) 1D energy distribution as a function of anneal temperature including deconvoluted elemental depth distribution of the as-grown SL MEIS data

5.3.4 TEM Studies of SBT

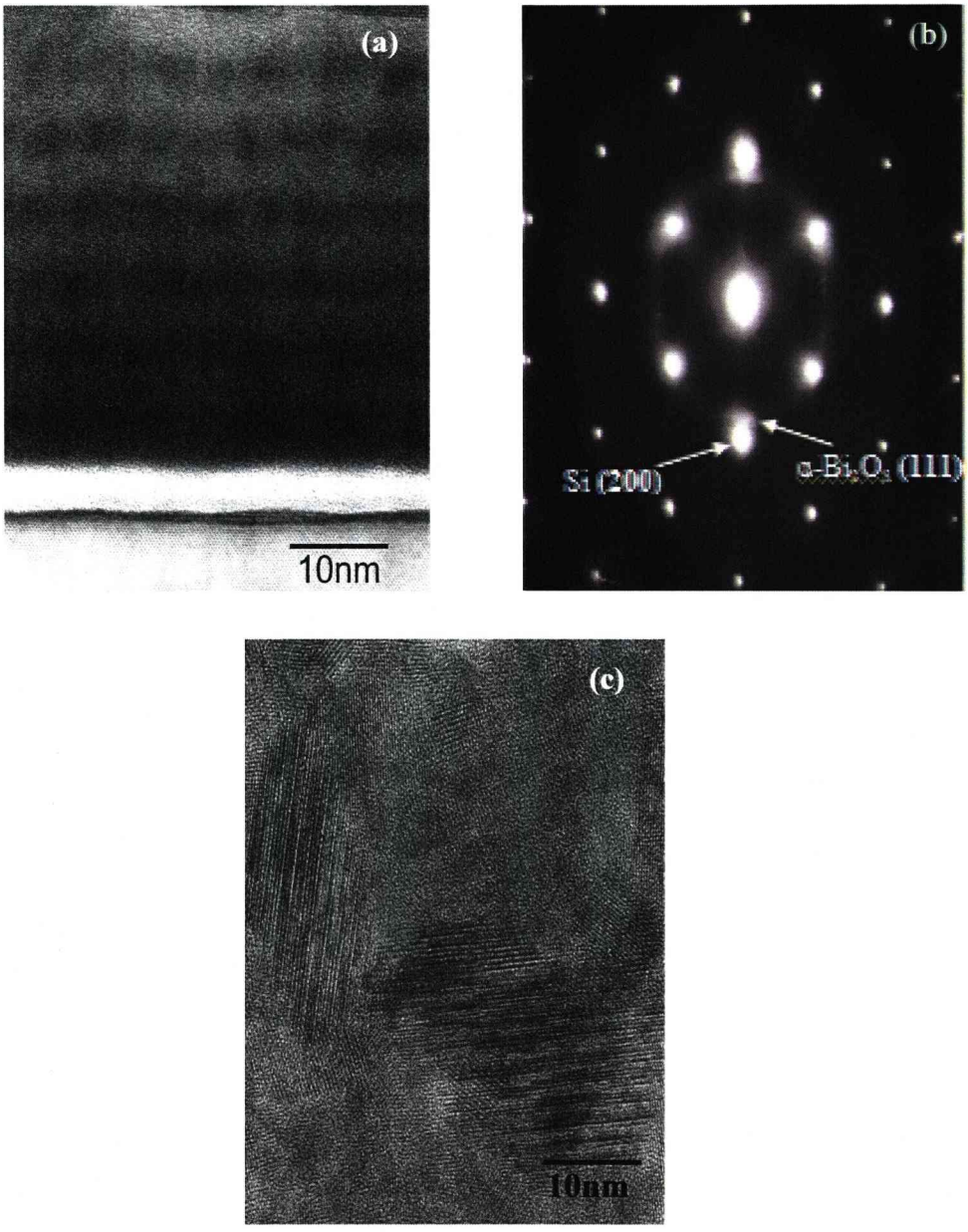

Figure 5.5: (**a**) HR-TEM image of the SL as grown in [011] zone axis of the Si substrate. (**b**) Illustrates SAD pattern of as-grown SL. (**c**) HR-TEM image of the SL annealed at 800°C.

Figure 5.5(a) shows a cross-sectional TEM image of the as-deposited SL sample viewed along the Si[011] zone axis. The strontium tantalate and bismuth oxide layers of the SL are clearly discernible as periodic light and dark regions arising from the varying atomic number (Z) contrast respectively. The very bright region above the substrate is an interfacial layer of SiO_2 ~4 nm thick. The SL is found to contain two distinct regions, the first 7 periods deposited have a periodicity of ~8 nm (~4 nm strontium tantalate, ~4 nm bismuth oxide) and the remaining 8 periods ~10.5 nm (~5.9 nm strontium tantalate, ~4.6 nm bismuth oxide). This difference is due to a slight increase in precursor volumes used in the second half of the deposition run. The bismuth oxide layers show lattice fringes with spacing of ~3.3Å nearly parallel to the substrate Si(100) plane and is responsible for the arced diffracton spots aligned with the Si(200) spots in select area diffraction (SAD) pattern, generated by the whole cross section including Si, see Figure 5.5(b). These are consistant with the (111) reflection of α-Bi_2O_3 [19]. Figure 5.5(c) portrays a HR-TEM image (viewed along the Si[011] zone axis) of a region of the sample (upper 8 periods) after annealing at 800°C for 15 mins, this clearly shows that the film has been transformed from the SL structure into a polycrystalline film. The annealed sample appears to have a higher level of crystallininty in the upper 8 period region than in the lower 7

period region. This may be indicative of an incomplete transformation of the SL to crystalline SBT.

5.4 Conclusions

The synthesis of $SrBi_2Ta_2O_9$ (SBT) thin films has been investigated using a superlattice approach. Thin films were deposited on Si by independent injection of each source to produce Bi_2O_3 - $SrTa_2O_5$ SLs. The effects of post-deposition annealing have been investigated using TEM, STEM and MEIS to depth profile the SLs. XRD has also been used to characterise the conversion of the superlattices. Post-growth annealing, the optimised SLs converts the distinct layers of Bi_2O_3 and $SrTa_2O_5$ containing some interfacial pyrochlore, into a single layer of the perovskite SBT phase.

The superlattice approach has enabled the low temperature synthesis of films consisting of a nominal $SrBi_2Ta_2O_9$ composition, at temperatures as low as 500°C. The effects of post-deposition annealing have been investigated using MEIS to depth profile the SLs and measure the interlayer inter-diffusion as a function of temperature. Post-growth annealing converts the distinct layers of Bi_2O_3 and $SrTa_2O_5$ into a single polycrystalline layer of the perovskite-like SBT phase.

5.5 References

[1] C.A. Paz de Arauja, J.D. Cuchiaro, K.D. McMillan, M.C. Scott, J.F. Scott, *Nature,* **347**, 627 (1995).

[2] H. Funakubo, K. Ishikawa, T. Watanabe, M. Mitsuya, N. Nukaga, *Adv. Mater. Opt. Electron.* **10**, 193 (2000).

[3] T. Mihara, H. Yoshimori, H. Watanabe, C.A. Paz de Arauja, *Jpn. J. Appl. Phys.*, **34**, 5233 (1995).

[4] P.X. Yang, N.S. Zhou, L.R. Zheng, H.X. Lu, C.L. Lin, *J. Phys. D, Appl. Phys.*, **30**, 527 (1997).

[5] T. Li, S.B. Desu, C.H. Peng, M. Nagata, *Appl. Phys. Lett.*, **68**, 616 (1996).

[6] H. Funakubo, N. Nugaka, K. Ishikawa, T. Watanabe, *Jpn J Appl Phys.*, **38**, L199 (1999).

[7] F. Felten, J.P. Senateur, F. Weiss, R. Madar, A. Abrutius, *J. Phys. IV,* France, **5**, C5-1079 (1995).

[8] A.C. Jones, T.J. Leedham, P.J. Wright, M.J. Crosbie, P.A. Lane, D.J. Williams K.A. Fleeting, D.J. Otway, P. O'Brien, *Chem. Vap. Deposition*, **4**, 46 (1998).

[9] J.F. Roeder, B.C. Hendrix, F. Hintermeier, D.A. Desrochers, T.H. Baum, G. Bhandari, M. Chappius, P.C. Van Buskirk, C. Dehm, E.

Fritsch, N. Nagel, H. Wendt, H. Cerva, W. Honlein, C. Mazure, *J. Eur. Ceram. Soc.*, **19**, 1463. (1999).

[10] C. Isobe, T. Ami, K. Hironaka, K. Watanabe, M. Sugiyama, N. Nagel, K. Katori, Y. Ikeda, C.D. Gutleben, M. Tanaka, H. Yaamoto, H. Yagi, *Integrated Ferroelectrics*, **14**, 95 (1997).

[11] A.C. Jones, N.L. Tobin, P.A. Marshall, R.J. Potter, P.R. Chalker, J.F. Bickley, H.O. Davies, L.M. Smith, G.W. Critchlow, *J. Mater. Chem.*, **14** (5), 887 (2004).

[12] R.J. Potter, P.A. Marshall, J.L. Roberts, A.C. Jones, P.R. Chalker, M. Ritala, M. Vehkamäki, P.A. Williams, H.O. Davies, N.L. Tobin, L.M. Smith. *MRS Fall*, **784** (2003)

[13] P.A. Williams, A.C. Jones, M.J. Crosbie, P.J. Wright,J.F. Bickley, A. Steiner, H.O. Davies, T.J. Leedham, G.W. Critchlow, *Chem. Vap. Depos.*, **7**, 205 (2001).

[14] K. Amanuma, T. Hase, Y. Miyasaka, *Mater. Res. Soc. Symp. Proc.*, **361**, 21 (1995).

[15] H. Watanabe, T. Mihara, H. Yoshimori, C.A. Araujo, *Jpn. J. Appl. Phys.*, **34**, 5240 (1995).

[16] P.R. Chalker, R.J. Potter, J.L. Roberts, A.C. Jones, L.M. Smith, M. Schumacher, *J. Crystal Growth*, **272**, (1-4), 778 (2004).

[17] P. Bailey, T.C.Q. Noakes, D.P. Woodruff, *Surface Science*, **426**, 358 (1999).

[18] T. Watanabe, H. Funakubo, *Jpn. J. Appl. Phys.*, **39**, 5211 (2000).

[19] S.A. Ivanov, R. Tellgren, H. Rundlof, V.G. Orlov, *Powder Diffr.*, **16**, 227 (2001).

[20] M. Osada, M. Kakihana, M. Mitsuya, T. Watanabe, H. Funakubo, *Jpn. J. Appl. Phys.*, **40**, L891 (2001).

[21] J.F. Scott, *IEICE Trans. Electron.* E81 –C(4), 477 (1998).

[22] A.J. Hartman, M. Huffman, M. Azuma, Y. Shimada, T. Otsuki, G. Kano, L.D. McMillian and C.A. Araujo, *Symposium on VLSI Technology Digest of Technical Papers*, 153 (1994).

[23] M.A. Rodriguez, T.J. Boyle, C.D. Buchheit, R.G. Tissot, C.A. Drewien, B.A. Hernandez, and M.O. Eathough, *Integrated Ferroelectrics*, **14**, 201 (1997).

[24] C. Muller, F. Jacob, Y. Gagou, E. Elkaim, *J. Appli. Cryst.*, **36**, 880 (2003).

[25] M. Mayer, Proc. of the 15th International Conference on the Application of Accelerators in Research and Industry, J. L. Duggan & I.L. Morgan (eds.), AIP Conf. Proc., **475**, 541 (1999).

Chapter 6 ALD of Strontium Bismuth Tantalate – Superlattice Approach

6.1 Introduction

The development of MOCVD and ALD presents considerable potential benefits for large-area processing of SBT and integration with silicon technology. The two techniques are exceptionally complementary to modern manufacturing processes for microelectronics. As outlined in the earlier chapters, liquid injection MOCVD is extensively utilised for the deposition of thin-films such as SBT [1]. However, some additional factors required by the MOCVD make it less favourable when compared with ALD. For example, precursors in chosen solvents must be soluble, stable and non-reactive with other precursors for long periods. The various precursors need to be capable of depositing oxide films in a similar temperature regime to optimise compositional uniformity. This is achieved by using single-source heated evaporators with fixed temperatures.

ALD is a low-temperature modification of CVD or MOCVD [2], whereby gaseous precursors are sequentially dosed into a vacuum chamber under computer control. The sub-nanometre repeated cycles of ALD consist of three stages:

1. The first precursor (an oxidant e.g. H_2O or ozone) chemisorbs to the substrate surface [3].
2. Prior to the next pulse, volatile reaction products are cleansed from the reactor by evacuation or use of an inert gas. This ensures excess precursor and reaction by-products are removed thus eliminating gas phase reactions [4].
3. Subsequently, the second inorganic precursor is introduced and reacts with the first, hence yielding a monolayer of film.

The whole cycle is repeated until the appropriate film thickness is achieved. This model of the ALD process, is considered as a 'self-limiting' mechanism, causes the film growth to halt automatically at one or two monolayers per cycle. As a result, the film growth rate becomes independent of the precursor pulse length; so long as 'saturative' doses are introduced during each pulse. Significant advantages of ALD include

excellent thickness control and perfect step-coverage of high aspect ratio structures. Consequently producing three-dimensional structures is achievable in structures otherwise too complex to fabricate using physical vapour deposition methods e.g. via holes [5,6].

The purpose of this chapter is to describe further investigations made to deposit SBT. It highlights the significant potential of using the single-source strontium tantalate precursor coupled with $Bi(mmp)_3$ to deposit SLs of strontium tantalate and bismuth oxide by ALD. The outcome of post-deposition annealing on SL structures produced using these precursors is investigated. The resulting ALD SBT layers have been characterised by XRD, MEIS and TEM. The reason for choosing ALD was the intention of extending the SBT deposition to lower temperatures than achievable with MOCVD. In doing so, the information gained and the arising results obtained in this investigation can make a unique contribution to the state-of-the-art at the time of writing.

6.2 Experimental

Thin films of strontium tantalate were deposited from $Sr\{Ta(OEt)_5(dmae)\}_2$. Bismuth oxide layers were deposited from $Bi(mmp)_3$. SLs of strontium tantalate - bismuth oxide were deposited on Si(100) substrates using a horizontal Aixtron AIX 200FE reactor fitted with a Trijet™ liquid injector system. The growth conditions for the abovementioned precursors are presented in Table 6.1. Characterisation techniques such as XRD, MEIS and TEM (see Chapter 3 for more detail) were used to examine and analyse the composition and structure of the thin films deposited. A comparison study has been carried out between the MOCVD (Chapter 5) and the ALD data.

Parameter	**$Sr\{Ta(OEt)_5(dmae)\}_2$**	**$Bi(mmp)_3$**	**SBT**
Reactor pressure	5 mbar	5 mbar	5 mbar
Evaporation temperature	200°C	200°C	200°C
Precursors pulse length	2 sec.	2 sec.	2 sec.
Precursor purge time	2 sec.	2 sec.	2 sec.
Water pulse length	0.5 sec.	0.5 sec.	0.5 sec.
Water purge time	3.5 sec.	3.5 sec.	3.5 sec.
Substrates	Si(100)	Si(100)	Si(100)
Growth temperature range	150 – 400°C	200 – 300°C	250°C

Table 6.1: Reactor growth conditions (Aixtron) for ALD

6.3 Results and Discussion

6.3.1 Growth Rates of Strontium Tantalate

The single-source precursor $Sr\{Ta(OEt)_5(dmae)\}_2$ was successfully used to deposit strontium tantalate films under ALD conditions, over the substrate temperature range from 150 – 400°C. Figure 6.1 illustrates the variation in oxide film thickness/mole with substrate temperature for both ALD and MOCVD deposition techniques. It was noted earlier (Chapter 3) that the errors in estimating growth rate arise from the measurement of weight gains. Figure 6.1 uses a 'normalised' weight gain per mole of injected precursor to enable the comparison of the ALD and MOCVD processes. This comparison means that some small addition error is incorporated due to the estimation of injected precursor volumes. As observed from the ALD curve, at low temperatures (150°C), film growth was achieved at a rate of 400 – 450 μm/mole. By contrast, even at an increased temperature of 300°C a relatively insignificant growth rate/mole was found by MOCVD. This highlights that the ALD technique is driven by surface thermodynamic effects (enthalpy), rather than by Arrhenius driven ones in the MOCVD growth regime. ALD is capable of

depositing films from strontium tantalate precursors at considerably lower temperatures than MOCVD.

It was noted in Chapter 4 that the growth rate of strontium tantalate increases exponentially with substrate temperature, between 400 and 550°C and then tails off above 550°C. The strontium tantalate growth behaviour under the ALD conditions shows that the growth rate between 150 – 300°C is almost constant. Above this temperature a component of CVD-like growth occurs causing the growth rate to increase with temperature again like the MOCVD case. The data indicates that $Sr\{Ta(OEt)_5(dmae)\}_2$ precursor is suitable for both ALD and MOCVD.

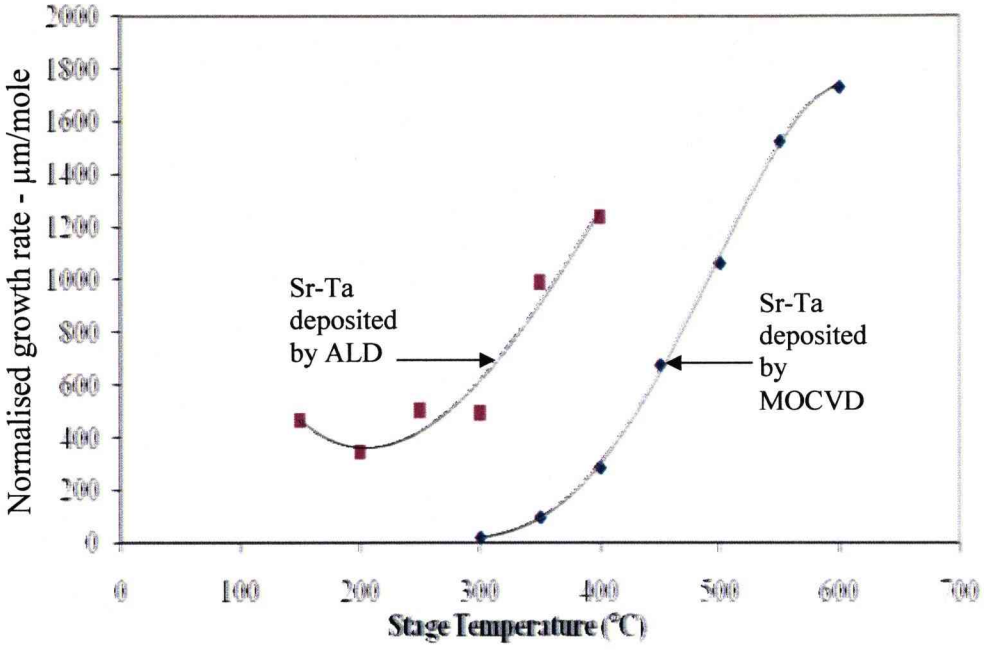

Figure 6.1: Strontium tantalate ($Sr\{Ta(OEt)_5(dmae)\}_2$) normalised growth rate in terms of thickness deposited / mole of precursor injected by ALD and MOCVD

6.3.2 XRD Studies of Strontium Tantalate

In order to understand the composition and phases present in the strontium tantalate films, annealing studies were made using the ALD grown films, which were examined by XRD. It was noted that the as-deposited strontium tantalate films grown at substrate temperatures

between 150 – 400°C exhibit an amorphous-like microstructure and demonstrate no crystalline diffraction features in their XRD patterns.

It was evident, after investigation of various ALD deposited strontium tantalate films, over numerous annealing temperatures and periods of time, that films undergo crystallisation at 550°C (minutes in air) as illustrated in Figure 6.2. The focus of these experiments was directed towards the films grown at 250°C because the strontium tantalate growth data showed favourable characteristics. The diffraction patterns of the annealed films closely resembles that of a $Sr_{2.83}Ta_5O_{15}$ (Sr:Ta ratio of 0.57) phase identified by Siegrist et al. [7] (P4/MBM, ICSD; ID = 24663). The XRD data from the annealed ALD grown films also resembles those of the annealed films deposited by MOCVD discussed in Chapter 4. The main difference between the ALD and MOCVD grown materials is the deposition and annealing temperatures.

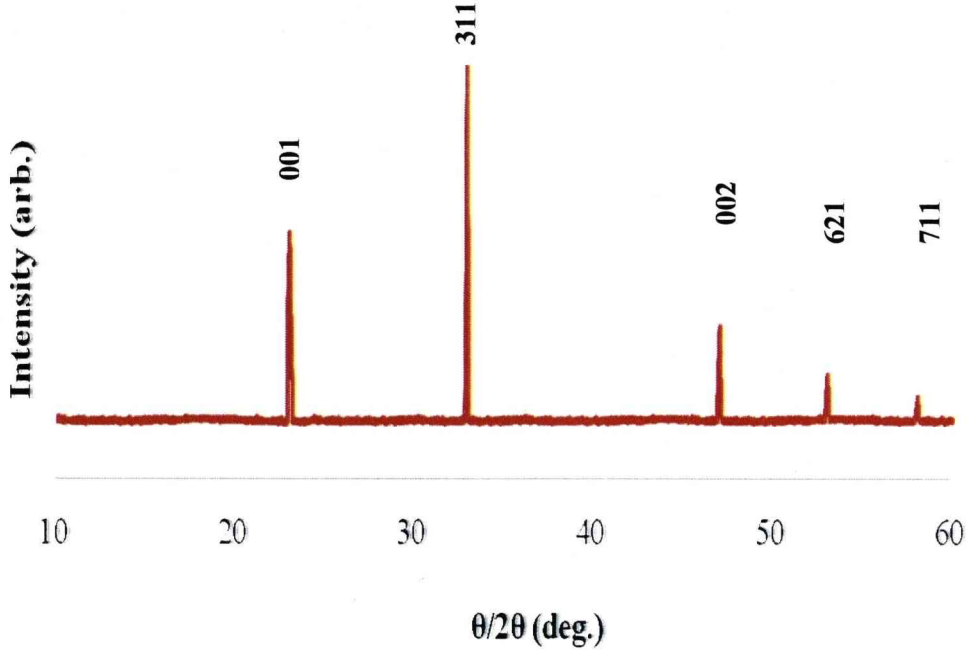

Figure 6.2: XRD pattern of strontium tantalate film deposited at 250°C and annealed at 550°C for 15 min

6.3.3 MEIS Studies of Strontium Tantalate

Medium energy ion scattering was used in order to investigate the effect of annealing on the strontium tantalate thin film. A 200 keV He^+ ion beam was focused incident on the surface normal (Si(100)) and the emerging back-scattered ions were collected from the Si[111] direction. Heavier target atoms e.g. tantalum cause higher energy He^+ recoils and

they appear at the top of the 2D energy – scattering angle MEIS map shown in Figure 6.3.

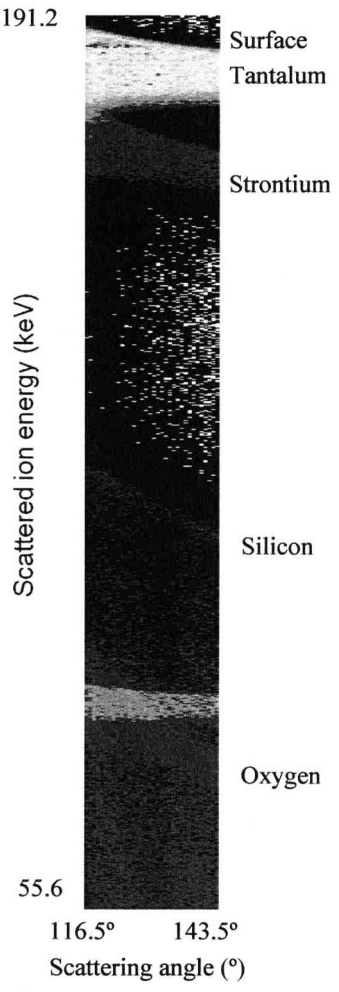

Figure 6.3: MEIS 2D energy/angle data tile of an as-deposited strontium tantalate thin film

The scatterred ions undergo inelastic scattering processes as a function of depth below the sample surface so the surface of the tantalum distribution occurs at the top of the map. Below the surface signal the thickness

distribution or 'depth profile' of tantalum is seen. The distribution of strontium is seen at lower energies and the signal due to oxygen occurs at the bottom of the profile. It is more convenient to integrate the scattered ion intensity across a small range of scattering angles (~4°) at each energy and this data can be replotted as a 1D energy distribution, which gives an effective depth profile of the target atoms.

1D energy depth profiles were collected from the as-grown strontium tantalate thin film and after annealing at 600 and 700°C in air for 15 minutes.

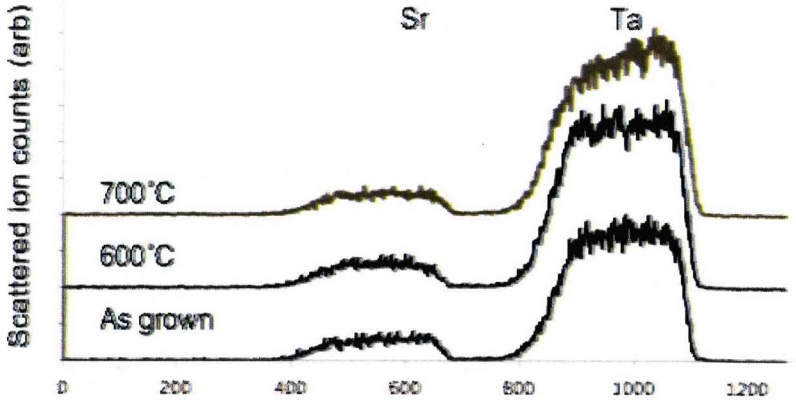

Figure 6.4: 1D MEIS energy depth profile of an as-deposited strontium tantalate thin film and after annealing at 600 and 700°C

Figure 6.4 reveals that the strontium tantalate is relatively impervious to the annealing conditions used. The low energy (channel number) parts of the tantalum and strontium distributions correspond to the interface between the oxide thin film and the silicon substrate. Little or no inter-diffusion is observed at the interface at either the Sr or Ta profiles. The only apparent effect of annealing on the films is noticed in the tantalum profile of the film after annealing at 700°C. A small increase in the Ta intensity at the surface is observed. Detailed investigation of the profile suggests that this is not due to diffusion or segregation, but is more likely due to the crystallisation of the film. As a material crystallises and the cations and anions become ordered on lattice sites, the cross section (or 'visibility') to ion scattering increases.

Overall the MEIS studies indicate that the strontium tantalate film is relatively inert to any interaction with the silicon substrate within the temperature range examined.

6.3.4 Growth Rates and XRD Analysis of Bismuth Oxide

$Bi(mmp)_3$ is highly reactive towards moisture and was loaded into the reactor under inert gas purge. Alternate pulsing of $Bi(mmp)_3$ and H_2O was found to produce bismuth oxide films on Si(100) substrates at 200 – 350°C (Figure 6.5). Uniform bismuth oxide thin films were deposited with thickness/mole rates between 1.5 – 150 μm/mole, however, the reproducibility of the film growth was poor. Above 350°C, bismuth oxide film growth was not possible because of decomposition of the precursor. Reducing the deposition temperature below 200°C would require extended purging times for both H_2O and $Bi(mmp)_3$.

A possible reason for the lack of reproducibility of bismuth oxide growth might be because of reduction of bismuth to a metallic form when no other metal oxides are present in the film, leading to termination of the growth. Bismuth is easily reduced to metallic form under vacuum conditions in ALD as already observed by Schuisky et al. [8]. A further possible reason for the poor reproducibility, which must be considered, is that impurities interfere with the film growth reactions.

Figure 6.5 illustrates the variation in oxide film growth rate with substrate temperature for both ALD and MOCVD deposition regimes. The plot shows a 'normalised' weight gain per mole of injected precursor to enable the comparison of the ALD and MOCVD processes. This comparison means that a small additional error is inherent in the growth rates due to the estimation of injected precursor volumes. As observed, the ALD curve follows a similar trend to the MOCVD one; however, the ALD films can be produced at lower temperatures. This highlights the fact that ALD growth is dominated by surface thermodynamic considerations and is capable of depositing $Bi(mmp)_3$ precursors at considerably lower temperatures than MOCVD.

The bismuth oxide growth curve of $Bi(mmp)_3$ corresponds closely with the temperature regime found in the strontium tantalate curve (Figure 6.1) of $Sr\{Ta(OEt)_5(dmae)\}_2$. This suggests that $Bi(mmp)_3$ is a suitable complementary source of Bi to the all alkoxide "single source" strontium tantalate precursors for SBT.

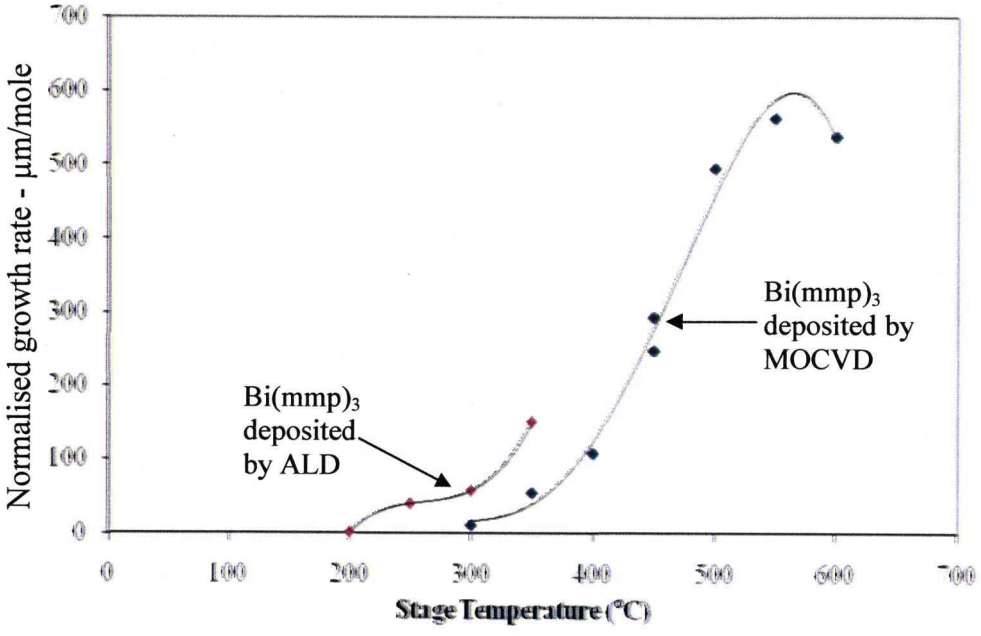

Figure 6.5: Bismuth oxide $Bi(mmp)_3$ normalised growth rate in terms of thickness deposited / mole of precursor injected by ALD and MOCVD

Figure 6.6 shows an X-ray diffraction pattern of a film deposited at 350°C. The pattern is dominated by a single peak due to the (111) reflection of α-Bi_2O_3 (P121/C1, ICSD; ID = 71396) [9]. The XRD data also resembles the XRD deposited by MOCVD discussed in Chapter 4. The main difference is the deposition temperature at which the films were grown.

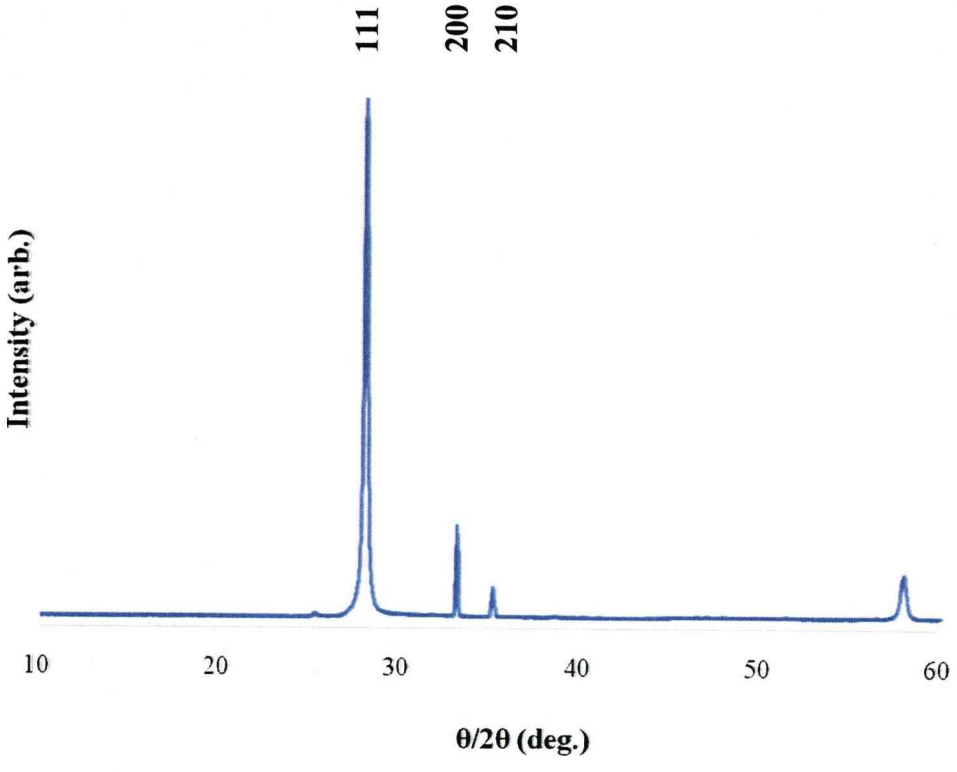

Figure 6.6: XRD pattern of a α-Bi_2O_3 deposited at 350°C

6.3.5 Growth Rates and XRD Analysis of SBT

A series of bismuth oxide / strontium tantalate SLs were grown with varying number of cycles/period of Bi_2O_3. The effect of $Bi(mmp)_3$ cycles per periods on film weight gain, is shown in Figure 6.7. This plot indicates that as $Bi(mmp)_3$ cycles/period increases, a significant contribution to the mass is observed.

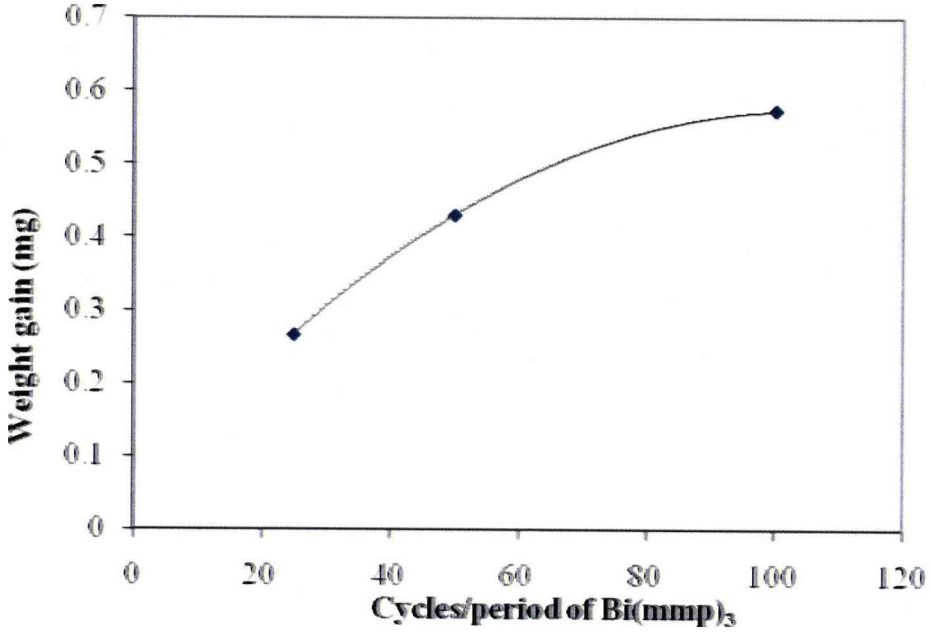

Figure 6.7: Thin film weight gain as a function of $Bi(mmp)_3$ cycles/period

Assuming that the oxide densities are 4.56 g/cc and 8.9 g/cc for strontium tantalate and bismuth oxide respectively, the mass balance analysis of the SLs, can be used to estimate that each strontium tantalate and bismuth oxide layer is ~2.5 nm thick. Coupling this information together with EDS data gathered from TEM data, showed that the SL deposited using 25 cycles/period of each precursor over 6 periods, was closest to required 1:2:2 Sr:Ta:Bi stoichiometry (see Figure 6.8). The sample was subjected to further annealing studies at 600, 700 and 800°C for 15 minutes in air and then were analysed.

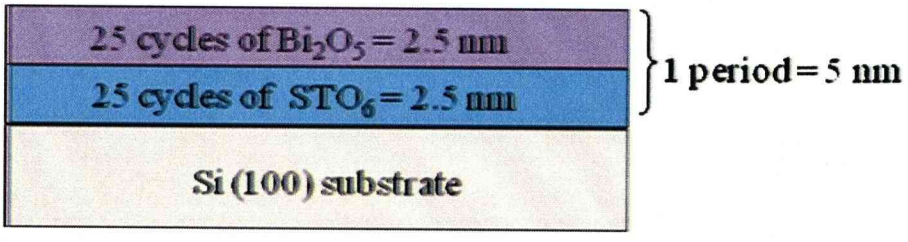

Figure 6.8: A systematic diagram illustrating the mass balance data of the preferred sample with the nearest required SBT stoichiometry

Figure 6.9 illustrates the XRD patterns of the as-deposited and annealed SBT SL obtained using the Kα copper line (λ=0.1542 nm). SBT has three different crystalline phases, the low-temperature fluorite phase, a bismuth deficient pyrochlore phase and the desired ferroelectric layered perovskite (Aurivillius phase). The fluorite phase was observed in the as-grown film, superimposed on a broader, less intense feature centred around ~28.8° believed to be the (111) reflection of α-Bi_2O_3 (present at the interfaces between bismuth oxide and strontium tantalate layers in the SLs) [9]. Consequently, the presence of the fluorite phase evident in Figure 6.3.5.c is indicative of either that the film grown at a lower temperature than required to form the SBT phase or by an excess of Bi.

Depending on the annealing conditions, the fluorite phase either changed to: a) a Bi-layered perovskite or b) a Bi deficit – pyrochlore phase. As

highlighted by the respective diffraction patterns, the SLs annealed at temperatures of 500°C or above, show that the α-Bi_2O_3 (111) diffraction feature is suppressed. The intensity of the underlying broad feature increases with annealing temperature up to 700°C. This may suggest that Bi diffuses into the strontium tantalate layers, allowing the formation of more fluorite SBT. The crystallisation of the SLs into SBT finally occurs after subsequent to annealing at 800°C. This is evident in the slight shift of the main peak to 29.2°. A number of weak diffraction features also became visible. These featured peaks are consistent with the Aurivillius phase of SBT [10], where the main feature at 29.2° is the (115) reflection. These XRD patterns are very similar to the XRD data presented in Chapter 4.

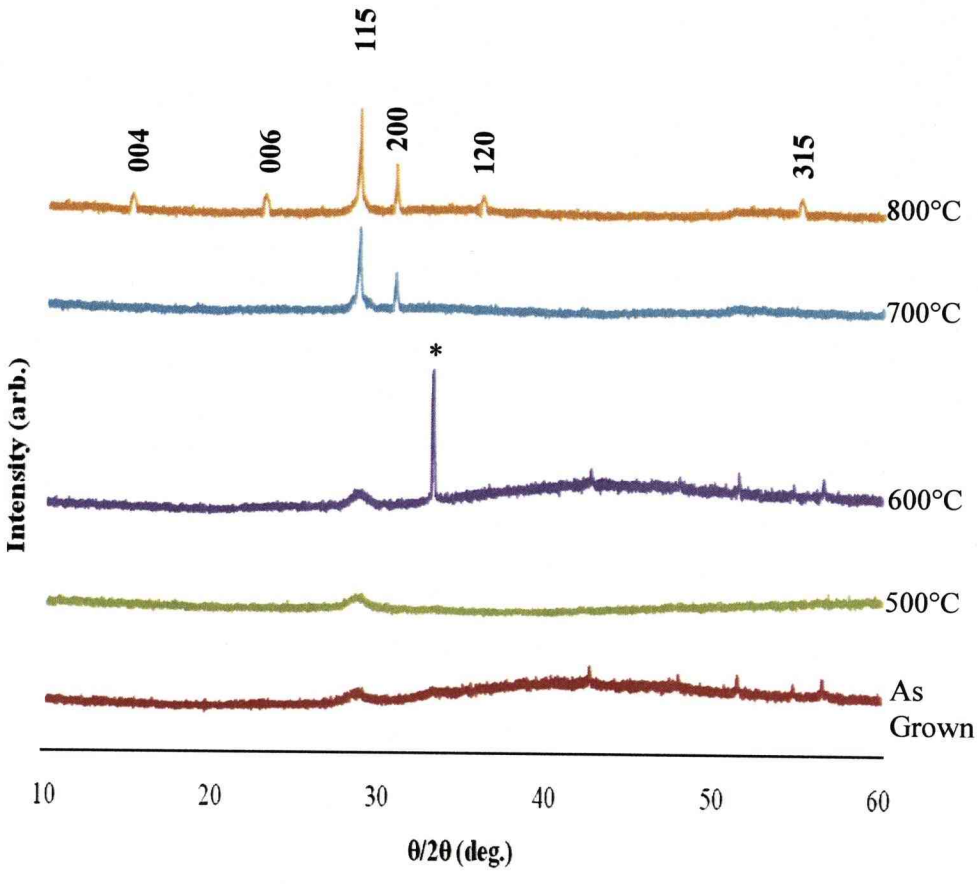

Figure 6.9: X-ray diffraction patterns of the as-deposited and annealed (15mins in air) SBT SL. Peak marked with * is due to the Si(200) of the substrate.

6.3.6 MEIS Studies of SBT

The effect of annealing on a 6-period strontium tantalate – bismuth oxide superlattice was investigated using medium energy ion scattering. The 200 keV He^+ ion beam was focused incident on the surface normal

(Si(100)) and the emerging back-scattered ions were collected from the Si[111] direction. The 2D energy – scattering angle MEIS map of the as-deposited SL is shown in Figure 6.10.

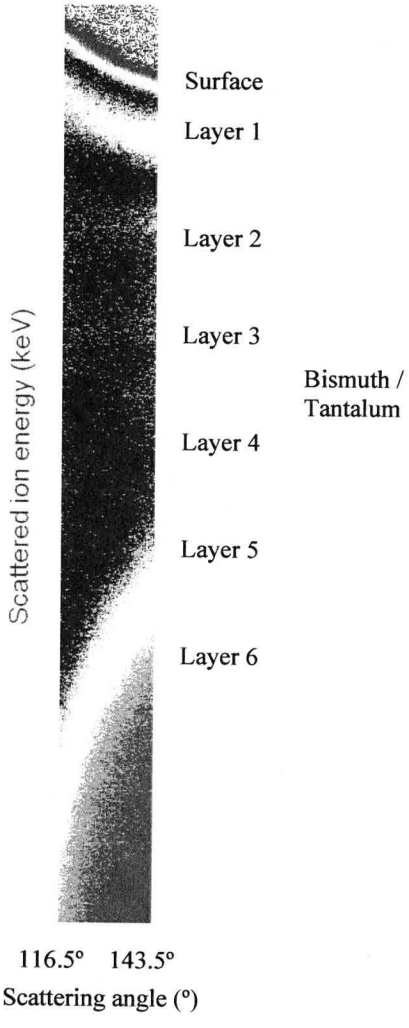

Figure 6.10: MEIS 2D energy/angle data tile of an as-deposited a 6-period strontium tantalate – bismuth oxide superlattice

Below the surface signal at the top of Figure 6.10, the convoluted thickness distribution or 'depth profile' of the bismuth and tantalum is seen. 1D energy depth profiles were collected from the as-grown superlattice and after annealing at 500, 600 and 700°C in air for 15 minutes. This data is shown in Figure 6.11.

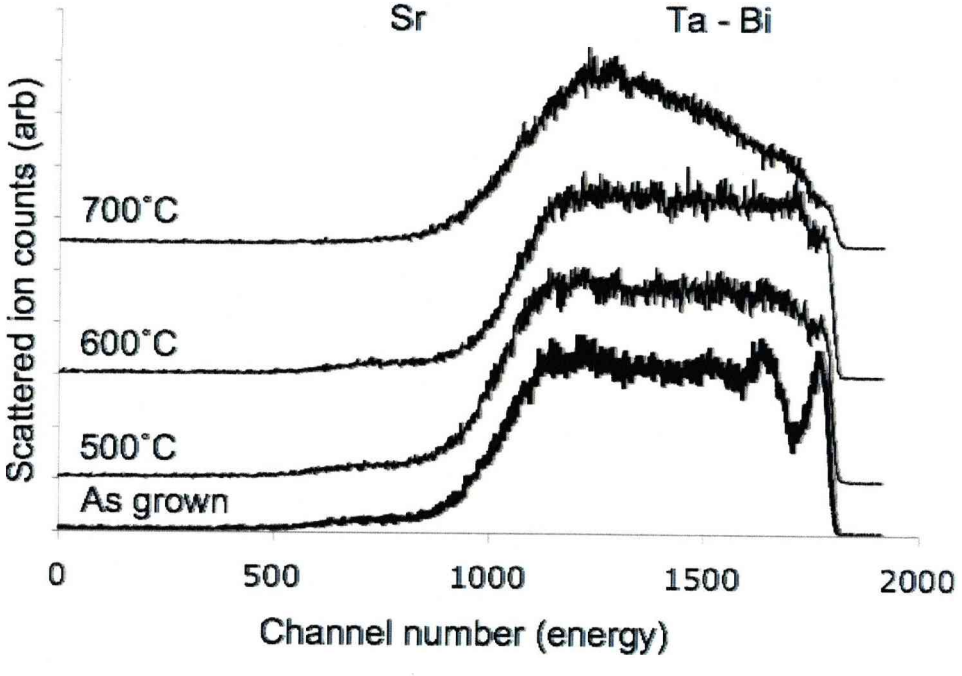

Figure 6.11: 1D MEIS energy depth profile of an as-deposited strontium tantalate – bismuth oxide SL and after annealing at 500, 600 and 700°C

Figure 6.11 shows an underlying periodic SL structure in the bismuth – tantalum distribution. The presence of a 'tail' intensity due to the strontium distribution is obscured for two reasons. Firstly the

incorporation of the heavier Bi is present, which has a high cross section in MEIS scattering; secondly the total thickness of the SBT layer is now relatively thick. As the cross section for scattering from strontium is relatively (to the Bi) small, the intensity appears to be low. However, modelling with SIMNRA shows that the strontium distribution is consistent with a stoichiometric SBT layer. After annealing at 500°C some inter-diffusion is evident within the SL. Annealing at higher temperatures shows some loss of intensity at the surface. This is particularly apparent at 700°C and is attributed to the loss of the heavier bismuth atoms from within the film. This observation is consistent with the earlier discussion in the chapter and the corresponding XRD data which shows a transition from a fluorite phase to a cubic layered perovskite one.

The MEIS data indicate that an inter-diffused SBT film can be formed from a strontium tantalate – bismuth oxide SL. The transformation starts at 600°C after annealing for 15 minutes.

6.3.7 STEM Studies of SBT

Figure 6.12(a) illustrates a cross sectional STEM image of the as-deposited SL sample viewed along the Si[110] zone axis. Six alternating periods consisting of strontium tantalate and bismuth oxide layers are clearly discernible as periodic light and dark regions of atomic number contrast respectively.

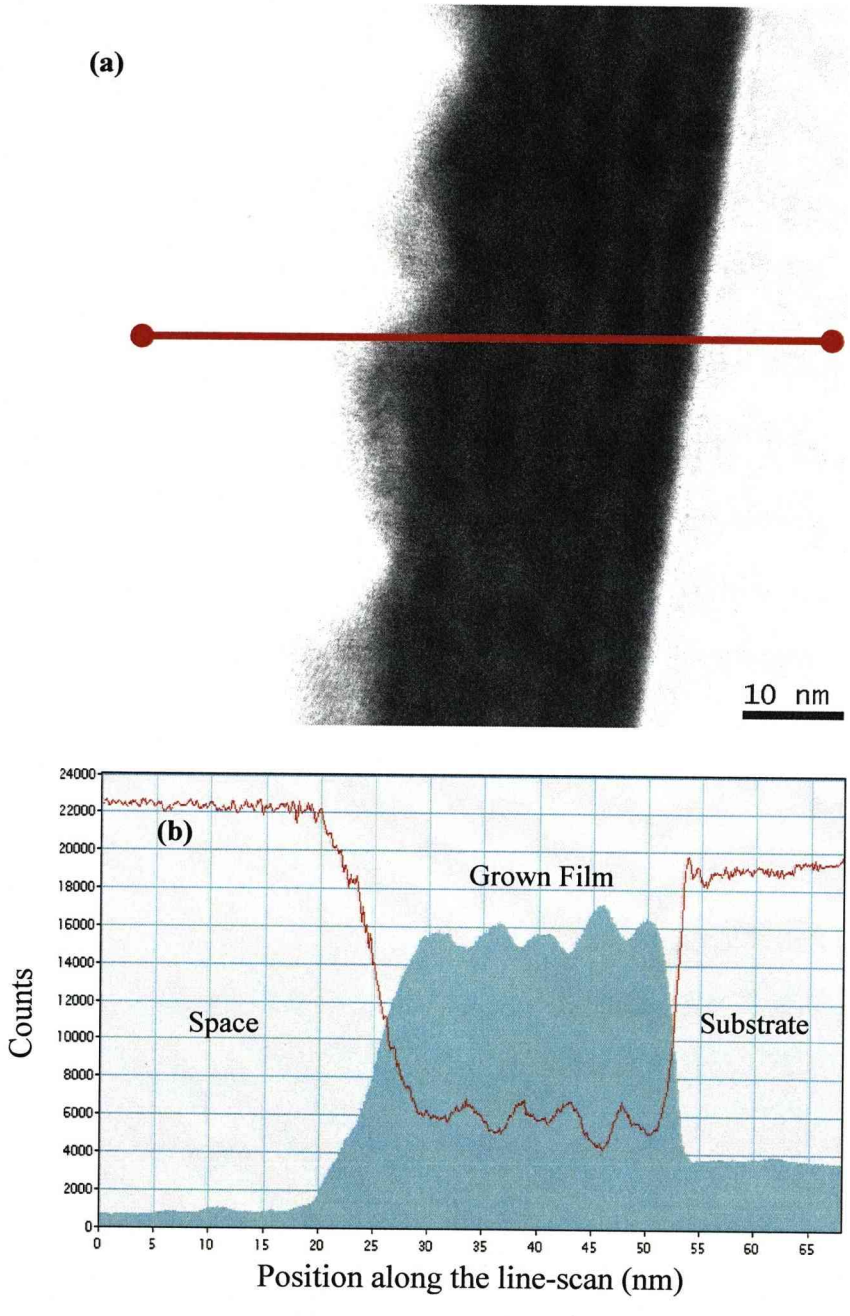

Figure 6.12: (**a**) STEM image of the SL as grown in [110] zone axis of the Si substrate. (**b**) STEM intensity profile representation of the line-scan

The SL is found to contain five layers of strontium tantalate and bismuth oxide which are relatively flat and planar (see Figure 6.12(b)) with respect to the silicon surface. The last outer period at the film surface, seems to be rougher and discontinuous. Moreover, the outcome of the analysis highlighted that the average thickness of a single period (strontium tantalate and bismuth oxide) was 5.17 nm and total thickness of entire film is 32.75 nm. This observation is in close agreement with the mass balance analysis made in Section 6.3.5 of this chapter. The mass balance gave a similar close estimation of both the total film thickness and the individual layer thicknesses.

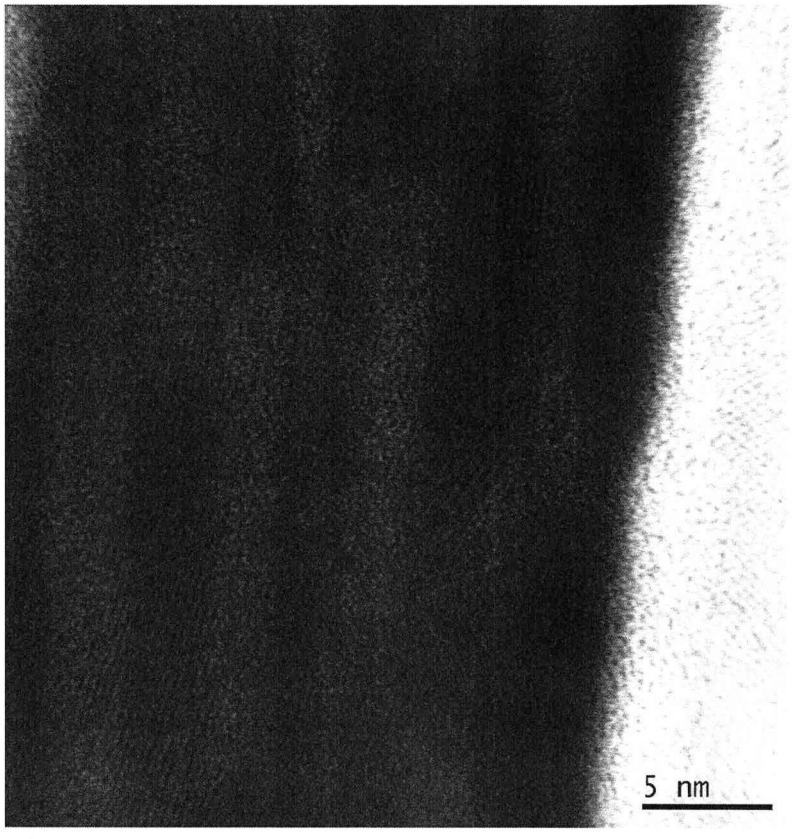

Figure 6.13: STEM image of the SL as grown featuring bismuth oxide crystallised grains in dark regions

It is evident from the micrograph, that the strontium tantalate has an amorphous disordered structure. By contrast, the bismuth oxide layers contain crystallite grains, as witnessed by the lattice fringes (shown in Figure 6.13). This observation is consistent with the (111) reflection of α-Bi_2O_3 diffraction pattern presented in Section 6.3.5. As mentioned earlier, the last deposited period has a rough morphology. The underlying reason

for this roughness may be either that the bismuth oxide properties encourage deleterious reactions with the environment (hydroxylation or carbonate formation); or that the grain growth caused by crystallised thin SBT films in the process development.

6.4 Conclusions

A series of bismuth oxide / strontium tantalate SLs have been grown under ALD growth conditions using $Sr\{Ta(OEt)_5(dmae)\}_2$ and $Bi(mmp)_3$ precursors for the first time. A SL deposited using 25 cycles/period of each precursor over 6 periods, was found to consist of the composition closest to required 1:2:2 Sr:Ta:Bi stoichiometry. The SL sample was subjected to annealing studies. Depending on the annealing conditions, the fluorite phase found in the film after growth was either transformed to: a) a Bi-layered perovskite or b) a Bi deficit – pyrochlore phase. The SL crystallises into SBT after annealing at 800°C. XRD featured peaks are consistent with the Aurivillius phase of SBT where the main feature at 29.2° is the (115) reflection.

The MEIS data indicate that an inter-diffused SBT film can be formed from a strontium tantalate – bismuth oxide SL. The transformation starts at 600°C after annealing for 15 minutes. This observation is consistent with the XRD data.

6.5 References

[1] A.C. Jones, *Mater. Chem.*, **12**, 2576 (2002).

[2] M. Leskelä, M. Ritala, *J. Phys. IV* Fr. **9-Pr8**, 837 (1999).

[3] M. Leskelä and M. Ritala, in *Handbook of Thin Film Materials*, vol. 1, pp. **108-113**, ed. H.S. Nalwa, Academic Press, (2002).

[4] D.M. Hausmann, E. Kim, J.S. Becker, R.G. Gordon, *Chem. Mater.*, **14**, 4350 (2002).

[5] K.-E. Elers, V. Saanila, P.J. Soininen, W-M. Li, J. T. Kostamo, S. Haukka, J. Juhanoja and W.F.A. Besling, *Chem. Vap. Deposition,* **8**, 149 (2002).

[6] J.W. Elam, D. Routkevich, P. Mardilovich and S.M. George, *Chem. Mater.*, **15**, (18), 3507 (2003).

[7] T. Watanabe, H. Funakubo, *Jpn. J. Appl. Phys.*, **39**, 5211 (2000).

[8] M. Schuisky, K. Kukli, M. Ritala, A. Harstå and M. Leskelä, *Chem. Vap. Deposition*, **6**, 139 (2000).

[9] S.A. Ivanov, R. Tellgren, H. Rundlof, V.G. Orlov, *Powder Diffr.* **16**, 227 (2001).

[10] C. Muller, F. Jacob, Y. Gagou, E. Elkaim, *J. Appl. Cryst.*, **36**, 880 (2003).

Chapter 7 Conclusions and Recommendations for Future Work

7.1 MOCVD of Strontium Tantalate and Bismuth Oxide

For the manufacturing of applications requiring thin-film ferroelectrics, the demand for higher memory device densities has increased. Strontium bismuth tantalate (SBT) is considered a promising material for use in non-volatile ferroelectric memory applications. Metal organic chemical vapour deposition (MOCVD) is regarded as the most suitable and essential deposition technique of SBT. Liquid injection MOCVD uses metal-organic CVD precursors, either evaporating or dissolving them into a solvent, to facilitate vapour transport. However, lack of suitable metal-organic precursors for MOCVD has resulted in implementing "single source" precursors to achieve the appropriate metal : metal ratio and meet the stoichiometric requirements. Meeting these is problematic as fragmentation of the precursor reactive Sr and Ta intermediates can occur.

In Chapter 4, liquid injection MOCVD of the precursors for the SBT components, strontium tantalate and bismuth oxide were investigated using the single source precursor $Sr\{Ta(OEt)_5(dmae)\}_2$ and $Bi(mmp)_3$. The effect of post-deposition annealing on the strontium tantalate and bismuth oxide thin films was also studied. The Aixtron TriJet™ liquid delivery system was used for the deposition studies. The strontium tantalate and bismuth oxide films were deposited over a range of substrate temperatures between 300 – 600°C. Characterisation of the strontium tantalate and bismuth oxide thin films was made using Auger electron spectroscopy and X-ray diffraction.

It was demonstrated that the composition of the strontium tantalate films was dependent on growth temperature. The film composition was evidently tantalum-rich (Sr:Ta ~0.8) at the lowest growth temperature of 300°C. Between 350 – 400°C, the Sr:Ta ratio in the films reaches a maximum close to unity. This is followed at higher temperatures by a decrease in the strontium content. The optimum growth temperature was found around 510°C, which is where the Sr:Ta ratio in the film was 0.5 - stoichiometry close to the $SrTa_2O_6$ found in the SBT composition.

The XRD studies illustrate that across the temperature range of 300 – 600°C, the as-deposited ST films exhibit an amorphous-like microstructure and demonstrate no crystalline diffraction features. It is evident that films undergo crystallisation at around 650°C (for 15 minutes) in air and form an orthorhombic crystalline phase.

The $Bi(mmp)_3$ precursor deposits bismuth oxide films over the temperature range of 300 – 600°C. At increased temperatures, the XRD pattern of bismuth oxide revealed that the films had a crystalline habit and consisted of the α-Bi_2O_3 phase.

7.2 MOCVD of Strontium Bismuth Tantalate using the Superlattice Approach

Initial attempts of depositing SBT were made by simultaneous injection of $Sr\{Ta(OEt)_5(dmae)\}_2$ and $Bi(mmp)_3$ precursor solutions. It was found that with increased $Bi(mmp)_3$ partial pressure, the level of Bi incorporation also noticeably increased in a non-linear manner. Moreover, the Sr incorporation was rapidly suppressed as the Bi content exceeded a few atomic percent. Introducing Bi into the film without loss of Sr (to form the Aurivillius phase) was a logical outcome from Chapter 4.

Investigations into the low temperature synthesis of $SrBi_2Ta_2O_9$ thin films were completed using a series of Bi_2O_3 / $SrTa_2O_6$ superlattices (SLs) via the liquid injection MOCVD technique. The effects of post-deposition annealing were examined using MEIS, HR-TEM and XRD as methods of exploring the effect of annealing temperature on the composition, structure and crystallinity of the SLs.

The XRD patterns of the annealed films revealed that the optimised SL structures converted the distinct layers of Bi_2O_3 and $SrTa_2O_6$, containing

some interfacial pyrochlore, into a single polycrystalline layer of the perovskite-like SBT phase.

The effects of post-deposition annealing were studied using medium energy ion scattering (MEIS) to measure the compositional depth profile the SLs and measure the interlayer inter-diffusion as a function of temperature. MEIS depth distribution illustrated that with increasing annealing temperature, interdiffusion between the bismuth oxide and strontium tantalate layers progressively increased. This finding was in agreement with the XRD outcome.

7.3 Atomic Layer Deposition of Strontium Bismuth Tantalate

The purpose of Chapter 6 was to describe novel methods of reducing the thermal budget (temperature - time) required to produce the Aurivillius phase of SBT. This involved the use of the ALD technique to deposit SLs, which could be converted to SBT. ALD is a low-temperature modification of MOCVD, whereby precursors are sequentially dosed into a vacuum chamber under computer control. Significant advantages of ALD include excellent thickness control and perfect step-coverage of high aspect ratio structures.

A series of bismuth oxide / strontium tantalate SLs were grown under ALD growth conditions using $Sr\{Ta(OEt)_5(dmae)\}_2$ and $Bi(mmp)_3$ precursors for the first time. A SL deposited using 25 cycles/period of each precursor over 6 periods, was found to consist of the composition closest to required 1:2:2 Sr:Ta:Bi stoichiometry. The SL sample was subjected to annealing studies.

Depending on the annealing conditions, the fluorite phase of the SBT film either transformed to: a) a Bi-layered perovskite or b) a Bi deficit – pyrochlore phase. Complete crystallisation of SBT occurred following

annealing at 800°C. XRD diffraction patterns featured peaks, which were consistent with the Aurivillius phase of SBT where the main feature at 29.2° is due to the (115) reflection.

The MEIS data from these films indicates that an inter-diffused SBT film can be formed from a strontium tantalate – bismuth oxide SL. The transformation starts at 600°C after annealing for 15 minutes. This observation is consistent with the XRD data.

7.4 Recommendations for Future Work

In the course of this research, low temperature synthesis of SBT, deposited by MOCVD and ALD techniques has been investigated. Various characterisation methods such as AES, XRD, MEIS and TEM have been exploited to elucidate the composition and structure of these materials. From the literature review, it was evident that all these characterisation methods have advantages and disadvantages. In particular, the most commonly used method to study SBT thin films was the X-ray diffraction (XRD) technique.

The principle structure of SBT is an orthorhombic-layered perovskite. However, the SBT thin films encountered in practice are often non-ideal and contain fluorite or pyrochlore phases. Using the XRD technique, only the average structure of SBT is observed, as the spatial resolution is limited to ~30 μm, and, most crucially, the concomitant fluorite or pyrochlore phases are not easily discernable by their diffraction patterns from the layered perovskite.

To improve the analysis of the SBT films, Raman spectroscopy is recommended instead of XRD. Raman spectroscopy frequently allows

more rapid data collection and provides a sensitive means of identifying the crystallographic phase grown.

Raman scattering by an anisotropic crystal can be used to: characterise material phases; measure temperature; and provide information about the crystallographic orientation of a sample. The polarisation of the Raman scattered light with respect to the crystal and the polarisation of the laser light can be used to find the orientation of the crystal. Raman spectroscopy offers several advantages for microscopic analysis. The specimens do not need to be sectioned, for example. Raman can also detect low-concentration impurity phases. In comparison with the diffraction methods it is generally more sensitive to the non-crystalline (but Raman active) phases.

In addition to better material characterisation methodologies, the ferroelectric properties of the deposited SBT thin films can also be characterised (detailed in Chapter 2). The Sawyer-Tower measuring technique, which displays a dielectric hysteresis loop, is an established method for the characterisation of non-linear devices. Electrical polarisation is the main parameter measured for the characterisation of ferroelectric materials. This parameter is deduced from hysteresis loops

that are obtained by tracing the change of polarisation versus applied electric field. Unfortunately, facilities for measuring the ferroelectric properties of the SBT films synthesised were not accessible during the course of this research. It is recommended that the electrical properties of the SBT films should be measured to complete the evaluation of the processing – property relationships.